Investigation of metal hydroxides-graphene composites as electrode materials for supercapacitor applications

by

Momodu Damilola Yusuf

A thesis submitted in partial fulfillment of the requirements for the degree of

DOCTOR OF PHILOSOPHY (PHD) IN PHYSICS

Faculty of Natural and Agricultural Sciences

University of Pretoria

Hatfield Pretoria

June 2015

Supervisor/Promoter: **Prof. N. I. Manyala**

Co-supervisor: **Dr. J. K. Dangbegnon**

Declaration

I, Momodu, Damilola Yusuf declare that this thesis, entitled "***Investigation of metal hydroxides-graphene composites as electrode materials for supercapacitor applications***" which I hereby submit for the degree Doctor of Philosophy (PhD), is the result of investigations carried out by me under the supervision of Prof. N. I. Manyala and co-supervision of Dr. J. K. Dangbegnon, in the Physics department at the University of Pretoria, South Africa and has not previously been submitted by me for a degree at any other tertiary institution. In keeping with the general practice in reporting scientific observations, due acknowledgement and referencing has been made whenever the work described is based on the findings of other investigators.

Signature…… Date……

The vocation, is to make my research

impact on me and generations yet unborn,

for it is the only true way to have

lived a fulfilling life...

Damilola Y. Momodu

(2015)

Dedication

With unending love,

To my Dad and Mom,

Mr. A.B Momodu and Late Mrs. C.A Momodu

for their inspiration thus far…

Acknowledgements

All praises is due to the Almighty God, the Lord of the Worlds, it is He alone that I worship and it is from Him that I seek help. He is the Creator of all, the Guider of hearts and Master of the day of Judgment. I would not be here today without His blessings, favors, sustenance and grace. Thank you Lord.

My sincere gratitude goes to my supervisor, Prof. Ncholu Manyala, who was a great advisor, mentor, friend and uncle throughout my PhD research. In the last couple of years, he has not only guided and assisted through getting a good experimental thesis work done, but he constructively criticized my work which enabled me work harder. Also to my co-supervisor, Dr. Julien K. Dangbegnon, for the invaluable assistance in carrying out my laboratory work and also in meticulously analyzing results and working closely with me like an elder brother throughout my PhD sojourn. Only God can repay you both for all the effort and time you put into me.

I would like to give unending gratitude to my Dad, Mr. A.B Momodu for his constant prayers and encouragement which kept me standing strong in the midst of the struggle. The inspiration I got from you to pursue the very best in life and the good upbringing you have instilled in me, has taken me to places I never imagined. Also to the rest of my lovely family for their unending calls and chats that made me never miss home, my brothers and sisters, especially my big Sister Adama who constantly ensured I was always comfortable and doing well. May God keep you all in good health for me.

My special gratitude goes to my longtime friend and brother, Dr. Abdulhakeem Bello for giving me unending assistance both in the laboratory and making my postgraduate research a success. My special thanks to him for the role he played in working extra hours on weekends in ensuring we were able to get good results and finish up my work in record time.

I would also like to thank the rest of my group members, Farshad B., Fatemeh T., Tshifhiwa M., Dr. Fabiane, Moshawe M., Dr. Khamlich, Abubakar K., Faith U. and Okikiola O. for their ever-reliable support and assistance they rendered. The constructive discussions sleepless nights and sacrifices at the lab in helping out with experiments even in your various busy schedules. You guys will remain forever evergreen in my memory. I hope we meet again soon and probably work on bigger scientific projects in the near future.

I would also like to appreciate head of the department Prof. C.C. Theron for some part-time work in the department to enable me supplement my finances and both the University of Pretoria and the South African national research foundation (NRF) financial support.

I am also thankful to the great friends I made here at the Physics Department, fellow students, staff, professors who put up with me throughout my stay, especially some great friends worth mentioning; my best friend and confidant, Ms. Thabsile T.T for the inspiring discussions and golden memories shared, Ms. Belinda M., Ms. Mosele T., Mr. Isaac N., Mr. Katlego M., Dr. Paul E., Dr. Thulani H., Mr. Ezekiel O., Mr. Mmusi G., Ms. Opeyemi O., Ms. Asmita S., Mr. Alex P, Ms. Seppie T. and Mr. Kian G., but to mention a few. My life in the last 36 months has been so interesting and memorable with you guys. I have learnt a lot and I know we will keep in touch to share more good times.

I also will like to specially thank Antoinette and Andre at the Microscopy department for their assistance in getting nice SEM images, Dr. Linda Prinsloo for all the assistance with measuring equipment. Likewise to Ms. Suzette Seymore and Mrs. Isbe Van DerWesthuizen at the Institute of Applied Materials, South Campus laboratory for their unending support in procurement and laboratory work.

My acknowledgment would not be complete without mentioning my fiancée, Pharteemah Lawal. Your patience, prayers and perseverance has always been appreciated. I will continue to pray that all goes well and our dreams for the future come true soon.

Table of Contents

List of figures

List of Equations

$$E_{S1} + A^- \xrightarrow{CHARGING} E^+{}_{S1} // A^- + e^- \quad (1)$$

$$E^+{}_{S1} + A^- + e^- \xrightarrow[DISCHARGING]{} E_{S1} + A^- \quad (2)$$

$$E_{S2} + C^+ + e^- \xrightarrow{CHARGING} E^-{}_{S2} // C^+ \quad (3)$$

$$E^-{}_{S2} + C^+ \xrightarrow[DISCHARGING]{} E_{S2} + C^+ + e^- \quad (4)$$

$$E_{S1} + E_{S2} + A^-C^+ \Leftrightarrow E^+{}_{S1} // A^- + E^-{}_{S2} // C^+ \quad (5)$$

$$C_i = \frac{\varepsilon A_i}{d_i} \quad (6)$$

$$C = \frac{A\,\varepsilon}{4\,\Pi\,d} \quad (7)$$

$$\frac{1}{C_{DL}} = \frac{1}{C_Q} + \frac{1}{C_D} \quad (8)$$

$$C = \frac{d(\Delta Q)}{d(\Delta V)}. \quad (9)$$

$$HRuO_2 \longleftrightarrow H_{1-\delta}RuO_2 + \delta H^+ + \delta e^- \quad (10)$$

$$HRuO_2 + \delta H^+ + \delta e^- \longleftrightarrow H_{1-\delta}RuO_2 \quad (11)$$

$$HRuO_2 + HRuO_2 \longleftrightarrow H_{1-\delta}RuO_2 + H_{1-\delta}RuO_2 \quad (12)$$

$$C_i = \left|\frac{Q}{E_2 - E_1}\right| \quad (13)$$

$$\boldsymbol{I = a\, v^b} \quad (14)$$

$$C = \frac{I}{v}: \quad (15)$$

$$C_s\ \left(\frac{\mathrm{F}}{\mathrm{g}}\right) = \frac{\bar{A}}{\upsilon m \Delta V} \quad (16)$$

$$I = C\ \times \frac{dV}{dt} \quad (17)$$

$$E_D = \frac{1}{8} C_{sp}\, V^2 \quad (18)$$

$$E_{MAX} = \frac{1}{2\times 3600}\, C\, V^2 \quad (19)$$

$$P_{MAX} = \frac{1}{4\times(ESR)}\ \frac{V^2}{M} \quad (20)$$

$$C\ =\ I/(dV/dt). \quad (21)$$

$$C = \frac{1}{2\pi f |Z"|} \quad (22)$$

$$n\lambda = 2d \sin\theta \quad (23)$$

List of Tables

List of Abbreviations and Symbols

AC	Activated carbon
AE	Aqueous electrolytes
Ag/AgCl	Silver – Silver Chloride
BET	Brunauer-Emmett-Taylor
C	Charge or Discharge Rate
CVD	Chemical Vapor Deposition
CPs	Conducting polymers
CV	Cyclic Voltammetry
*C*s	Specific Capacity
°C	Degree Celsius
DL	Double layer
EC	Electrochemical Capacitor
EDLC	Electric double layer capacitor
ESR	Equivalent Series Resistance
EIS	Electrochemical Impedance Spectroscopy
FESEM	Field Emission Scanning Electron Microscopy
FTIR	Fourier Transform Infrared Spectroscopy
HEV	Hybrid Electric Vehicle

ILs	Ionic liquids
LDH	Layered double hydroxide
NMP	N-Methyl-2-Pyrolidone
PVDF	Polyvinylidene Fluoride
Redox	Reduction-Oxidation
PC	Pseudocapacitor
REC	Redox Electrochemical Capacitor
R_s	Solution (electrolyte) resistance
SCs	Supercapacitors
SEM	Scanning Electron Microscopy
T	Temperature
TGA	Thermal Gravimetric Analysis
tMOs	transition-metal oxide
tM-OH	transition metal hydroxides
V	Volt
XPS	X-ray Photoelectron Spectroscopy
XRD	X-ray Diffraction
UC	Ultracapacitor
Z’	Real impedance
Z’’	Imaginary impedance

Abstract

The aim and objectives of this work are to optimize the synthesis of metal hydroxides - graphene foam (GF) composites using different configurations of graphene with a facile and environmentally friendly solvothermal technique for energy storage applications. The evaluation of the morphological, structural, surface area and compositional properties of the composites were carried out with the techniques such as field emission-electron microscopy (FESEM), transmission electron microscopy (TEM), X-ray diffraction (XRD), Brunauer–Emmett–Teller (BET), Raman spectroscopy, and Fourier transform infrared (FT-IR) spectroscopy. The results show the existence of interlaced sheets of metal-hydroxides-graphene composites with sufficient surface area necessary for efficient charge storage. The main reason for incorporating graphene foam (GF) into these metal hydroxides in this study was due to its unique mechanical properties, good conductivity and large surface area which offer the possibility for an enhanced deposition/adsorption of the active metal hydroxides both in-situ and as a supporting template for practical applications. The electrochemical properties of the synthesized composite electrodes modified with different graphene foam nanostructures were thus explicated in a 3-electrode system (with Ag/AgCl as reference electrode)and they all showed excellent electrochemical performance. The overall results clearly demonstrated an excellent potential of graphene based composite electrode materials for energy storage applications.

CHAPTER 1

1.0 INTRODUCTION

1.1 Background and General Motivation

The increasing demand for a reliable and sustainable source of energy for technological growth and development has facilitated a simultaneous increase in funding energy-related research. The increasing world population and advancement in technology has also created an increase in the global demand for energy use ranging from small scale domestic applications (in terms of personal use) to large scale industrial applications for transportation and manufacturing purposes. However, in a bid to create sufficient energy to meet the sky-rocketing demand, the diverse routes taken in the production of energy also constitutes a great threat to life and the universe at large. Some of these routes include, the energy generated from thermal power stations via combustion of coal, hydroelectric power stations using dams and most recently, nuclear reactors among others. These pose issues of global warming and environmental pollution, on one hand, and the toxic waste from energy generation on the other, are of important concern to many countries today.

The depletion of natural resources like crude oil, coal and natural gas reserves which are the most common sources of fuel for energy generation today has resulted in the need to develop a sustainable and reliable form of energy for the future. Renewable energy sources are energy resources which can be easily and quickly restored by a natural

process. This has led to an increasing interest in renewable energy-based research for generating a much cleaner and safer energy generation/conversion systems. Furthermore, if the main goal is to ensure a readily available energy source to meet the demand, there is also a need to build reliable and efficient energy storage systems to preserve the excess generated power (from these renewable energy sources) for use when required for specific applications. Such storage systems must possess high energy and high power densities in order to provide a robust storage capacity along with an instantaneous/rapid delivery capability respectively. This will provide a reliable system which is able to fit into present day ubiquitous technology where energy is needed at different instances to power complex assemblies such as portable electronic gadgets, hybrid electric vehicles, speed trains etc.

Some of the common energy storage devices in use today are batteries and conventional capacitors which are characterized with low power density and energy density respectively. Thus, an efficient high performance, low cost and environmentally safe all-in-one energy storage system which combines the properties of the batteries and capacitors is required.

Electrochemical Capacitors (ECs) are emerging technologies with a bright as well as promising future to complement and possibly replace batteries and conventional capacitors for energy storage [1,2]. However, the performance of these technologies is related to their constitutive material characteristics. In order to optimize them for suitable specific energy storage applications, there is a need to analyze their individual

properties to meet the increasing consumption rate. It is worth stating that the lifetime of storage systems should be comparable to the requirements presented by these emerging technologies. Furthermore, the long term goal is to develop a system which is easily compatible with individual energy conversion systems like fuel cells, solar cells, windmills, etc. in order to easily collect excess generated energy and store it for later use.

Electrochemical capacitors (ECs), Supercapacitors (SCs) or Ultracapacitors (UCs) are commonly used to classify a category of energy storage devices that are closely linked with rapid storage and release of energy [3]. In comparison with conventional capacitors, the specific energies of SCs are much higher while their corresponding power densities are much greater than most batteries [3,4]. Thus, with the appropriate structural model, there is a promising trend to obtain hybrid structures with a combination of both conventional capacitors and batteries which exists as a stand-alone storage unit. Their highly reversible charge-storage capability also makes them the ideal candidate for much desirable long term applications which fits perfectly into the fast growing technological advancements in the energy industry [3–6].

SCs are broadly divided into two main types based on their mode of energy storage and associated material components, namely;

(i) the electrical double-layer capacitors (EDLCs)

(ii) the pseudocapacitors or redox electrochemical capacitors (RECs)

The EDLCs store energy by charge separation which is similar to the charge storage mechanism in a basic capacitor. However, the magnitude of charge stored in the EDLCs is very much higher due to the surface area of the active electrode material and the distance over which charge separation occurs [1]. The ions within the electrolyte which are responsible for charge movement between the electrode and electrolyte interface involves very fast processes as compared to batteries [4]. This explains the reason for their dynamic charge propagation (short-term pulse) which is useful in emerging technological applications (like hybrid electric vehicles, emergency doors of aircraft etc.) where an initial high specific power is required.

Carbon is the only material used for fabricating EDLCs and this has been extensively studied by researchers [4,7]. This has led to the discovery of numerous forms of carbon depending on the synthesis route used. Some of the important forms of carbon suitable for electrochemical studies include activated carbon [8–10], graphene [11,12], carbon nanotubes [13,14], onion-like carbons [15], activated carbon fibers (ACF) [16], etc. These different forms of carbon mentioned are also associated with a broad range of selective properties which make them suitable for energy storage applications. Some of these properties include; high surface area, controllable pore size, high conductivity, good corrosion resistance, high temperature stability, relatively low cost due to its abundance in nature and its compatibility with other material matrix to form composites [2,4,11,17–19].

Graphene, which is among one of the most recently discovered allotropes of carbon with a one atomic thick-2D planar nanosheets, has received tremendous attention due

to its attractive properties such as high electrical conductivity, high surface area (theoretically quoted as ~2600 m^2/g), superior carrier mobility (> 200000 cm^2/V S) coupled with its robust mechanical properties [20–22]. Although graphene has unique desirable properties, the development of highly conductive large surface area material alone is not sufficient to improve electrochemical performance of energy storage devices. These attributed values quoted above are theoretical values which are practically unattainable at the moment due to the propensity of graphene sheets to restack and the polycrystalline nature of the graphene produced in the laboratory. EDLCs also suffer from a low energy density due to an inherent limitation of the electrostatic surface charging mechanism [23] and the nanoscale sheet-like morphology of these materials, generates a concern that the obtained gravimetric-normalized capacitance may not be a useful metric [24]. Even so, graphene and other carbonaceous species has been successfully incorporated with other materials to obtain hybrid composites [22,23,25,26].

Pseudocapacitors (also referred to as Redox Electrochemical Capacitors, RECs) store energy by means of reversible Faradaic-type charge transfer which is associated with an electrochemical charge transfer process which occur at the surface or near the surface within the electrode material. A notably higher capacitance is often observed for these types of capacitors as compared to EDLCs due to the non-electrostatic nature of their capacitance. They usually have a battery-like type capacitive behavior. However, the main difference between pseudocapacitive materials and batteries and is that the charging and discharging behavior of former occurs on the order of seconds and

minutes [27]. This rouses a strong motivation for studying and developing pseudocapacitive or faradaic-type materials in that if the findings obtained are useful, it will lead to the fabrication of a material with both high energy and high power densities. Common materials which used for redox capacitors (or pseudocapacitors) are the conducting polymers (CPs), transition-metal oxide (tMOs) and transition metal hydroxides (tM-OH) due to their ability to conduct fast and reversible faradaic reactions at the electrode/electrolyte interface [23].

Among the transition metal hydroxides, layered double hydroxides (LDH) containing double metals in a unique pattern have been widely adopted as electrode material for pseudocapacitors due to their excellent redox property, tunable composition, flexible ion exchangeability and environmentally friendly growth techniques [28–32]. However, CPs are characterized with a poor cyclic stability resulting from the volume expansion and shrinking of the active polymer material during charge and discharge periods over a long number of cycles [33]. On the other hand, the tMOs and tM-OHs are characterized with a relatively low electron transfer and mass diffusivity which hinders their rate capabilities and affects the overall capacitive performance. Also, their surface properties are still low when compared with carbonaceous materials used for the EDLCs. Hence, it is necessary to combine these materials with high surface and conducting carbon materials to obtain a synergy of properties for both the EDLCs and redox capacitors [34–36]. This will provide a hybrid system with combined and improved characteristics which would boost the electrochemical performance of the entire storage system.

Composite materials containing pseudocapacitive species with highly conductive and high surface area graphene have been studied by various researchers over time and these composites show a promising trend towards achieving the desired goal for a robust energy storage system to meet the global demand [12,37–41]. The combination of these materials provides a mutual or symbiotic relationship in which they independently improve the other pair's contact of electrochemically active sites resulting in the overall enhancement and performance of their electrochemical storage capability. Recent studies by Wimalasiri *et al*. [41] showed that graphene enhances the conductivity of Nickel–Aluminum LDH and eliminated the need for conducting additives; the Ni-Al LDH also prevents graphene sheets restacking. As a result, the layer structured hybrid material demonstrated a superior electrochemical performance due to the synergistic contribution from the pseudocapacitance of Ni-Al LDH and the electrical double layer capacitance of graphene.

Graphene synthesis has been extensively carried out by various techniques which include mechanical cleavage of highly oriented pyrolytic graphite [42], conversion of SiC (0001) to graphene *via* sublimation of silicon atoms at high temperatures [43], covalent [44] or non-covalent [45] exfoliation of graphite in liquids and the reduction of oxidized graphite by the modified Hummers method [46,47]. However each of these techniques listed have one or more problems associated with them ranging from the structural and electronic disorder in the graphene to the price of the initial SiC wafer in the case of sublimation of silicon atoms [48].

Chemical Vapor Deposition(CVD) has been recently discovered to be a very promising, easily obtainable, inexpensive and relatively safe approach for deposition of reasonably high quality graphene on transition metal substrates such as Ni [49], Cu [50], Pd [51] existing in the form of sheets or foams. Recently, synthesis of graphene on 3-dimensional nickel foam with the subsequent etching of the metal to obtain graphene foam have been carried out to obtain supercapacitor electrodes with superior electrochemical properties [52,53] when used in combination with other metal oxides as composite electrodes.

This research work is centered on fabrication of graphene-based metal hydroxide composites which are synthesized in the form of sheets. This hybrid system will aid in preventing the re-stacking of graphene sheets earlier discussed whilst also improving the electrical properties of the metal hydroxide matrix in which graphene is incorporated. We focus our attention on chemical vapor deposition (CVD) method as a promising approach for the production of graphene foam and graphene based templates (current collectors) which exhibits improved electrochemical properties when compared to reduced graphene oxide (r-GO) and pristine nickel foam respectively. This will go a long way in improving the electrochemical properties of the composite materials as possible electrode for supercapacitor applications.

1.2 Aim and Objectives

The aim and objectives of this research study are as follows:

I. Synthesis of high quality graphene-foam samples using chemical vapor deposition on clean nickel foam (NF) substrates.

II. Synthesis of metal hydroxide samples using a facile environmentally – friendly solvothermal technique in different reaction solvents and elucidate their formation mechanism in the respective solvents.

III. Fabrication of metal hydroxide - graphene composites using numerous synthesis techniques like solvothermal method, with graphene in different configurations such as graphene foam (GF), nickel foam-graphene (NF-G) templates.

IV. Evaluation of the morphological, structural and pore size distribution of the composites with techniques such as field emission-electron microscopy (FESEM), Raman spectroscopy, Fourier transform infrared (FT-IR) spectroscopy, transmission electron microscopy (TEM) and x-ray diffraction (XRD) and Barrett-Joyner-Halenda (BJH) technique.

V. Explication of the electrochemical performance/characteristics of the metal hydroxide-graphene composite electrodes by understanding the principle of its charge storage mechanism and the interaction between the substrate and active material.

1.3 Scope and Outline of thesis

In this work, the main focus is not on the large scale design or applicability in a whole energy storage system but rather investigating the ways to improve the electrochemical properties of possible graphene-based material composites for use as electrodes; i.e. optimizing the electrode material for intended laboratory scale applications and

subsequently a larger scale in the near future. This includes experiments and further studies conducted in order to clearly understand the processes which take place at the active material/electrolyte interface during charge separation, charge transport and redox processes.

This work has been performed at the University of Pretoria, Department of Physics, under the Institute of Advanced Materials. The studies involves an extensive characterization of metal hydroxide-graphene composites mainly utilizing the laboratory synthesized Ni-Al layered double hydroxides with graphene in different forms and further adding it to improve the electrochemical properties of a conducting polymer blend. Another section involves an in-situ growth of hexagonal zinc chloride hydroxide (Simonkolleite) platelets in the presence of graphene sheets to form a graphene-based composite. The overall electrochemical performance is extensively investigated using the conventional electrochemistry techniques ranging from Electrochemical Impedance Spectroscopy (EIS) to Cyclic Voltammetry (CV) and Galvanostatic tests. Efforts are made to elucidate the reason for the observed enhancements by analyzing the charge storage trend at varying current densities and cycling stability over several thousand operating cycles.

The general objective of this thesis is to contribute to the collective knowledge database in the field of supercapacitor research. The results discussed are quite important in further understanding the internal processes within the composite electrode material as alternatives for future applications. With this underway, it provides an avenue for improvements to be made where necessary. Thus, the key challenges to supercapacitor

development leading to its full commercialization remain dependent on the electrode stability and improvement of electrode specific capacitance along with the operating voltage so as to increase the overall energy density to be comparable to much common high performance batteries presently in use.

The thesis is divided into five chapters:

Chapter 1 presents a general introduction to the global energy issue and a proposed solution with respect to modeling efficient, clean, reliable and environmentally friendly energy storage systems.

Chapter 2 presents a literature review on ongoing research related to graphene-based supercapacitors and the way forward.

Chapter 3 presents the detailed experimental procedure used in this study while

Chapter 4 deals with the results obtained accompanied with detailed discussion of the results presented in sub-sections. A summary of the conclusions from each experimental result discussed will be presented in different sections of Chapter 4.

Chapter 5 contains general conclusions from the entire thesis and details of future work to be performed in this study are then presented in Chapter 6.

Most importantly, we have been able to show that the metal hydroxide - graphene composites could be an excellent material for ECs application when used both in-situ and as a current collector template. In particular, we have also demonstrated a tremendous improvement in the supercapacitance behavior (by an order of magnitude) for conducting polymer-blend composites with the introduction of metal hydroxide-graphene foam material into the active matrix. An excellent stability is recorded for

these materials even after cycling them over a reasonably long number of operating cycles at high current densities.

1.4 References

[1] B. Conway, Electrochemical Supercapacitors: Scientific Fundamentals and Technological Applications, Kluwer Academic Publishers, Plenum Press: New York, 1999.

[2] F.Benguin, E. Frackowiak, Carbon 39 (2001) 937.

[3] A.G. Pandolfo, A.F. Hollenkamp, J. Power Sources 157 (2006) 11.

[4] L.L. Zhang, X.S. Zhao, Chem. Soc. Rev. 38 (2009) 2520.

[5] A. Nishino, J. Power Sources 60 (1996) 137.

[6] A. Shukla, J. A. Harrison, Resonance 6 (1981) 333.

[7] F. Béguin, V. Presser, A. Balducci, E. Frackowiak, Adv. Mater. 26 (2014) 2219.

[8] E. Raymundo-Piñero, K. Kierzek, J. Machnikowski, F. Béguin, Carbon 44 (2006) 2498.

[9] K. Kierzek, E. Frackowiak, G. Lota, G. Gryglewicz, J. Machnikowski, Electrochim. Acta 49 (2004) 515.

[10] A. Bello, F. Barzegar, D. Momodu, J. Dangbegnon, F. Taghizadeh, N. Manyala, Electrochim. Acta 151 (2015) 386.

[11] M. Stoller, S. Park, Y. Zhu, J. An, R. Ruoff, Nano Lett. 8 (2008) 3498.

[12] Z.S. Wu, W. Ren, D.W. Wang, F. Li, B. Liu, H.M. Cheng, ACS Nano 4 (2010) 5835.

[13] E. Frackowiak, K. Jurewicz, S. Delpeux, F. Béguin, J. Power Sources 97-98 (2001) 822.

[14] T. Bordjiba, M. Mohamedi, L.H. Dao, Adv. Mater. 20 (2008) 815.

[15] K. Makgopa, P.M. Ejikeme, C.J. Jafta, K. Raju, M. Zeiger, V. Presser, K.I. Ozoemena, J. Mater. Chem. A 3 (2015) 3480.

[16] B. Xu, F. Wu, R. Chen, G. Cao, S. Chen, Z. Zhou, Y. Yang, Electrochem. Commun. 10 (2008) 795.

[17] E. Frackowiak, F. Béguin, Carbon 40 (2002) 1775.

[18] B.J. Landi, M.J. Ganter, C.D. Cress, R.A. DiLeo, R.P. Raffaelle, Energy Environ. Sci. 2 (2009) 638.

[19] K.S. Subrahmanyam, S.R.C. Vivekchand, A. Govindaraj, C.N.R. Rao, J. Mater. Chem. 18 (2008) 1517.

[20] M.T. Pettes, H. Ji, R.S. Ruoff, L. Shi, Nano Lett. 12 (2012) 2959.

[21] W. Zhang, C. Ma, J. Fang, J. Cheng, X. Zhang, S. Dong, L. Zhang, RSC Adv. 3 (2013) 2483.

[22] X.-C. Dong, H. Xu, X.-W. Wang, Y.-X. Huang, M.B. Chan-Park, H. Zhang, L.-H. Wang, W. Huang, P. Chen, ACS Nano 6 (2012) 3206.

[23] F. Deng, L. Yu, G. Cheng, T. Lin, M. Sun, F. Ye, Y. Li, J. Power Sources 251 (2014) 202.

[24] Y. Gogotsi, P. Simon, Science 334 (2011) 917.

[25] L. Zhang, J. Wang, J. Zhu, X. Zhang, K. San Hui, K.N. Hui, J. Mater. Chem. A 1 (2013) 9046.

[26] A. Gupta, A.J. Akhtar, S.K. Saha, Mater. Chem. Phys. 140 (2013) 616.

[27] V. Augustyn, P. Simon, B. Dunn, Energy Environ. Sci. 7 (2014) 1597.

[28] T. Yan, R. Li, Z. Li, Mater. Res. Bull. 51 (2014) 97.

[29] J. Fang, M. Li, Q. Li, W. Zhang, Q. Shou, F. Liu, X. Zhang, J. Cheng, Electrochim. Acta 85 (2012) 248.

[30] Y. Tao, L. Ruiyi, L. Zaijun, L. Junkang, W. Guangli, G. Zhiquo, RSC Adv. 3 (2013) 19416.

[31] M. Li, J.E. Zhu, L. Zhang, X. Chen, H. Zhang, F. Zhang, S. Xu, D.G. Evans, Nanoscale 3 (2011) 4240.

[32] Y. Song, J. Wang, Z. Li, D. Guan, T. Mann, Q. Liu, M. Zhang, L. Liu, Microporous Mesoporous Mater. 148 (2012) 159.

[33] X. Cai, X. Shen, L. Ma, Z. Ji, C. Xu, A. Yuan, Chem. Eng. J. 268 (2015) 251.

[34] Z. Gao, J. Wang, Z. Li, W. Yang, B. Wang, Chem. Mater. 23 (2011) 3509.

[35] Z. Wang, X. Zhang, J. Wang, L. Zou, Z. Liu, Z. Hao, J. Colloid Interface Sci. 396 (2013) 251.

[36] R. Ma, X. Liu, J. Liang, Y. Bando, T. Sasaki, Adv. Mater. 26 (2014) 4173.

[37] Z. Fan, J. Yan, T. Wei, L. Zhi, G. Ning, T. Li, F. Wei, Adv. Funct. Mater. 21 (2011) 2366.

[38] G. Yu, L. Hu, M. Vosgueritchian, H. Wang, X. Xie, J.R. McDonough, X. Cui, Y. Cui, Z. Bao, Nano Lett. 11 (2011) 2905.

[39] J. Zhang, J. Jiang, H. Li, X.S. Zhao, Energy Environ. Sci. 4 (2011) 4009.

[40] J. Shen, C. Yang, X. Li, G. Wang, ACS Appl. Mater. Interfaces 5 (2013) 8467.

[41] Y. Wimalasiri, R. Fan, X.S. Zhao, L. Zou, Electrochim. Acta 134 (2014) 127.

[42] K.S. Novoselov, A.K. Geim, S. V Morozov, D. Jiang, Y. Zhang, S. V Dubonos, I. V Grigorieva, A.A. Firsov, Science 306 (2004) 666.

[43] W.A. de Heer, C. Berger, X. Wu, P.N. First, E.H. Conrad, X. Li, T. Li, M. Sprinkle, J. Hass, M.L. Sadowski, M. Potemski, G. Martinez, Solid State Commun. 143 (2007) 92.

[44] S. Stankovich, D. A Dikin, G.H.B. Dommett, K.M. Kohlhaas, E.J. Zimney, E. A Stach, R.D. Piner, S.T. Nguyen, R.S. Ruoff, Nature 442 (2006) 282.

[45] Y. Hernandez, M. Lotya, D. Rickard, S.D. Bergin, J.N. Coleman, Langmuir 26 (2010) 3208.

[46] W.H. Jr, R. Offeman, J. Am. Chem. 80 (1958) 1337.

[47] Y. Wimalasiri, L. Zou, Carbon 59 (2013) 464.

[48] C. Mattevi, H. Kim, M. Chhowalla, J. Mater. Chem. 21 (2011) 3324.

[49] K.S. Kim, Y. Zhao, H. Jang, S.Y. Lee, J.M. Kim, K.S. Kim, J.-H. Ahn, P. Kim, J.-Y. Choi, B.H. Hong, Nature 457 (2009) 706.

[50] X. Li, W. Cai, J. An, S. Kim, J. Nah, D. Yang, R. Piner, A. Velamakanni, I. Jung, E. Tutuc, S.K. Banerjee, L. Colombo, R.S. Ruoff, Science 324 (2009) 1312.

[51] S.-Y. Kwon, C. V Ciobanu, V. Petrova, V.B. Shenoy, J. Bareño, V. Gambin, I. Petrov, S. Kodambaka, Nano Lett. 9 (2009) 3985.

[52] A. Bello, O.O. Fashedemi, J.N. Lekitima, M. Fabiane, D. Dodoo-Arhin, K.I. Ozoemena, Y. Gogotsi, A.T. Charlie Johnson, N. Manyala, AIP Adv. 3 (2013) 082118.

[53] A. Bello, M. Fabiane, D.Y. Momodu, S. Khamlich, J.K. Dangbegnon, N. Manyala, J. Solid State Electrochem. 18 (2014) 2359.

CHAPTER 2

2.0 LITERATURE REVIEW

2.1 Charge storage – Basic design

The concept of charge storage in most electrochemical devices like batteries, fuel cells, electrochemical capacitors is structured around the assembly of two main electrodes placed closely with a dielectric between the electrodes. The electrode pair is usually placed in an electrolyte containing ions which determine the nature of the charge storage process. Batteries chemically store bulk energy by an internal charge accumulation process while electrochemical capacitors (ECs) store bulk energy with a surface phenomenon [1–3]. Chemical storage in batteries give them a high storage capacity (energy density) over ECs; however, they are often saddled with a short cycle life problem and poor power delivery [4]. ECs on the other hand, can be fully charged and discharged in seconds and this gives them a better cycle life with a higher power density but a lower energy density capability as compared to batteries.

Figure 2.1 shows the relationship between the energy density and power density displayed on a Ragone plot for different energy storage systems. The figure presents the energy densities of various energy storage devices, measured along the horizontal axis, versus their corresponding power densities, measured along the vertical axis. It is seen that supercapacitors (SCs or ultracapacitors) occupy a region between conventional

electrolytic capacitors and batteries. Supercapacitors are still yet to match the energy densities of lithium ion or hybrid batteries and fuel cells despite greater capacitances than electrolytic capacitors. Although most of the literature in existence has focused on developing improved types or classes of supercapacitors by developing novel nanostructured materials with enhanced properties, there is an urgent need to make their energy densities more comparable to those of batteries if they are to be applied as stand-alone energy storage units.

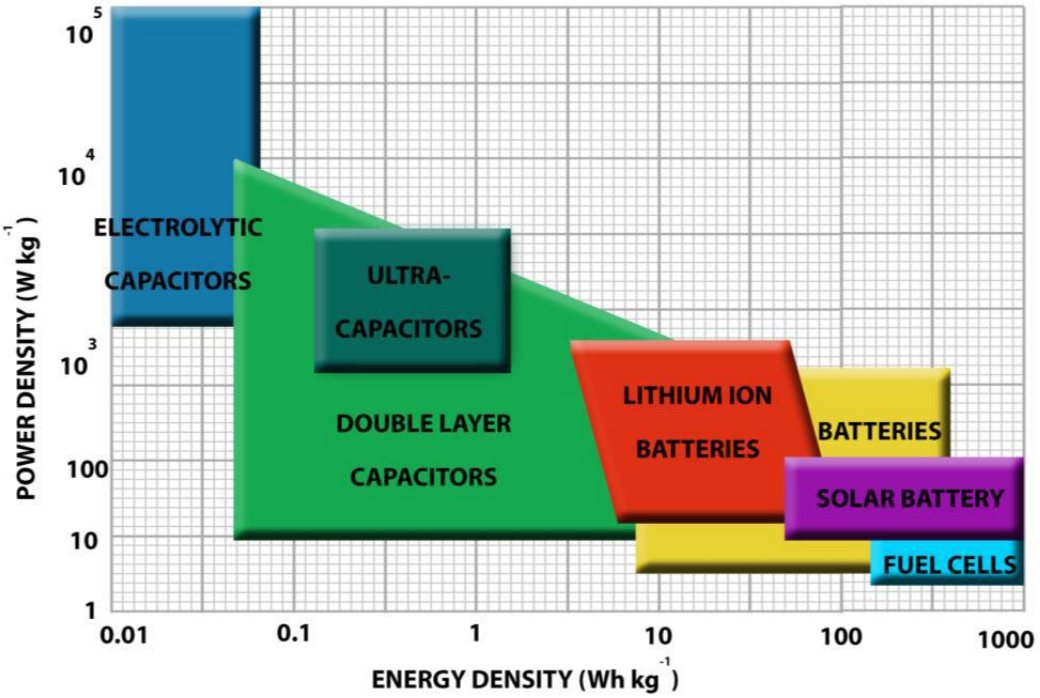

Figure 2.1: Ragone plot showing variation of energy density and power density for common energy storage devices (adapted from ref. [5]).

2.2 Electrochemical capacitors: Principle of energy storage

Electrochemical capacitors (ECs), Ultracapacitors (UCs) or Supercapacitors (SCs) can be broadly classified into three (3) main types based on their mechanism of energy storage namely;

(i) Electric Double Layer Capacitors (EDLCs)

(ii) Redox Electrochemical Capacitors (RECs) or Pseudocapacitors

(iii) Hybrid Electrochemical Capacitors (Hy-ECs)

A chart presenting an overview of each of these classes of electrochemical capacitors with their sub-groups and common electrode material is presented in figure 2.2 to give a clearer understanding.

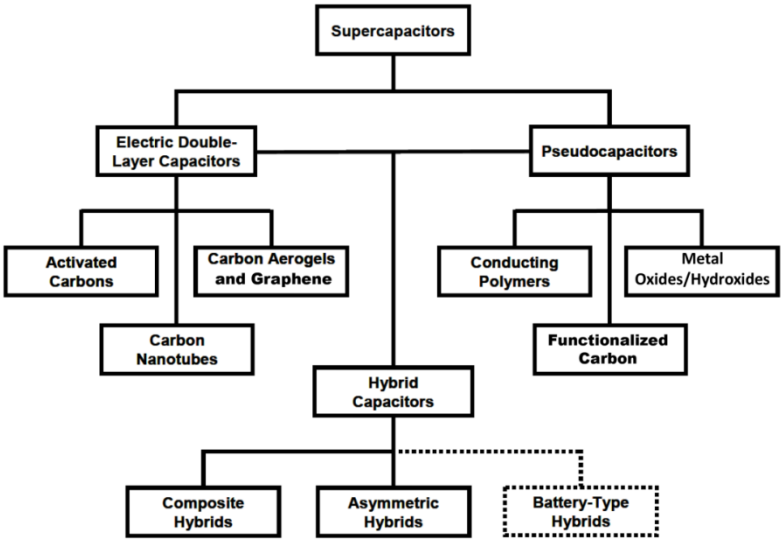

Figure 2.2: Classification of Electrochemical Capacitors.

2.2.1 Electric Double Layer Capacitors (EDLCs)

2.2.1.1 Theory and Operation mechanism

Electrochemical capacitors store charge based on pure electrostatic charge accumulation at the electrolyte/electrode interface. They are usually composed of a pair of polarizable electrodes which can store or supply charges by non-Faradaic or electrostatic processes. In this process, there is absolutely no transfer of charges across a phase boundary (electrode/electrolyte interface) and the oxidation state of the electroactive species that partake in the charge transfer process remain unaltered. The process relies solely on the potential gradient and electric field created within the system. The characteristics of the EDL are dependent on the surface structure of the electrode, the electrolyte composition and the potential field between the charges at the interface [6]. When the electrode is subjected to a negative or positive current as the case may be, the outer electrode surface electrostatically attracts oppositely charged ions from the electrolyte. These ions diffuse across the separator and align themselves uniformly on the pores of entire outer surface thus creating an electric field which allows the storage of energy by the capacitor. Figure 2.3 shows a schematic representation of an electrochemical capacitor with the electrode/electrolyte interface enlarged to further elucidate the diffusion of ions within the porous structure of the active electrode material. The electrode material consists of pores that serve as a site for the transport of mobile ions of opposite charge from the electrolyte when a potential (V) is applied and stores the charge by electrostatic force.

During the charging process of the SC, the ions migrate to the polarized electrodes of opposite charge within the electrolyte and electrons are transferred from the positive electrode to the negative electrode through an external source of current.

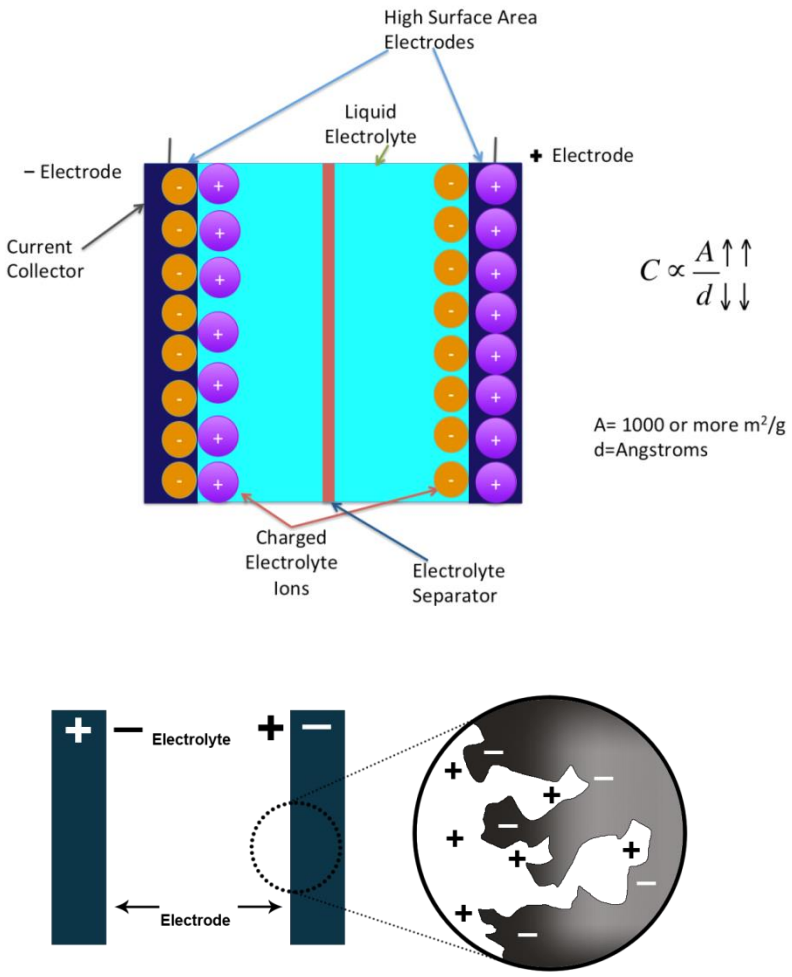

Figure 2.3: Schematic Illustration of a simple electrochemical cell showing the diffused ion-electrode material interaction.

Subsequently when the SC is discharging, the reverse takes place and ions are released from the electrode into the electrolyte [7].

In an ideal EDLC system, since there is no charge transfer across the electrode/electrolyte interface, there are no chemical or compositional changes associated with them and the electrolyte concentration should remain the same during charging and discharging [8]. Thus, charge storage in EDLCs is highly reversible and allows them to be cycled continuously with a high stability. Ionic recombination is also prevented due to the nature of the electrodes which creates a double layer (DL) charge configuration at each electrode. This double layer of charge accompanied with the high surface area from the porous carbon materials commonly used, gives EDLCs the ability to achieve higher energy densities than electrolytic capacitors and better cyclic stability than batteries [9–11].

Thus, the electrochemical processes (charging and discharging) for a double-layer capacitor can be expressed as [7,8,12]:

AT THE POSITIVE ELECTRODE

$$E_{S1} + A^- \xrightarrow{CHARGING} E^+{}_{S1} // A^- + e^- \quad (1)$$

$$E^+{}_{S1} + A^- + e^- \xrightarrow[DISCHARGING]{} E_{S1} + A^- \quad (2)$$

ON THE NEGATIVE ELECTRODE

$$E_{S2} + C^+ + e^- \xrightarrow{CHARGING} E^-{}_{S2} // C^+ \quad (3)$$

$$E^-{}_{S2} + C^+ \xrightarrow[DISCHARGING]{} E_{S2} + C^+ + e^- \quad (4)$$

A combination of the overall charge and discharge process on both electrodes can be expressed as:

$$E_{S1} + E_{S2} + A^{-}C^{+} \Leftrightarrow E^{+}{}_{S1} // A^{-} + E^{-}{}_{S2} // C^{+} \quad (5)$$

where E_s denotes the electrode surface, // represents the double layer (DL) where charges are accrued on both sides, A^- and C^+ are abbreviations for the anions and cations, respectively within the electrolyte.

As observed from the overall reaction, the "A^-C^+" material can be taken to be a salt which is consumed during the charging process and regenerated during the discharging process. Thus, the electrolyte can be considered as an active material that partakes in the entire process [12]. The charge density at the electrode interface changes with a simultaneous change in the concentration of the salt and electrolyte conductivity during the charge and discharge process. However, one important point to note is that the amount of ions involved in building the DL is exactly the same as the number of charges developed on the electrodes.

A simplified figure of the orientation of charges and ions at the electrode/electrolyte interface is shown in figure 2.4 which is basically the electrolytic capacitor configuration. It can be seen from the figure that each electrode of the EDLC exists as a single capacitor of capacitance C_i (i = 1, 2) which is related to the area (A) and permittivity ε by the traditional electrolytic capacitor equation:

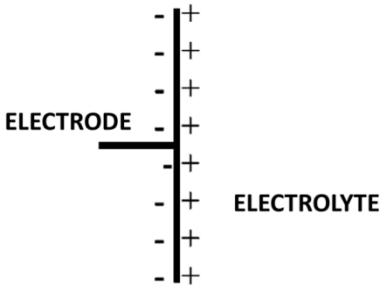

Figure 2.4: Orientation of charges at the electrode/electrolyte interface of an EDLC.

$$C_i = \frac{\varepsilon A_i}{d_i} \qquad (6)$$

where ε is related to the permittivity of the medium in relation to ε_o, which is the permittivity of free space (8.854 x 10^{-12} F m^{-1}) and *d* is the distance between the centers of ion and porous electrode surface (of the order of molecular dimensions) respectively.

Nevertheless, several controversial observations have been made by different authors [13,14] who have described significant deviations from this simple law. Their views were interpreted either as an “ion size effect” or “non-accessibility of small micropores within the electrolyte”. The limitation in capacitance is attributed to a space constriction for charge accommodation within the walls of the pore [15]. Other related factors which also affect the measured capacitance include; charge screening; quantum capacitance; electrochemical doping of density of states; pore size distribution within the electrode material etc. Thus, charge storage is carried out through reversible ion adsorption onto the electrode surface at the electrode/electrolyte interface.

The “electrochemical active surface area” is defined based on the limitations described above and is described as the useful accessible surface area where charge storage reactions take place within the electrode. The pore size of the electrode material also has a great effect on the measured capacitance [16]. For achieving maximum double layer capacitance, it has been reported in an earlier study by Largeot *et al*. [17] that the pore size of the electrode material was close to the electrolyte ion size. For other larger to smaller pores, there was no successful charge storage and this led to a significant capacitance loss. In addition, a direct increase of the pore size also increases the average distance between the pore walls and the centre of the electrolyte ion which also reduces capacitance. This is expressed as [8]:

$$C = \frac{A\,\varepsilon}{4\,\Pi\,d} \tag{7}$$

where ε the local dielectric constant of the electrolyte with respect free space ε_o, d is the separation between carbon and ions and A is the surface area.

This reduction is further elucidated by a computational analysis done by Mathew *et al*. [18], and termed “interfacial confinement effects”. From their findings, an atomic scale depiction of ion transport dynamics in aqueous electrolyte which provides the platform for the examination of size trends within specific geometries is described as well as trends in concentration. A modeling of the electrode pores as planar graphite sheets to facilitate focused ion motion is done under confined conditions. An enhancement to the ionic diffusivities in the pore direction is observed which decreases with further

confinement. These findings from the simulation provide a strong evidence of charge separation perpendicular to the surface for all size scales, ion types and concentration which creates a useful baseline for examining different capacitance behavior and energy storage [18].

The porosity relevant for improving capacitance is quite complex involving both pore size and pore size distribution for a given specific surface area (m^2 g^{-1}) of an electrode material. Pore size distribution in the range of 2 – 5 nm which is larger than the size of double solvated ions has been identified as a way of enhancing energy and power of electrochemical capacitors [4]. Therefore, ECs greatly rely on the electrochemical active surface area for any significant energy storage capability.

Some established theoretical models related to determining the specific capacitance (per unit surface area) of EDLCs are based on classical theories [19–22] and are further explained in much recent reports [7,23]. In most models, it is suggested that the accumulation of ions close to the electrode surface caused the formation of a “diffusive layer” within the electrolyte.

The double layer capacitance was initially modeled and described by Helmholtz in the 19th Century. His model states that two adjacent layers of opposite charges are created and concentrated at the electrode/electrolyte interface mimicking the conventional parallel plate capacitor [19]. He further described the different sizes of ions with respect to their surface reactivity. Chemical affinities of the ions to the surface of the electrode and the EDL field strength are the determining factors for the adsorption process in the EDL. In practice however, the EDL structure is more complex than the Helmholtz model

tried to describe it. This model failed to describe other phenomena which take place at the DL region such as the diffusion of ions in the solution and the interaction between the dipole moment of the solvent and the electrode [24].

Thus, Gouy and Chapman subsequently modified the Helmholtz model. They proposed a diffusion model of the EDL in which the potential decreases exponentially from the electrode surface to the bulk liquid and the continuous distribution of ions determined by thermal motion within the electrolyte [20,21]. However, this model leads to an over-estimation of the capacitance value in highly charged DLs and was further modified by H. Stern [22].

The Stern model involved the combination of both the Helmholtz and the Gouy-Chapman models by accounting for the hydrodynamic motion of the ionic species in the diffuse layer and the accumulation of ions close to the electrode surface with a clear identification of two regions of ion distribution namely; the inner region known as the compact layer and the outer region called the diffuse layer. The total EDL capacitance (C_{DL}) in this case, is the combination of the capacitance contributions from both regions represented as a series of capacitors at the electrode/electrolyte interface expressed as [22]:

$$\frac{1}{C_{DL}} = \frac{1}{C_Q} + \frac{1}{C_D} \tag{8}$$

where C_Q is the compact double layer capacitance and C_D is the diffusion layer capacitance.

Ions are mostly hydrated in the compact layer and thus, are strongly adsorbed by the electrode, which makes them refer to it as a “compact layer”. Furthermore, the compact layer also contains precisely adsorbed ions (generally anions irrespective of the charge nature of the electrode) and other adsorbed counter-ions. The diffuse layer is extensively described by the Gouy-Chapman model described earlier in refs. [15] and [16].

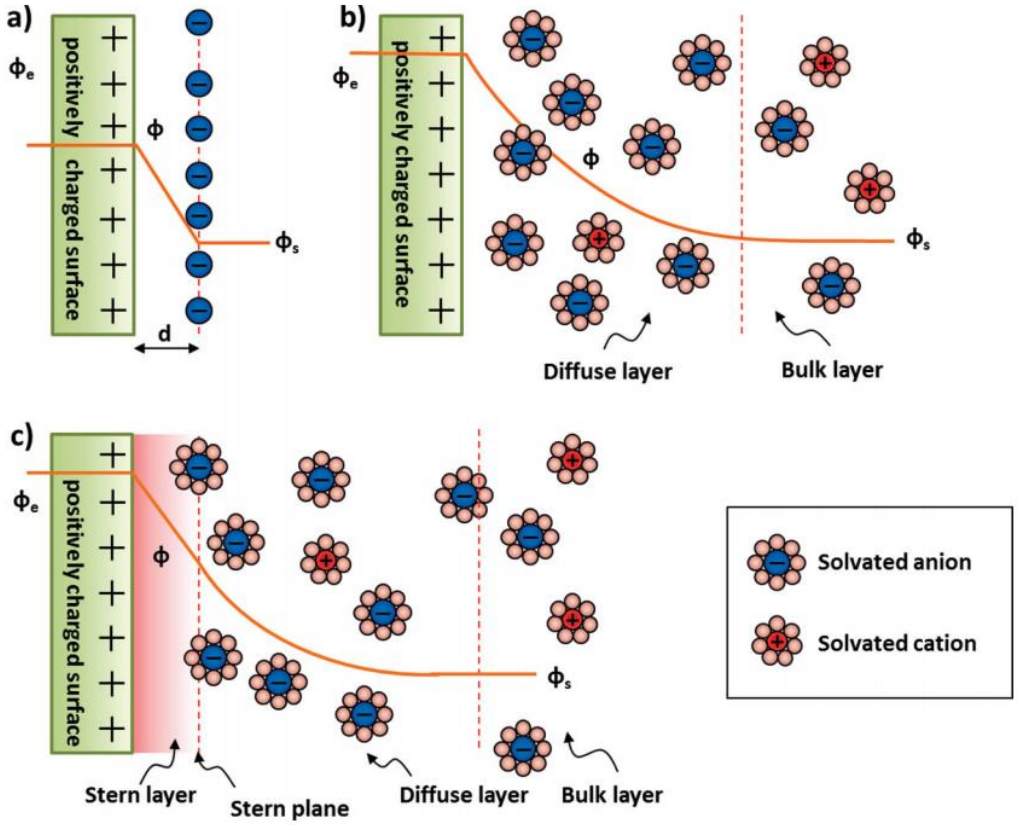

Figure 2.5: Schematic showing (a) Helmholtz, (b) Gouy-Chapman, and (c) Stern model of the electrical double-layer on a positively charged electrode in an aqueous electrolyte (adapted from [24])

The performance characteristics of an EDLC can also be adjusted by changing the nature of the electrolyte. An EDLC works best in either an aqueous or organic electrolyte depending on the material component of the active electrode. Aqueous electrolytes, such as potassium hydroxide (KOH), sodium sulfate (Na_2SO_4) and sulfuric acid (H_2SO_4), generally have a lower equivalent solution resistance (R_s), lower minimum pore size requirements due to their characteristic ion sizes and are cheaper in price compared to organic electrolytes, such as acetonitrile, propylene carbonate and tetrahydrofuran.

Nonetheless, organic electrolytes have higher breakdown voltages which create the opportunity of reaching higher voltage windows which implies higher energy density when using them for device applications. Therefore, in choosing between the former and latter, there is a need to compromise between the capacitance, solution resistance R_s, operating voltage, and device cost [2,3,9]. For these reasons, the electrolyte choice often depends on the proposed application of the EDLC. Although the nature of electrolyte is very important for an efficient enhancement of the performance of supercapacitors, comparison of different electrolyte types is not within the scope of this thesis, and as such will only be revisited and discussed briefly when describing the material components of a supercapacitor in section 2.3.

2.2.1.2 Electrode Materials for EDLCs

The main electrode materials widely utilized as electrode materials in EDLCs are the carbon-based materials due to their abundance, low cost, large surface area/porosity, good electronic conductivity, facile synthesis route, robust surface chemical

environment and high chemical stability. Chemical activation and template carbonization amongst other various techniques are processes recently adopted to produce different forms of porous carbon materials with exceptionally large specific surface areas and finely tuned porosity [25,26]. The storage mechanism is electrostatic in nature with charges stored at the electrode/electrolyte interface. Thus, the capacitance predominantly depends on the available surface area. The measured specific capacitance values of these carbon-based materials ranges from 50 - 200 F g^{-1} in aqueous electrolytes, 30-100 F g^{-1} in organic electrolytes and 20-70 F g^{-1} in ionic electrolytes.

Typical carbon materials used as supercapacitor electrodes include activated carbons (ACs) [27,28], carbon nanotubes (CNTs) [29,30], graphene [31], carbon nanofibres (CNFs) [32], template porous carbons (TPCs) [33] and onion like carbons (OLCs) [34,35], etc. OLCs are zero-dimensional ("quasi 0D") quasi-spherical nanoparticles containing concentric graphitic shells materials prepared by annealing nanodiamond powders in vacuum or argon and by detonation of nanodiamond, giving rise to bulk nanoparticles of a few nanometres. The first three carbon materials listed are the most investigated materials and will now be discussed.

(I) *Activated carbon*

Activated carbons (ACs, shown in figure 2.6) are the most commonly used electrode material in EDLCs because of their excellent surface area coupled with their complex

porous structure and low-cost. For this reason, tuning the pore size distribution of the active electrode material should enhance the performance of energy storage devices.

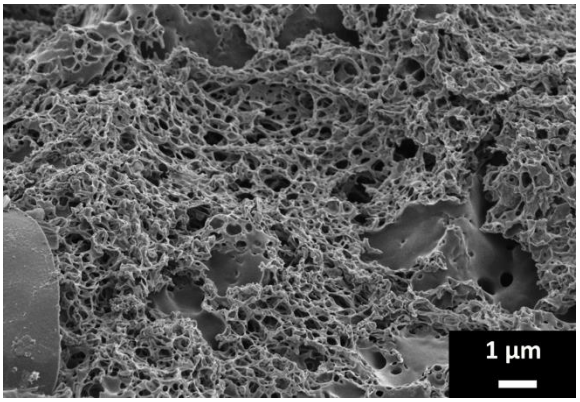

Figure 2.6: Scanning electron microscopy image of activated carbon

Generally, researchers have focused on establishing an optimized pore size for the activated carbon in a particular electrolyte in order to adopt this for producing high quality active material with improved capacitive properties. By varying the temperature of activation, studies done by Herawan and co-workers [36] report that for a fixed activation time coupled with varying temperatures between 500-700°C, yields higher surface area and could lead to obtaining larger specific surface area within the active carbon matrix.

Earlier reports by Conway [9] show that the larger pore sizes correspond to higher power densities while smaller pore sizes correspond to higher energy densities. The relationship between the specific surface area, pore volume, average pore size and pore size distribution of ACs with their specific capacitance has also been extensively investigated by Shi *et al.* [37]. It was found that the capacitance of ACs is not linearly

related to the surface area and different pores sizes are characterized with different capacitance per unit surface area. For example, the specific capacitance of micropores is larger than that of mesopores.

Bello *et al*. [26] also fabricated symmetric EDLCs based on a porous three dimensional interconnected carbon framework using graphene foam (GF) and polyvinyl alcohol (PVA) as the sacrificial template. The high surface area activated carbon exhibited a specific capacitance of 65 F g^{-1} with a corresponding energy density and power density value of 12 Wh kg^{-1} and 400 W kg^{-1} respectively. This was attributed to the highly porous interconnected framework with mesoporous walls and microporous texture which are suitable as electrode for energy storage.

Surface area is generally increased by the development of porosity within the bulk of carbon materials giving it a characteristic porous network suitable for storing charge. For activated carbon, recorded specific capacitances range from 100 – 200 F g^{-1} [26] in an aqueous electrolyte and 80 – 100 F g^{-1} for those tested in an organic electrolyte [38,39].

(II) *Carbon nanotubes*

After their discovery in recent years, researchers have focused on producing high quality carbon nanotubes (CNTs) materials with improved morphological and electrical properties. This increased interest is due to their great potential for use as EDLC materials due to their open and accessible network of mesopores in the form of an entangled mat [24,40]. Unlike the other carbon based materials, their tubes are

interconnected (figure 2.7) which gives room for a continuous charge distribution that uses all of the available surface area.

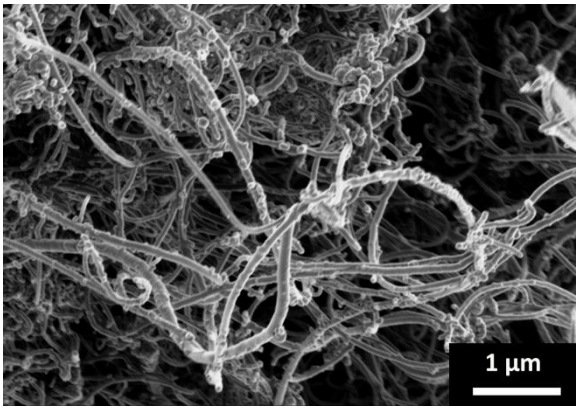

Figure 2.7: Scanning electron microscopy image of carbon nanotubes

Carbon nanotubes (CNTs) which are one-dimensional ("quasi 1D"), have been extensively studied for electrochemical capacitors in the past few years due to their unique pore structure, superior electrical properties, good mechanical and thermal stability. CNTs can be categorized as single-walled carbon nanotubes (SWCNTs), double-walled carbon nanotubes (DWCNTs) and multi-walled carbon nanotubes (MWCNTs), all of which have been widely explored as energy storage electrode materials. However, their preparation techniques are quite complicated to carry out and the energy density obtained from use of these materials as SC electrodes is relatively small due to their limited specific surface area (< 500 $m^2 g^{-1}$) as compared to ACs.

However, in special cases, most of the surface area is maximally utilized to achieve high capacitance even comparable to some activated carbon-based ECs. This is possible

because the problem of ion misfit is almost absent in this case since most electrolyte ions can easily diffuse into the mesoporous network. Their higher conductivity also gives them a lower equivalent series resistance (ESR) value as compared to activated carbon. Therefore, there is a high possibility of obtaining specific capacitance values close to those of highly porous activated carbons which implies improved energy densities and a corresponding reduction in the ESR which would greatly enhance their power density.

(III) *Graphene*

The interest in graphene has increased ever since its discovery by Novoselov and co-workers in early 2004 [41,42]. Its unique and extraordinary properties such as excellent electronic transport ability, tunable band gap, great mechanical strength, large surface area, excellent optical characteristics and thermal conductivity etc., has made it an exciting and suitable candidate for numerous applications [43,44].

Graphene, a 2-dimensional (2D) allotrope of carbon with its honeycomb network (schematic as shown in figure 2.8) constitutes a one-atom thick sheet of sp^2 bonded carbon atoms and this makes it the basic building block of other carbon allotropes of different dimensionalities with dissimilar electrochemical properties.

Graphene is a zero band gap semiconductor that shows a linear dispersion at high symmetry point in the reciprocal space and results in an effective dynamics of electrons similar to that of massless relativistic Dirac fermions [45].

These properties are summarized in Table 1 showcasing all the allotropes of carbon with their detailed properties quantitatively expressed. The excellent theoretical surface area

has attracted its application as a potential electrode material for ECs. Conversely, the experimental specific capacitance value obtained is only about 262 F g^{-1} in aqueous electrolytes [46–48].

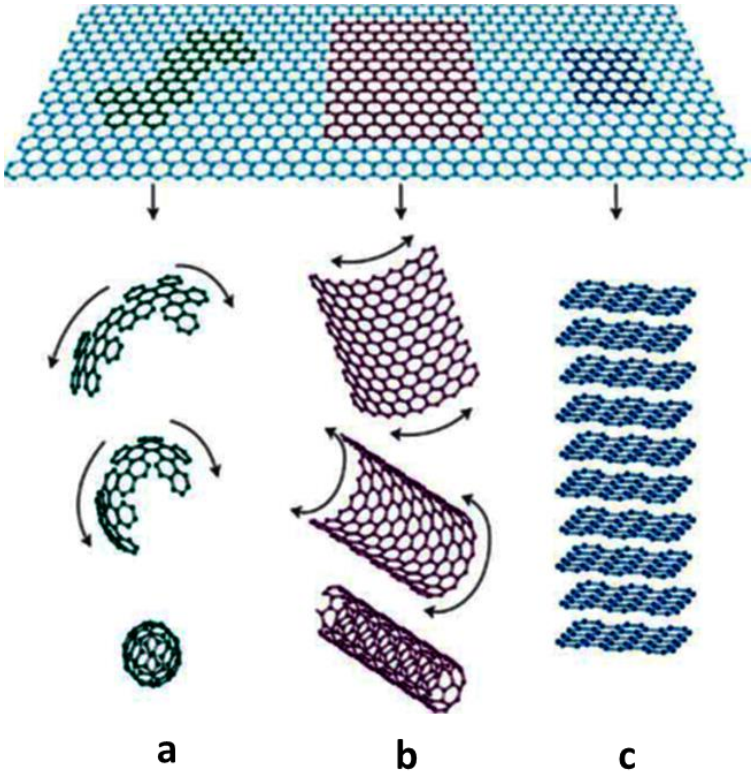

Figure 2.8: Graphene, mother of all graphitic forms; can be wrapped up into 0D buckyballs, rolled into 1D nanotubes or stacked into 3D graphite (adapted from [49])

The limited capacitance value has been attributed to the high tendency of graphene sheets to restack themselves owing to the strong π- π bond interaction between the neighboring sheets leading to significant decrease in the available surface area for electrolyte ions and consequently low specific capacitance value for the pure graphene-based SCs.

In order to prevent this problem, it is necessary to functionalize graphene with chemical functional groups such as the carbonyl and hydroxyl groups [3,31] or attach them with highly pseudocapacitive or faradaic materials such as polymers, metal oxides and metal hydroxides [50,51]. This process does not only prevent the restacking problem but also enhances the electrochemical performance by adding to the overall EDL capacitance [52–54]. With regards to the grafting with faradaic-like materials, several hybrid composites of graphene (or reduced graphene oxide) have been studied and reported. Composites such as polymer-graphene [51,55] and graphene-metal oxides/graphene-metal hydroxides [56–58] have all been investigated and the results from the numerous studies listed showed that the performance of the ECs depends on the structure and porosity of the electrode.

Recently, a 3D network of graphene foam (GF) was also synthesized by template-directed chemical vapor deposition and studied by Chen *et al*.[59] in order to provide high quality and conductive interconnected graphene sheet network with excellent electrical and mechanical properties. The graphene foam is characterized with a unique porous structure that can provide an avenue for the free movement of ions within the structure when used for EC applications. Significant efforts have further been made on synthesis of GF-composites [60–62] as electrode materials for SC applications. However, there is still a need for further extensive studies to develop and improve the available studies reported so far in order to fully optimize the potential of graphene-based ECs.

Thus, this thesis explores the effect of incorporating graphene foam into the active matrix of faradaic-type materials with an attempt to fully analyze and understand the

effect of the addition to the electrochemical properties of the SC electrode materials. The results obtained can be used to develop active supercapacitor electrodes with improved specific capacitance and stability for complete energy storage devices.

Table 2: The properties of graphene and other carbon allotropes [4]**.**

Allotropes of Carbon	**Graphite**	**Diamond**	**Fullerene**	**Carbon nanotubes**	**Graphene**
Dimensionality	Three	Three	Zero	One	Two
Hybridization	sp^2	sp^3	mainly sp^2	mainly sp^2	sp^2
Crystal system	Hexagonal	Octahedral	Tetragonal	Icosahedral	Hexagonal
Experimental specific surface area ($m^2\ g^{-1}$)	~10-20	~20-160	~80-90	~1300	~2675
Density (gcm^{-3})	2.09-2.23	3.5-3.53	1.72	>1	>1
Electrical conductivity ($S\ cm^{-1}$)	Anisotropic $2{,}3 \times 10^{4a}$, 2.3×10^{6b}		10^{-10}	Depends on the particular structure	2000
Electronic properties	Conductor	Insulator, semiconductor	Insulator	Depends on structure. Can be metallic or semiconductin g	Semimetal, zero gap semiconductor
Thermal conductivity ($W\ m^{-1}\ K^{-1}$)	1500-2000[a] 5-10[c]	900-2320	0.4	3500	4848-5300
Hardness tenacity	High	Ultrahigh	Highly elastic	High flexible elastic	Highest flexible elastic (single layer)
Optical properties	Uniaxial	Isotropic	Non-linear optical response	Structural dependent	97.7% optical transmittance
[a]a-direction	**[b]b-direction**	**[c]c-direction**			

2.2.2 Pseudocapacitors (PCs or Redox Electrochemical Capacitor)

2.2.2.1 Theory and Operation mechanism

Pseudocapacitors (or RECs) faradaically store charge through the transfer of charges between the electrode and electrolyte unlike EDLCs, which store charge electrostatically. Earlier studies by Conway [9], reports that electrochemical charge storage in pseudocapacitors occurs based on certain faradaic mechanisms present and these include; electrosorption (underpotential deposition), reduction-oxidation reactions (redox pseudocapacitance) and intercalation (intercalation pseudocapacitance). Pseudocapacitance is described to arise due to charge acceptance (ΔQ) and a voltage change (ΔV). It also involves the passage of charges across the double layer so that the capacitance C (which is Faradaic in nature) is obtained from the derivative of the charge and voltage as:

$$C = \frac{d(\Delta Q)}{d(\Delta V)}. \quad (9)$$

The formation of an adsorbed surface monolayer from ions contained within the electrolyte on the electrode composed of a different metal which has a redox potential well above the former is termed “Underpotential deposition”. For example, the deposition of lead (Pb) on the surface of a gold (Au) electrode [63].

The electrochemical adsorption of ions onto the surface or near the surface of an electrode material accompanied with a related faradaic charge transfer is described as “Redox pseudocapacitance” while “Intercalation pseudocapacitance” arises from the

intercalation of ions into the layers or pores of pseudocapacitive materials accompanied with a faradaic charge transfer with no crystallographic phase change [9].

These above explained mechanisms occur with different materials and due to independent processes. The similarity in electrochemical signatures occurs due to the relationship between the potential (*V*) and the generated charge (Q) as a result of the adsorption/desorption processes at the electrode/electrolyte interface or within the inner layers of the electrode material surface.

The significant difference between materials suitable for pseudocapacitors and batteries lies in the surface reactions. Battery materials utilize the bulk solid state to store charges which gives them their high energy densities while pseudocapacitive materials are not limited by solid state diffusion and the utility of energy storage is based on a kinetic behavior [64]. This gives them their characteristic high rate capability as compared to batteries where a limited solid-state diffusion between the anode and cathode inhibits its power capability [65]. These processes are clearly shown by a schematic diagram in figure 2.9 where the different types of reversible redox mechanisms which bring about pseudocapacitance are illustrated.

Pseudocapacitance could be intrinsic or extrinsic in nature. Intrinsic pseudocapacitance materials are those which display redox-capacitive charge storage for a wide range of particle sizes and morphologies while extrinsic pseudocapacitance materials do not exhibit any pseudocapacitance in a bulk state due to phase transformation during ion storage [64].

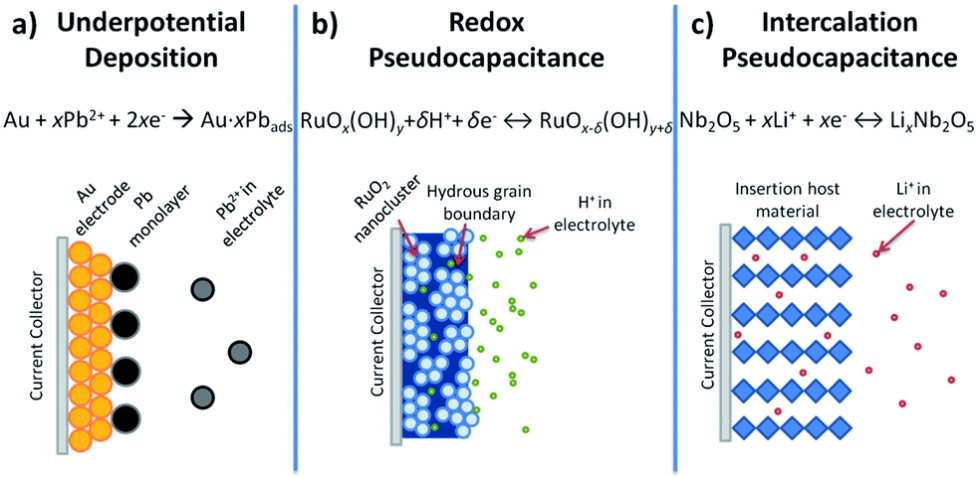

Figure 2.9: Schematic showing various types of reversible redox mechanisms that give rise to pseudocapacitance (adapted from [64])

With extrinsic pseudocapacitive materials, nano-structuring to improve their surface area enhances their rate capacity behavior due to a decrease in diffusion distance and in some cases decrease in phase transformation. Examples of intrinsic pseudocapacitance materials include RuO_2 [66], MnO_2 [67], Nb_2O_5 [68] and a widely used and very good example of extrinsic pseudocapacitive material is $LiCoO_2$ [69].

The most commonly studied pseudocapacitor or faradaic-like electrode materials are transition metal oxides [8,70,71], transition metal hydroxides [72–74], transition metal nitride [75,76] carbon material enriched with oxygen/nitrogen containing functional groups [77,78] etc. The choice of transition metals in most pseudocapacitor materials is due to the variable oxidation state of the metals. In general, a higher capacitance has been demonstrated for some of these materials as compared to EDLCs. This is due to

the faradaic charge transfer process which takes place at the electrode surface. The major drawback of these type of energy storage materials is however, their surface which is highly susceptible to degradation and redox-dependent solid state kinetics [30]. This leads to low power performance due to poor electrical conductivity and lower cycling stability when compared to pure EDLC-based materials.

Ruthenium dioxide was the first pseudocapacitive material discovered in 1971 [66] and have been extensively studied by researchers over time. Initial reports [66] from the first studies demonstrated low gravimetric capacitance values due to the fact that only 4–7% of the Ru^{4+} atoms participated in the redox reaction. However, it demonstrated the unique electrochemical features for typical pseudocapacitive processes. Furthermore, it also revealed the need for a porous and hydrous oxide as the bulk. An improvement in capacitance was observed in a subsequent study [79] to a higher value of over 700 F g^{-1} and this was linked to the mixed proton-electron conductivity (from the structural water, specifically, $RuO_2.nH_2O$ where n = 0.5) within the hydrous oxide.

The electrochemical storage reaction mechanism for RuO_2 electrodes can be expressed as [9,12]:

POSITIVE ELECTRODE

$$HRuO_2 \longleftrightarrow H_{1-\delta}RuO_2 + \delta H^+ + \delta e^- \quad (10)$$

NEGATIVE ELECTRODE

$$HRuO_2 + \delta H^+ + \delta e^- \longleftrightarrow H_{1-\delta}RuO_2 \quad (11)$$

OVERALL REACTION

$$HRuO_2 + HRuO_2 \longleftrightarrow H_{1-\delta}RuO_2 + H_{1-\delta}RuO_2 \quad (12)$$

where $0 < \delta < 1$, RuO_2 and $HRuO_2$ are representative of both the positive and the negative electrodes at fully charged states, respectively. $HRuO_2$ represents electrodes which are at a fully discharged state.

As stated earlier, the enhanced electrochemical performance of RuO_2.nH2O materials is related to its porous architecture, its high metallic conductivity as well as hydrous nature. From the above reaction (eqns. 10 - 12), the reversible redox transitions depend on both proton exchange and electron-hopping processes [8]. In addition, there is a migration of electrons through the external power source while protons migrate from one electrode to another during the charge and the discharge process. Although, no net ion exchange occurs between the electrode and the electrolyte, the electrolyte concentration may differ due to some polarization, some EDL formation and the presence of redox reactions during the entire charge/discharge process which is the reverse phenomenon in double-layer capacitor [4]. However, there is a limitation to adoption of this material for practical applications because of the high cost of the RuO_2. As such, numerous techniques have been adopted for the development of cheaper and environmentally safe materials which show similar promising properties compared to that of RuO_2. Other materials such as NiO, MnO_2, Fe_2O_3, Fe_3O_4, SnO_2, Co_3O_4 and transition metal- layered double hydroxide will be explored and elucidated in further sections.

2.2.2.2 Electrode Materials for Pseudocapacitors

Common electrode materials applied in RECs include; conducting polymers, transition metal oxides and transition metal hydroxides etc.

(I) Conducting polymers (CPs)

Conducting polymers (CPs) have received significant attention due to their vast range of properties which includes good pseudocapacitive behavior with an associated relatively high specific capacitance and a wide range of electrical conductivity which can be tuned by varying the doping levels while maintaining its mechanical flexibility and thermal stability [80]. Due to this reason, they have a low equivalent series resistance (ESR) value and devices with high specific power are feasible if properly fabricated.

The pseudocapacitive form of energy storage involves the faradaic processes of p- and n-doping. Basically, the n/p-type polymer configuration (with a negatively charged (n-doped) and a positively charged (p-doped) conducting polymer electrode) has the potential to fully exploit the maximum energy and power densities [10]. CPs have an excellent redox capability where ions are transferred to the polymer backbone from the electrolyte during oxidation and released back to the electrolyte during reduction.

However, inadequate n-doped conducting polymer materials have prevented their application in supercapacitors due to their limited capacitance values. In order to facilitate the n-doping process, numerous polythiophene derivatives have been synthesized. Nevertheless, understanding and tuning the structure of the thiophene units to amend the potential at which doping occurs has led to the production of

heavier molecules with increasing cost to the electrode material. Furthermore, a build-up of mechanical stress on the entire conducting polymer backbone during both the tuning process and faradaic reactions limits the stability of the overall device electrode during cycling involving galvanostatic charge-discharge process. CPs are also well known for large volumetric change and consequent polymer breakage during the same charge-discharge process especially when used alone in their pristine form [51]. Hence, the decreased cycling stability limits their development for CP-based EC applications.

The most commonly studied CPs for EC applications are polyaniline (PANI) [55,81], polythiophene (PTh) [82], polypyrole (PPy) [83], poly(3,4-ethylene-dioxythiophene) (PEDOT) [84] and composites of CP with other materials [85,86].

The specific capacitance (C_s) of a PANI nanofiber modified stainless-steel (SS) electrode (PANI/SS) assembled supercapacitors was reported as 524.9 F g^{-1} from the galvanostatic charge/discharge measurements in 1.0 M H_2SO_4 electrolyte by Li *et al*. [87] and compared with a theoretical mass specific capacitance (Cs) of polyaniline (PANI) which was firstly estimated by combining electrical double-layer capacitance and pseudocapacitance. The maximum specific capacitance obtained from these methods in the study was found to be about 26% of the theoretical value. Guan *et al*. [88] fabricated PANI fibers by interfacial polymerization in the presence of paraphenylenediamine (PPD) to tune their morphology and also improve their electrochemical properties. The specific capacitance of the fibers in the presence of PPD showed a higher specific capacitance of 548 F g^{-1} with a specific energy of 36 Wh kg^{-1} and power of 127 W kg^{-1} at a 0.18 A g^{-1} current density.

Wang *et al*. [89] also successfully demonstrated the synthesis of highly ordered P3HT:PCBM nanostructures via a slow-drying method and further analyzed their potential as supercapacitive electrodes. They found out that the nanowires possessed high capacitance which was attributed to their large surface area and open structure which can facilitate efficient ion transport and charge accumulation.

Another study on P3HT-graphene polymer composites [90] involved comparing an in-situ and ex-situ technique for synthesis in order to investigate their supercapacitive behavior since researchers had claimed that individual polymers alone were easily susceptible to breakage when used in their pristine form for SC applications. They discovered that the in-situ grown samples showed a better formation of the composite than the ex-situ samples based on the microstructural and photoluminescence spectra obtained coupled with a higher C_s of 323 F g^{-1} as compared to 244 F g^{-1} at a 200 mA g^{-1} current density. This was ascribed to the restacking of graphene layers and hydrophobic nature of the P3HT polymer chains present in the sample prepared by ex-situ technique which limited its charge storage capacity as compared to the in-situ where highly porous structures present in the composite creates access to electrolyte ions.

Recently, Zhou *et al*. [91] fabricated and analyzed the electrochemical characteristics of an asymmetric supercapacitor based on PEDOT-coated on aligned carbon nanotubes (CP/a-CNTs) and pristine aligned carbon nanotubes (a-CNTs) as the negative and positive electrode respectively. In the study, it was revealed that the CP/a-CNTs enhances charge storage while the a-CNTs morphology provides a straight and fast ion transport pathway. This enables the exhibition of a wide operating voltage window of up to 4.0 V

with an excellent maximum energy and power densities of 82.8 Wh L^{-1} and 130.6 KW L^{-1} in volumetric performance units. Thus, the incorporation of other materials into the active polymer matrix might be an initial step to addressing the instability and volume expansion issues associated with CPs when used as EC electrode material.

(II) Transition metal oxides/hydroxides (t-MO/t-MOH)

Transition metals exhibit variable oxidation states due to the relatively low reactivity of their unpaired *d* orbital electrons [92]. The electrons they use to combine with other elements (or valence electrons), are present in more than one shell. This is the reason why they are suitable choices for redox capacitor electrode materials where faradaic reactions take place. They also form stable metal oxide (t-MO) and hydroxide (t-MOH) nanostructures which are electrochemically active with the ability to interact with electrolyte ions over an appreciable voltage range.

Several t-MOs and t-MOHs such as Co_3O_4 [93–95], $Co(OH)_2$ [96], MnO_2 [97–99], NiO [100–102], $Ni(OH)_2$ [50], RuO_2 [103–105], SnO_2 [106], V_2O_5 [107,108] and VN [109–111] have been reported to store charge both electrostatically and by electrochemical faradaic reactions with promising trends on improved specific capacitance and associated energy densities. In order to be successfully applied as electrode materials for SCs, the oxides/hydroxides must be electronically conductive in nature; the constituting metals must also have the ability to exist in variable oxidation states with no phase change involving reversible modifications of its structure. Lastly, their

structure should be designed in such a way that protons can freely intercalate in/out of the lattice during redox reactions. Furthermore, the enhancement of the kinetics of ion and electron transportation within electrodes and at the electrode/electrolyte interface can highly improve electrochemical properties of SCs. Thus, fabricating electrodes with proper pore structure and good electrical conductivity is ideal.

Initial studies done by Zheng *et al.* [79] demonstrated the stability of hydrous RuO_2 prepared by a sol-gel method. The amorphous hydrated material was obtained after annealing the precursors at low temperatures and testing their electrochemical performance in an acid electrolyte. A specific capacitance value of 720 F g^{-1} was measured for the amorphous powder and this dropped considerably when the material was further subjected to temperatures above 175°C. This was attributed to the formation of a crystalline phase with a decreased surface area. Co_3O_4 have also been investigated for their potential use in ECs due to their variable oxidation states, which can yield surface redox reactions. A dense network of Co_3O_4 nanowire arrays were grown by a template-free growth method [95] on nickel foam followed by thermal at 300°C in air. Results from the electrochemical tests showed a specific capacitance value of 746 F g^{-1} at a current density of 5 mA cm^{-2} with a coulombic efficiency of ~93%.

MnO_2 mainly exhibits pseudocapacitance which is attributed to reversible redox reactions involving the exchange of protons and/or cations within the electrolyte. There is also the transition between oxidations states of Mn (III)/Mn (II), Mn (IV)/Mn (III), and Mn (VI)/Mn (IV) within the electrode potential window of the electrolyte [4]. For this

reason, they have been extensively analyzed as electrode materials for supercapacitor applications. Xu *et al*. [112] reports an ideal capacitive behavior for MnO_2 material in an aqueous electrolyte containing bivalent cations. In their work, they report a specific capacitance of 310 F g^{-1} with no loss in capacity after 600 cycles which indicates the good cycling stability for the MnO_2 electrodes. Another study by Bello *et al*. [99] involved fabricating a symmetric capacitor based on MnO_2-based composites with graphene. In their study, they hydrothermally synthesized nanocrystalline MnO_2 needles anchored to the surface of graphene foam. The composite provided a maximum energy density of 8.3 Wh kg^{-1} with power density of 20 kW kg^{-1} and no capacitance loss even after 1000 cycles. This improvement in cycling stability as well as reasonable energy density was attributed to the successful coating and high loading of α- and γ -MnO_2 on a 3D porous graphene foam network that allows for the combination of double-layer and redox capacitance mechanisms. Likewise, NiO nanorods arrays have been deposited on a mesoporous 3D structure and electronically conducting Ni-foam in a review work by Yang *et al*. [113]. The microholes and crisscross flow channels on the Ni-foam substrate provided an enhanced surface area and mass transportation for electrolyte ions [114]. For this reason, a high capacitance of 2018 F g^{-1} and a corresponding 92% capacitance retention after cycling was recorded. The observed results are attributed to the ease of diffusion from the 3D structure and the reduction in diffusion distance from the slim rod morphology which optimizes the surface area for insertion and exertion of ions.

In addition, the strong chemical bonding of the rods to the substrate ensures good electron transport from the nanorods to the metallic current collector.

Similarly, over the past few decades, t-MOH nanostructures with different morphologies ranging from nanowires to nanosheets have also been adopted in supercapacitor applications due to the availability of adequate surface area useful for electrochemical surface reactions. Nanostructured $Co(OH)_2$ electrode was fabricated by a facile, low cost and efficient electrochemical technique which involved electro-deposition of $Co(OH)_2$ nano-whiskers on a pre-etched nanoporous Ni-substrate. The unique architecture provided an exceptional high energy storage electrode of specific capacitance as high as 2800 F g^{-1} with a preserved cycling stability due to the nanoporous nature of the substrate [96]. Two dimensional (2D) ultra-thin α – $Ni(OH)_2$ nanosheets have been recently synthesized by Zhu *et al*. [73] on a large scale via a microwave-assisted liquid phase growth under low temperature atmospheric conditions. The freestanding sheets demonstrated an enhanced SC performance with a specific capacitance of 4172 F g^{-1} at a 1 A g^{-1} current density and 98.5% capacitance retention value even after 2000 cycles. This method shows a promising trend for scaling up to produce high quality device electrode for commercial purposes.

Another form of metal hydroxides suitable for SC electrode material applications is the metal layered double hydroxides (LDHs). They are characterized with a mesoporous structure with thinner sheets that have higher surface area and good faradaic active properties. The thinner sheets facilitate electrolyte penetration with a corresponding increase in capacitance value and electrode cycling stability. A general chemical formula of $[M^{p+}_{1-x}M^{q+}_{x}(OH)_2]^{x+}[A^{n-}_{x/n}]^{x-}.mH_2O$ is used to describe LDH materials where M^{p+} and M^{q+} are commonly divalent and trivalent cations respectively; A^n is a charge-balancing n-

valent anion from the precursor salts used in the preparation of the active material; and $x = M^{p+}/(M^{p+}+M^{q+})$. In addition, their tunable composition and flexible ion-exchangeability also creates suitable active chemical sites present for both electric double layer capacitors and redox capacitors [115]. Their environmentally friendly growth techniques coupled with the attractive redox property makes LDHs great potential application as electrode materials for redox supercapacitors [116,117]. Common examples of metal combinations includes; NiAl-[118], NiCo-[119], and CoAl-LDHs [120]. Song *et al*. [118] reported a solvothermal technique for synthesizing NiAl LDHs with high surface area and porosity in varying ethanol/water solvent ratios. Results obtained were compared with those from common hydrothermal route and an enhanced surface area and specific capacitance were found to be superior to those prepared with H_2O alone. A growth mechanism for the nanostructures under different conditions was proposed and the superior capacitance recorded was related to the morphology of the NiAl LDH. Another similar study on the influence of morphology of LDH materials on electrochemical performance by Tao *et al.* [119] demonstrates an in-situ growth of three dimensional (3D) NiCo-double hydroxide microspheres using a tert-butanol (TBA) as a structural directing agent to obtain different architectures which directly impact on the measured capacitance. The electrode offered an excellent electrochemical performance with a superior capacitance value of 2275 F g^{-1}, high rate capability and excellent cycling life even after 5000 galvanostatic charge-discharge cycles. However, most of these metal oxides and hydroxides are still faced with the issue of a low operating voltage window and in some cases low conductivity which inhibits on

their overall energy density making them lower than EDLC materials. The issue of restacking of the sheets of LDH also restricts access of electrolytes ions to maximally use up their available surface area.

2.2.3 Hybrid Electrochemical Capacitors and Composite materials

Hybrid electrochemical capacitors (Hy-ECs) combine properties of both EDLCs and RECs. Materials for hybrid capacitors play a major role for the successful generation and efficient energy storage within the device. It is thus of vital importance to fully optimize their individual material properties in such a way as to obtain superior electroactive materials for advanced applications [121].

Composite materials provide an avenue for obtaining materials with enhanced electrochemical properties. They offer a smart alternative approach for combining materials with different properties by exploiting the merits and mitigating the shortcomings of EDLCs (non-faradaic) and pseudocapacitors (faradaic) to obtain better performance characteristics. Such characteristics include enhancing specific surface area and porosity, facilitating electron and proton conduction, preventing agglomeration of particles and optimizing particle size, expanding active sites, extending the potential window, protecting active materials from mechanical degradation and improving cycling stability. In this case, this is achieved by incorporating carbon-based materials with either pseudocapacitive conducting polymers or metal oxide materials to synergize both physical and chemical charge storage mechanisms. The process basically involves the

actual combination of both active materials to form a mixture (composites) or by combining individual material electrodes (in the case of “hybrid ECs”).

Even so, it is worth stating that a reverse effect might occur during this combination process. Thus, there should be a consensus with regards to the individual material compositions and an optimized charge balance/molar ratio (in the case of composites and hybrid devices respectively) of the individual constituent in order to achieve a good composite.

Gao *et al*.[122] demonstrated the production of graphene nanosheet-layered double hydroxide (GNS/LDH) by a simple hydrothermal technique. In their report, glucose was used as a reducing agent in place of toxic hydrazine to exfoliate graphene oxide (GO) sheets and obtain an even dispersion of GNS in water. The observed remarkable specific capacitance was ascribed to be due to the combination of the EDLC and faradaic capacitance from the open structure system with improved contact between the electrode/electrolyte interface [122]. The conductive network of graphene sheets over-lapping each other was explained to facilitate fast electron transfer between the active composite material and the charge collector. Another report by Dong *et al.*[61] adopted an innovative strategy of growing cobalt oxide (Co_3O_4) nanowires on 3D graphene foam by an in situ deposition method. The graphene/Co_3O_4 composite was used as a monolithic free-standing supercapacitor electrode and exhibited a good specific capacitance of ~1100 F g^{-1} at a current density of 10 A g^{-1} with excellent cycling stability after 1000 cycles. The electrochemical properties of poly(3,4-ethylenedioxythiophene) /multi-walled carbon nanotubes (PEDOT/MWCNTs) composites have also been

investigated by Lota *et al*.[86]. The composite was prepared by electrochemical polymerization of EDOT directly on the nanotube. The specific capacitance values for the composite ranges between 60 – 160 F g^{-1} with a good cycling performance in different electrolytes. These excellent electrochemical properties and efficient reversible storage was attributed to the open mesoporous CNT-network coupled with the easily accessible electrode/electrolyte interface which allows quick charge propagation within the composite material [86].

2.3 Electrolytes

The electrolyte is also a very important component of the electrochemical capacitor system. It contains ions necessary for charge transport and storage. The requirements for an electrolyte include wide voltage window, high electrochemical stability, high ionic concentration, low solvated ionic radius, little cost, low toxicity and resistivity,.

Electrolytes can generally be divided into three (3) main categories namely;

(i) Aqueous electrolytes

(ii) Organic electrolytes

(iii) Ionic liquids

(I) Aqueous electrolytes (AEs)

AEs are mainly composed of strong acids, bases or salts of strong acids dissolved in water and have high conductivity due to their proton hopping transport mechanism and high ionic activity. However, the operating voltage of these electrolytes are limited to a theoretical value of 1.23 V [39,123]. The most common aqueous electrolytes used for EC applications include H_2SO_4 [124], Na_2SO_4 [125], KOH [126], NH_4Cl [127] etc. The capacitance of ECs containing aqueous electrolytes may generally be higher than those with organic electrolytes due to the high ionic concentration and smaller ionic radius [8]. Furthermore, the preparation procedure and use of aqueous electrolytes is somewhat easy and less complicated as compared to organic electrolytes which need stringent conditions in order to obtain and maintain ultra-pure stable electrolytes. However, aqueous electrolytes have limited voltage operating window of only 1.2 V due to the decomposition at high voltages. Thus, they limit the enhancement of the energy and power densities when used for SC applications.

(II) Organic electrolytes (OEs)

Organic electrolytes are capable of providing a higher operating potential window (of approx. 3.5V) compared to aqueous electrolytes. This is why they are commonly used for commercial supercapacitors. Examples of organic electrolytes used in SCs include acetonitrile (AN) [128], propylene carbonate (PC) [129], tetraethylammonium tetrafluoroborate [28], triethylmethylammonium tetrafluoroborate (TEMABF4) [130] etc. Acetonitrile can dissolve large other organic electrolytes and can thus provide highly conductive electrolytes [131]. However, they are plagued with environmental instability

and toxicity problems which make their use restricted to controlled environments in order to prevent poisoning or explosion. The water content in organic electrolytes should also be kept to a minimum (normally below 3 – 5 ppm) for them to retain their characteristic large operating voltage window. Propylene carbonate-based electrolytes are less toxic and can be used as replacements for AN electrolyte to provide an equally large potential window but their low conductivity leads to decreased power density.

(III) Ionic liquids (ILs)

Ionic liquids are solvent-free liquids which are molten at room temperature. They are obtained by overcoming the material lattice energy to melt or liquefy them to liquid form. They are mainly made up of cations and anions which make their voltage window stability mainly dependent on the electrochemical stability of the constituent ions. A careful and proper choice of both ions allows them to be used in the design of high-voltage window ECs. The characteristic properties which makes them ideal for SCs include good conductivity [132], low vapor pressure, high thermal and electrochemical stability [133], low flammability, wide voltage window of averagely 4.5 V. ILs can offer a unique ion size due to the absence of any solvent or associated solvation shells. Examples of ILs include imidazolium, pyrrolidinium, aliphatic ammonium salts with anions such as tetrafluoroborate, trifluoromethanesulfonate, bis(fluorosulfonyl)imide or hexafluorophosphate, quaternary ammonium salts such as tetralkylammonium [R4N]+, and cyclic amines such as aromatic pyridinium, imidazolium and saturated piperidinium, pyrrolidinium [132,134]. Reports on ECs devices based on ILs relating the relationship between the pore size of carbon electrodes, ion size of the electrolyte, and the

capacitance using ethyl-methyl-imidazolium-bis(trifluoromethane-sulfonyl)imide have been studied in reference [17]. An improved performance is also seen in hybrid activated carbon/conducting polymer devices with characteristic cell voltages greater than 3 V [135]. However, the ionic conductivity of these liquids is low at room temperature, and could be improved by selecting appropriate eutectic ionic liquid mixture-carbon combinations [136]. In addition, the dilution of ILs with organic electrolytes (such as acetonitrile, propylene carbonate or g-butyrolactone) might also be a good choice. For example, ILs mixed with the commonly used PC/TEMABF4 electrolytes showed some improvement in conductivity and therefore higher capacity and enhanced low-temperature power density [8]. However, this approach might lead to the resurfacing of other problems associated with organic electrolytes such as safety, toxicity, flammability etc.

2.4 Advantages, application and challenges arising from the use of ECs

Electrochemical capacitors are particularly looked upon as replacements for conventional capacitors and possibly batteries in the long run due to their attractive and desirable properties which include the following:

(i) <u>High power density</u>

ECs are known to exhibit a much higher power density than their battery counterparts [5]. This is also confirmed in the Ragone plot shown in figure 2.1 where the range of power density values for SCs are within the range of 1 – 100 KW kg^{-1} and that for batteries is in the range of 40 – 150 W kg^{-1}. The charge-discharge rate for SCs are not

limited by ionic conductivity in the bulk due to the fact that they store electrical charges both at the electrode surface and in the bulk near the solid electrode surface as compared to batteries which only store charge by redox reactions contained in their bulk. For example, in batteries, the charging time is normally on a scale of hours depending on the application whereas a typical SC could be fully charged or discharged in tens of seconds (~ 30 seconds) and the energy can be taken from it rapidly within a tenth of a second (~ 0.1 second) [137].

(ii) High efficiency

ECs are reversible with respect to charging and discharging throughout their operating voltage window and the loss of energy due to heat in each cycle is managed by easy removal due to its relatively small amount. Thus, the cycle efficiency of ECs are high (around 95%) even when operating at high power rates [8].

(iii) Long life expectancy

Faradaic reactions are the route through which batteries store energy in their material bulk. These processes are characterized with irreversible inter-conversion of the chemical electrode reagents and irreversible phase change. On the other hand, electrochemical storage in SCs involve negligibly small chemical charge transfer reactions and phase changes during charging and discharging, thus giving them an almost unlimited cyclability. The life expectancy for batteries is only about 5 – 10 years with 1000 – 10000 charge - discharge cycles; whereas, it is estimated to be up to about 30 years for SCs with little or no maintenance during their lifetime [8]. Moreover, SCs can run deep cycles at high rates for up to 500,000 cycles with only a small change in

their properties. This is impossible for batteries even if they have a small depth of discharge.

(iv) Long shelf life

ECs maintain their capacitance even if left unused for several years [16] although they self-discharge over a period of time leading to lower operating voltages. However, batteries if left on the shelf without use will self-degrade due to self-discharge and corrosion of the constituent materials.

(v) Wide range of operating temperature

The typical range of operating temperatures of ECs is between – 40 °C to 70 °C. This makes them suitable for a wide range of applications such as military operations where an efficient and reliable back up energy supply is needed to run electronic devices properly under all temperature conditions.

(vi) Safety and environmental friendliness

ECs are generally much safer to use and contain little or no toxic and hazardous materials as compared to batteries (especially Li-ion batteries) [8].

The numerous advantages and prospects discussed so far have made ECs a competitive and exciting device choice in technological applications like the electric trains, electric hybrid vehicles, personal gadgets (such as mobile phones, cameras, tablets, etc), electrical tools, uninterruptible power supplies and as storage units harnessed to solar cells to capture the generated solar energy [138–141]. A report by Miller *et al.* presents

a clear summary distinguishing the application of ECs into three main groups viz; energy management applications, power tools applications and day-night storage applications.

It is worthy to note that SCs in their present state cannot replace batteries. However, only a combination of the SCs with batteries is feasible as ECs are still characterized with low energy densities. As such, combining them will maximize the merits of both systems and provide a suitable hybrid system to fit in present day application requirements. For example, in hybrid vehicles, SCs are used in combination with the batteries for the initial acceleration, braking energy recovery, excellent cold weather starting etc. and this increases the overall battery life [8,141]. Thus ECs have the potential in complementing batteries in the energy conversion and storage fields [17] with a possible complete replacement achievable over time based on the active on-going research and development in the supercapacitor research world.

Due to their relatively low energy density and high manufacture cost, the market for ECs is still in a premature commercialization stage. Analyst stick to a forecast of 30 % compound growth of this market over the coming decades. The total global market for supercapacitors was worth $470 million in 2010, according to reports titled; “Supercapacitors: Technology Developments and Global Markets”. That value is projected to grow to $1.2 billion by the end of this year, a five-year compound annual growth rate (CAGR) of 20.6% and a $6 billion market worth by the end of 2024 [142].

2.5 Fabrication of electrodes for electrochemical capacitors

The electrode material is the core of the supercapacitor device which determines the electrochemical performance in terms of capacitance, self-discharge, life expectancy, resistance etc. Thus, the efficient fabrication of the electrode is essential and the processes involved need to be done meticulously in order to obtain high performance and durable electrodes. A highly conductive current collector should be used as template where the active material will be coated onto for testing. The current collector should also have a high current carrying capacity, chemical stability and low cost. Initially, the active material is made into a slurry/paste by mixing it with a binder and compatible conductive additive (i.e. carbon black). The slurry is then applied onto the current collector or made free-standing using a compression molding press which cuts out thin discs or pellets. The electrode thickness is usually a few tens of micrometers to sub-millimeters depending on the active material used and the proposed application. The mass of active material under analysis must be known and preferably its corresponding volume if possible. The as-obtained electrode is referred to as the "working electrode". In the case of a scientific and research study, the electrodes are usually placed in parallel with the separator and the suitable electrolyte is added to complete the set-up for electrode characterization/testing. Further packaging steps may be carried out for full cells which are meant for commercial purposes.

2.6 Electrochemical testing of the electrode material

Electrochemical testing can be done in either a two (2) electrode system or a three (3) electrode configuration. For research and development purposes, the performance of a single electrode are initially investigated using the conventional three (3) electrode configuration as shown in figure 2.10 which comprises of the active working electrode (WE), counter electrode (CE), reference electrode (RE) and a suitable electrolyte compatible with the set of electrodes. The reference electrode acts as a set-point electrode which measures and regulates the potential of the working electrode without allowing any current through it. The counter electrode on the contrary, allows the required amount of current to balance the current generated at the working electrode by varying its potential within the electrolyte. Suitable materials for CE are conductive materials which do not react with the electrolyte in which they are placed. Thus, the choice of electrolytes is highly related to the corresponding CEs and REs. For example, in acidic electrolytes, the counter electrode can be platinum or glassy carbon and the reference electrode could be a saturated calomel electrode (SCE) or a silver/silver chloride electrolyte (Ag/AgCl). In neutral electrolytes, the same configuration can be used. In alkaline aqueous electrolytes, a silver/silver chloride electrolyte (Ag/AgCl) or a mercury/mercury oxide (Hg/HgO) is used as reference electrode while for non-aqueous electrolytes, the choice of reference electrode depends on the electrolyte to be studied [143,144].

The three (3) electrode test configuration is firstly used in order to obtain the individual electrochemical properties of each electrode material without the influence of other

interaction factors that might arise when they are combined. The electrode is referred to as a "half-cell" in this configuration and a "full cell" in the two (2) electrode set-up. Specific electrode properties under study include the stable operating voltage window of the active material, specific capacitance, electrode cycling stability and the equivalent series resistance of the single electrode.

The full cell capacitance measured in a 2-electrode configuration is theoretically a quarter of the single electrode capacitance recorded in a 3-electrode system [145]. The factor of $^1/_4$ adjusts the full cell capacitance and the combined mass of the two electrodes to the half-cell capacitance and single electrode mass [4].

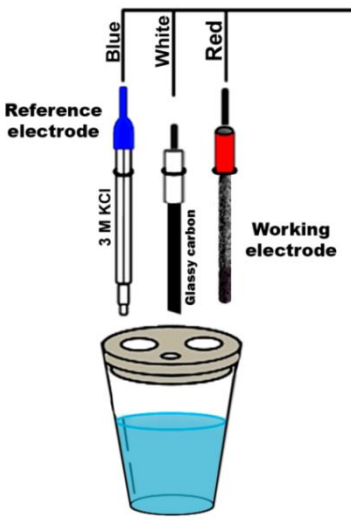

Figure 2.10: Schematic showing the set-up for testing material electrodes in a 3 - electrode configuration

In a two (2) electrode configuration (as shown in Figure 2.11), two working electrodes contained in an electrolyte are set up on opposite sides of the separator as described in the design of a simple electrochemical capacitor. In this system, the potential difference of both electrodes are monitored and additional electrochemical properties like the energy density, power density and life cycle testing can be studied [146,147].

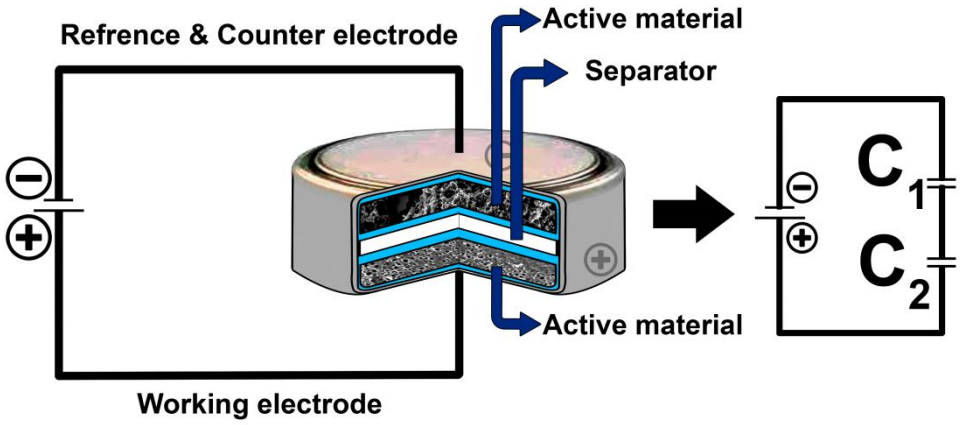

Figure 2.11: Schematic showing the set-up for testing electrode material in a 2 - electrode configuration

In summary, even if the specific capacitance of a 2-electrode cell is obtained by using the mass of one of the electrodes, the specific capacitance is not the same value as that recorded in a 3-electrode configuration with a single electrode. Possible factors have been explained to be responsible for this variance such as the difference in solvated cation and anion size, and the difference in potential at both electrodes during galvanostatic charge/discharge process.

2.7 Evaluation of electrode material

The electrochemical performance of an electrode material is basically evaluated using the cyclic voltammetry (CV), galvanostatic chronopotentiometry (GCP) and electrochemical impedance spectroscopy (EIS) techniques.

2.7.1 Cyclic Voltammetry (CV)

Cyclic voltammetry tests are carried out on electrode materials which has been either successfully coated onto the current collector substrate or tested as a free-standing electrode (pellets). The process involves applying a voltage which scans between two limits (E_1, E_2) at a scan rate, υ (mV s^{-1}) and measuring the corresponding current. The plot of current versus voltage generated is usually referred to as a "cyclic voltammogram". The area under the plot in either direction in a potential window is referred to as the charge Q, accumulated inside the electrode. The capacitance of the electrode material is given as [8]:

$$C_i = \left|\frac{Q}{E_2 - E_1}\right| \tag{13}$$

where Q is the charge stored, ($E_2 - E_1$) is the potential window set points.

The entire process has a mole fraction expressed as $\chi = QM/mF$ in which M is the molecular weight, F is the Faraday constant, and m is the mass of the electrode.

A typical CV curve for a pseudocapacitive material is shown in figure 2.11 where the different parts of the voltammogram are labeled. The electrochemical reaction depicted by this CV curve is a reversible redox process [148]. At higher scan rates, larger peaks are observed due to the collection of only the highest intensity part of the storage transient. With lower scan rates, full storage is not achieved due to kinetic limitations associated with the diffusion of material being investigated.

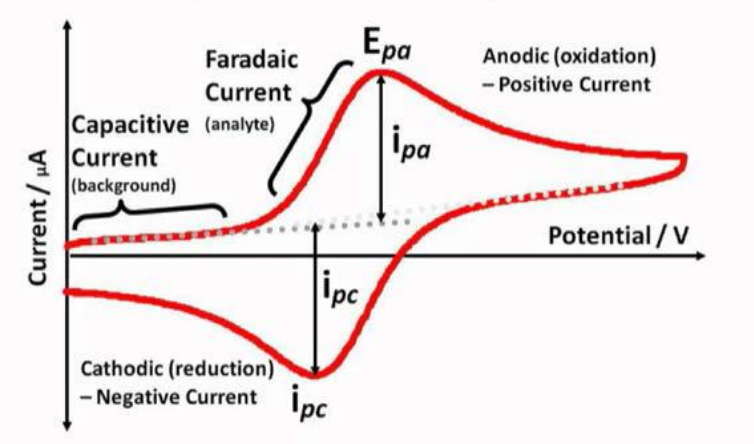

Figure 2.12: Cyclic voltammetry plot of a typical pseudocapacitor. (Extracted from ref.[4])

The mole fraction of inserted material reaches a value of approx. 0.5 when the lattice of positive ions is fully impregnated and this corresponds to a specific charge capacity. The total charge stored can be separated into three (3) components namely;

(i) The faradaic contribution from ion insertion.

(ii) The faradaic contribution from the charge transfer process with surface atoms (also known as Pseudocapacitance) and;

(iii) The non-faradaic contribution from the EDL effect.

The components (ii) and (iii) cannot be distinctly separated and are usually characterized by analyzing the CV data at various scan rates (*f*) according to the equation [149]:

$$I = a\, v^{b} \tag{14}$$

where *I* is the current, *υ* is the scan rate; a & b are adjustable parameters with b determined from the slope of the plot of log (*I*) vs log (*υ*)**.**

For a reversible electrochemical process, the CV plots must have:

(a) the peak voltage difference between the anodic and cathodic current peaks as small as possible (usually ~ 59 mV n^{-1}) where n is the number of electrons

(b) the positions of peak voltage do not change as a function of scan rate

(c) the ratio of the peak currents is Unity

(d) the peak current is proportional to the square root of the scan rate i.e. from the power law equation; $I = \upsilon^{0.5}$

The cyclic voltammogram for the EDLC-type electrodes are rectangular and the capacitance can be estimated using the equation relating capacitance C and the current (I) and scan rate (υ) given as [150]:

$$C = \frac{I}{\upsilon}: \tag{15}$$

Another expression for calculating gravimetric capacitance using the CV plot is given as [151]:

$$C_s\ \left(\frac{\mathrm{F}}{\mathrm{g}}\right) = \frac{\bar{A}}{\upsilon m \Delta V} \tag{16}$$

where $\bar{A}$ is the integral area of the CV curve (in mA-V); m is the mass of the active material (in g); and υ is the scan rate (in mV s^{-1}) used during the CV measurement. When a faradaic-type material is studied, the potential for capacitance calculation must be carefully chosen in the region where the material is stable as the CV plots are characterized with oxidation and reduction peaks as shown in figure 2.12.

Generally, the capacitance decreases as the scan rate increases due to less complete interactions between ions and the electrode's active surface area. The movement of ions are limited by diffusion at higher scan rates and only the outer active surfaces are used for charge storage [150]. As such there should be a minimum value of the scan rate, υ for which an enhanced high capacitance performance can be obtained. Application of a high potential may be a possible source of degradation during CV analysis.

In order to electrochemically describe a supercapacitor electrode, certain parameters need to be obtained. The capacitance of an EDLC can be calculated using:

$$I = C\ \times \frac{dV}{dt} \tag{17}$$

where I is the current, $(\frac{dV}{dt})$ is the potential scan rate and C is the double layer capacitance. The specific capacitance can be described as the capacitance in terms of mass (m), area (A) or volume (v).

The energy stored in a capacitor is directly related to the capacitance and the energy density of the electrode material is obtained from the specific capacitance of the electrode and the operating voltage as:

$$E_D = \frac{1}{8} C_{sp} V^2 \quad (18)$$

The maximum energy density on the other hand expressed in (Wh Kg^{-1}) is given as:

$$E_{MAX} = \frac{1}{2\times3600} C V^2 \quad (19)$$

where C is the capacitance of the cell in farads, C_{sp} is the specific capacitance in Farads (per Kg, area or volume depending on the normalization reference), V is the voltage (in volts),

The power is the energy expended per unit time and since the capacitor usually consists of the current collector, electrode and dielectric material, there will be an associated equivalent series resistance (ESR).from these extra components. As such; the associated maximum power density the cell can deliver is expressed as:

$$P_{MAX} = \frac{1}{4\times(ESR)} \frac{V^2}{M} \quad (20)$$

where ESR is the equivalent series resistance and M is the total mass of active material. Equation (20) clearly shows the dependence of maximum power of the capacitor on the ESR; thus it is ideal to ensure that this value remains as small as possible for high power density.

The capacitance depends on the electrode material used and the stability of the operating voltage in the working electrolyte. The maximum operating voltage is mainly limited to the level at which decomposition of the solvent in the electrolyte takes place (in the case of aqueous electrolytes). The energy density and power density of the capacitor both depend on the operating voltage as seen from equations (18-20); therefore the use of highly capacitive material with a large potential window is also important in obtaining improved energy densities comparable to those of batteries.

2.7.2 Chronopotentiometry (CP) or Galvanostatic Charge/Discharge (GCD)

Chronopotentiometry tests are carried out by applying a controlled current pulse (*I*) between the working and auxiliary electrodes and the corresponding generated voltage (*V*) is measured as a function of time [152]. This is the opposite case to the cyclic voltammetry tests in section 2.7.1 where the voltage was controlled. At the instance when the current is initially applied, there is an abrupt change in the measured potential due to the utilization of reactants and IR-loss at the electrode surface where storage processes are taking place. Over time, the ratio of the concentration of reactant to

products continues changing with time until the amount of reactants is completely depleted. [152].

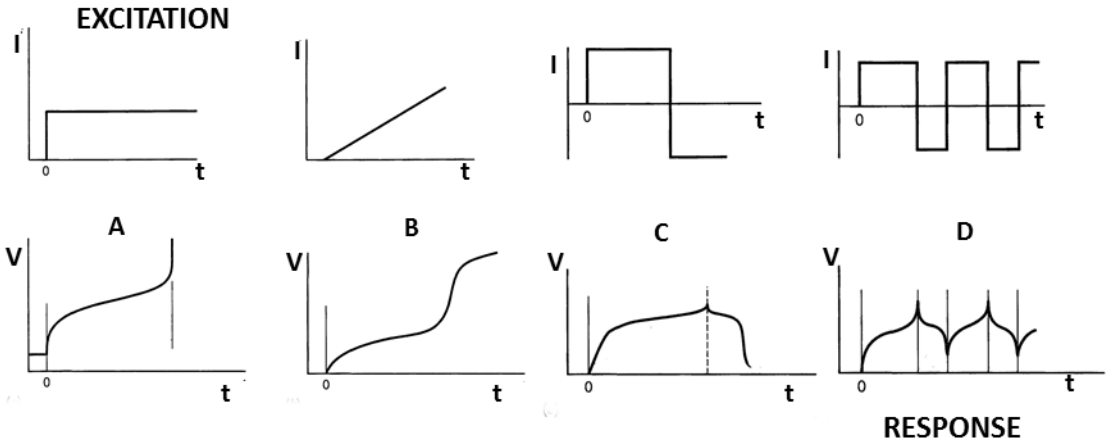

Figure 2.13: Different types of controlled-current chronopotentiometry techniques. (A) CC-CP, (B) LRC-CP, (C) CR-CP, (D) CyC-CP. (Image extracted from ref.[152]).

At this point, there is limited or no reactants for the available flux of electrons at the electrode surface and the electrode potential abruptly changes towards more negative values until it is appropriate for the opposite reaction to occur to replenish the reactants. The time interval between the initial application of current to the transition of the electrode potential is termed “transition time, τ”. There are different types of chronopotentiometric techniques based on the type of current applied and the associated voltage versus time (*V-t*) curve generated.

The shape and location of the *V-t* curve is governed by the reversibility of the electrode reaction. These include the constant-current chronopotentiometry (CC-CP), linearly-rising current chronopotentiometry (LRC-CP), current reversal chronopotentiometry (CR-CP) and cyclic current chronopotentiometry (CyC-CP).

As the name implies, the CC-CP involves application of a fixed anodic/cathodic current to the electrode which causes the electroactive species to be oxidized/reduced respectively at a constant rate (Figure 2.13-A). The applied current could also be constantly ramped up in a linear pattern over time (i.e. $I = \alpha t$) or reversed after a particular time as shown in figure 2.13-B & C. In the case of the CR-CP, a sudden change from the cathodic to anodic current of equal magnitude before or at the transition time, τ, will initiate the generation of more reactants. When the product initially formed in the previous reaction becomes diminished at the electrode surface, a potential transition occurs and the reverse transition time can be obtained. An addition to this technique is the continuous reversal at each transition time which gives the CyC-CP method (Figure 2.13-D).

The capacitance of an electrode material is best determined from the galvanostatic or constant current discharge curve [145]. It is the established measurement method for determining capacitance of packaged supercapacitors in the ultracapacitor industry and correlates more closely to how a load is applied to a supercapacitor in major applications. When the capacitance of material shows EDL behavior, the potential (V) of the chronopotentiogram varies linearly with time t, at a constant current.

Then the capacitance is related to the slope of linear potential-time relationship dV/dt, with the current (I) as [151]:

$$C = I/(dV/dt). \quad (21)$$

Similar to the case of the cyclic voltammogram discussed earlier, when there is a redox capacitance contribution to the total capacitance, the chronopotentiogram deviates from the linear relationship to a non-linear behavior. Such that the capacitance is usually given by, $C = I \times \Delta T/\Delta V$, where ΔT is the total discharge time for the electrode material obtained from the CP plot and ΔV is a potential difference after correcting an IR drop (voltage drop) which is estimated from the initial potential jump of chronopotentiogram.

2.7.3 Electrochemical Impedance Spectroscopy (EIS)

Electrochemical impedance spectroscopy (EIS) is also a useful way in determining the capacitance of electrode materials for SCs [7]. EIS measurements are run by applying small amplitude of alternating interrupting potential (in mV) over a range of frequencies (mHz to MHz) and collecting the impedance data at preferably an open circuit voltage. Information relating to the imaginary part of impedance (Z”) and the frequency (f) can

be obtained from this process. Some important plots gotten from the EIS measurements include the Bode plot and the Nyquist plot.

The Bode plot relates the $log\ |Z"|$ to $log\ |f|$ where *Z"* and *f* have their usual meanings mentioned earlier. The capacitance (C) can be calculated from the linear portion of the Bode plot using the relation [8]:

$$C = \frac{1}{2\pi f|Z"|} \tag{22}$$

The Nyquist plot relates the imaginary part of impedance Z(*f*)" with the real part of impedance Z(*f*)' [143] and can be used to obtain additional electrode material properties such as the charge transfer resistance, (R_{CT}), solution/electrolyte resistance, (R_{Ω}) etc. The diameter of the semicircle of the Nyquist plot shown in figure 2.14 gives the R_{CT} value. At high frequencies (> 10^4 Hz), the intercept of the impedance plot on the real $|Z|$ axis gives information on the conductivity of the electrolyte.

The pseudocharge transfer resistance linked to the porosity of the electrode material can be obtained from the medium frequency region (10 Hz - 1 Hz). At the low frequency region, (< 1 Hz), the impedance plot depicts the characteristic property of a pure capacitive behavior. The pure capacitor should ideally exhibit a straight line parallel to the imaginary $|Z|$ axis on the Nyquist plot, but this is not usually the case.

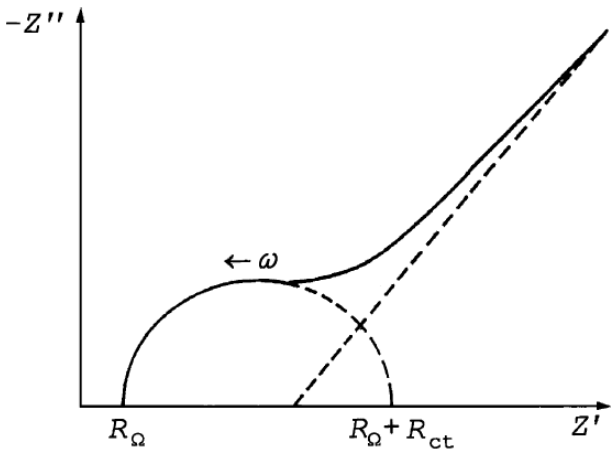

Figure 2.14: Nyquist impedance plot

A tilted line with angle of $45° \leq \theta \leq 90^o$ with respect to the real axis is obtained and this has been explained to correspond to ion diffusion mechanism between the Warburg diffusion and ideal capacitive ion diffusion (pseudocapacitance) [153,154].

This nonconformity with the ideal situation is linked to the redox reaction and variance in penetration depth of the alternating current signal in relation to the pore size distribution at the electrode leading to abnormal capacitance [155,156].

2.8 References

[1] B.E. Conway, J. Electrochem. Soc. 138 (1991) 1539.

[2] R. Kotz, M. Carlen, Electrochim. Acta 45 (2000) 2483.

[3] F. Benguin, E. Frackowiak, Carbon 39 (2001) 937.

[4] Bello Abdulhakeem, Three Dimensional Graphene Composites for Energy Storage Applications, Thesis (PhD), University of Pretoria, 2014.

[5] S. Holmberg, A. Perebikovsky, L. Kulinsky, M. Madou, Micromachines 5 (2014) 171.

[6] M. Winter, R.J. Brodd, Chem. Rev. 104 (2004) 4245.

[7] Y.M. Vol'fkovich, T.M. Serdyuk, Russ. J. Electrochem. 38 (2002) 935.

[8] G. Wang, L. Zhang, J. Zhang, Chem. Soc. Rev. 41 (2012) 797.

[9] B. Conway, Electrochemical Supercapacitors: Scientific Fundamentals and Technological Applications, Kluwer Academic Publishers, Plenum Press: New York, New York, 1999.

[10] M. Halper, J. Ellenbogen, MITRE Corp. McLean (2006) 1.

[11] A. Burke, J. Power Sources 91 (2000) 37.

[12] J.P. Zheng; J. Huang and T.R. Jow, J. Electrochem. Soc. 144 (1997) 2026.

[13] M. Endo, T. Maeda, T. Takeda, Y.J. Kim, K. Koshiba, H. Hara, M.S. Dresselhaus, J. Electrochem. Soc. 148 (2001) A910.

[14] D. Qu, H. Shi, J. Power Sources (1998).

[15] O. Barbieri, M. Hahn, A. Herzog, R. Kötz, Carbon N. Y. 43 (2005) 1303.

[16] P. Simon, Y. Gogotsi, Nat. Mater. 7 (2008) 845.

[17] C. Largeot, C. Portet, J. Chmiola, P.-L. Taberna, Y. Gogotsi, P. Simon, J. Am. Chem. Soc. 130 (2008) 2730.

[18] M.C.F. Wander, K.L. Shuford, J. Phys. Chem. C 114 (2010) 20539.

[19] H. Helmholtz, Ann. Phys 89 (1853) 21.

[20] M. Gouy, J. Phys. Théorique Appliquée 9 (1910) 457.

[21] D.L. Chapman, E. London, Mag. J. Sci. 25 (1913) 475.

[22] H. Stern-Hamburg, S.F Electrochem. (1924) 508.

[23] M. Vorotyntsev, Modern Aspects of Electrochemistry, Plenum, New York:, 1986.

[24] F. Béguin, V. Presser, A. Balducci, E. Frackowiak, Adv. Mater. 26 (2014) 2219.

[25] H. Nishihara, T. Kyotani, Adv. Mater. 24 (2012) 4466.

[26] A. Bello, F. Barzegar, D. Momodu, J. Dangbegnon, F. Taghizadeh, N. Manyala, Electrochim. Acta 151 (2015) 386.

[27] M. Zhi, F. Yang, F. Meng, M. Li, A. Manivannan, N. Wu, ACS Sustain. Chem. Eng. 2 (2014) 1592−1598.

[28] E. Raymundo-Piñero, K. Kierzek, J. Machnikowski, F. Béguin, Carbon N. Y. 44 (2006) 2498.

[29] F. Zhao, A. Vicenzo, M. Hashempour, M. Bestetti, Electrochim. Acta (2014).

[30] L.L. Zhang, X.S. Zhao, Chem. Soc. Rev. 38 (2009) 2520.

[31] A. Bello, M. Fabiane, D.Y. Momodu, S. Khamlich, J.K. Dangbegnon, N. Manyala, J. Solid State Electrochem. 18 (2014) 2359.

[32] B. Xu, F. Wu, R. Chen, G. Cao, S. Chen, Z. Zhou, Y. Yang, Electrochem. Commun. 10 (2008) 795.

[33] C. Portet, Z. Yang, Y. Korenblit, Y. Gogotsi, R. Mokaya, G. Yushin, J. Electrochem. Soc. 156 (2009) A1.

[34] D. Pech, M. Brunet, H. Durou, P. Huang, V. Mochalin, Y. Gogotsi, P.-L. Taberna, P. Simon, Nat. Nanotechnol. 5 (2010) 651.

[35] K. Makgopa, P.M. Ejikeme, C.J. Jafta, K. Raju, M. Zeiger, V. Presser, K.I. Ozoemena, J. Mater. Chem. A 3 (2015) 3480.

[36] S.G. Herawan, M.S. Hadi, M.R. Ayob, a. Putra, Sci. World J. 2013 (2013).

[37] H. Shi, Electrochim. Acta 41 (1996) 1633.

[38] K. Kierzek, E. Frackowiak, G. Lota, G. Gryglewicz, J. Machnikowski, Electrochim. Acta 49 (2004) 515.

[39] A.G. Pandolfo, A.F. Hollenkamp, J. Power Sources 157 (2006) 11.

[40] H. Pan, J. Li, Y. Feng, Nanoscale Res. Lett. 5 (2010) 654.

[41] K.S. Novoselov, A.K. Geim, S. V Morozov, D. Jiang, Y. Zhang, S. V Dubonos, I. V Grigorieva, A.A. Firsov, Science 306 (2004) 666.

[42] A.K. Geim, G. Opportunities, Science 324 (2009) 1530.

[43] X. Wang, L. Zhi, K. Müllen, Nano Lett. 8 (2008) 323.

[44] T. Yumura, K. Kimura, H. Kobayashi, R. Tanaka, N. Okumura, T. Yamabe, Phys. Chem. Chem. Phys. 11 (2009) 8275.

[45] K.S. Novoselov, A.K. Geim, S. V Morozov, D. Jiang, M.I. Katsnelson, I. V Grigorieva, S. V Dubonos, A.A. Firsov, Nature 438 (2005) 197.

[46] S.R.C. Vivekchand, C.S. Rout, K.S. Subrahmanyam, a. Govindaraj, C.N.R. Rao, J. Chem. Sci. 120 (2008) 9.

[47] Y. Wang, Z. Shi, Y. Huang, Y. Ma, C. Wang, M. Chen, Y. Chen, J. Phys. Chem. C 113 (2009) 13103.

[48] Y. Zhu, S. Murali, W. Cai, X. Li, J.W. Suk, J.R. Potts, R.S. Ruoff, Adv. Mater. 22 (2010) 3906.

[49] A.K. Geim, K.S. Novoselov, Nat. Mater. 6 (2007) 183.

[50] H. Wang, H.S. Casalongue, Y. Liang, H. Dai, J. Am. Chem. Soc. 132 (2010) 7472.

[51] K. Zhang, L.L. Zhang, X.S. Zhao, J. Wu, Chem. Mater. 22 (2010) 1392.

[52] L.L. Zhang, S. Zhao, X.N. Tian, X.S. Zhao, Langmuir 26 (2010) 17624.

[53] L.L. Zhang, T. Wei, W. Wang, X.S. Zhao, Microporous Mesoporous Mater. 123 (2009) 260.

[54] Z.-S. Wu, D.-W. Wang, W. Ren, J. Zhao, G. Zhou, F. Li, H.-M. Cheng, Adv. Funct. Mater. 20 (2010) 3595.

[55] Q. Wu, Y. Xu, Z. Yao, A. Liu, G. Shi, ACS Nano 4 (2010) 1963.

[56] B. Wang, J. Park, C. Wang, H. Ahn, G. Wang, Electrochim. Acta 55 (2010) 6812.

[57] Z.-S. Wu, G. Zhou, L.-C. Yin, W. Ren, F. Li, H.-M. Cheng, Nano Energy 1 (2012) 107.

[58] M. Li, J.E. Zhu, L. Zhang, X. Chen, H. Zhang, F. Zhang, S. Xu, D.G. Evans, Nanoscale 3 (2011) 4240.

[59] Z. Chen, W. Ren, L. Gao, B. Liu, S. Pei, H.-M. Cheng, Nat. Mater. 10 (2011) 424.

[60] X. Cao, Y. Shi, W. Shi, G. Lu, X. Huang, Q. Yan, Q. Zhang, H. Zhang, Small 7 (2011) 3163.

[61] X.-C. Dong, H. Xu, X.-W. Wang, Y.-X. Huang, M.B. Chan-Park, H. Zhang, L.-H. Wang, W. Huang, P. Chen, ACS Nano 6 (2012) 3206.

[62] U.M. Patil, J.S. Sohn, S.B. Kulkarni, S.C. Lee, H.G. Park, K. V Gurav, J.H. Kim, S.C. Jun, ACS Appl. Mater. Interfaces 6 (2014) 2450.

[63] E. Herrero, L.J. Buller, H.D. Abruña, Chem. Rev. 101 (2001) 1897.

[64] V. Augustyn, P. Simon, B. Dunn, Energy Environ. Sci. 7 (2014) 1597.

[65] P. V. Braun, J. Cho, J.H. Pikul, W.P. King, H. Zhang, Curr. Opin. Solid State Mater. Sci. 16 (2012) 186.

[66] S. Trasatti, G. Buzzanca, J. Electroanal. Chem. Interfacial Electrochem. 29 (1971) A1.

[67] T. Brousse, M. Toupin, R. Dugas, L. Athouël, O. Crosnier, D. Bélanger, J. Electrochem. Soc. 153 (2006) A2171.

[68] V. Augustyn, J. Come, M. a Lowe, J.W. Kim, P.-L. Taberna, S.H. Tolbert, H.D. Abruña, P. Simon, B. Dunn, Nat. Mater. 12 (2013) 518.

[69] M. Okubo, E. Hosono, J. Kim, M. Enomoto, N. Kojima, T. Kudo, H. Zhou, I. Honma, J. Am. Chem. Soc. 129 (2007) 7444.

[70] C.-C. Hu, K.-H. Chang, M.-C. Lin, Y.-T. Wu, Nano Lett. 6 (2006) 2690.

[71] H. Zhang, G. Cao, Z. Wang, Y. Yang, Z. Shi, Z. Gu, Nano Lett. 8 (2008) 2664.

[72] H.B. Li, M.H. Yu, F.X. Wang, P. Liu, Y. Liang, J. Xiao, C.X. Wang, Y.X. Tong, G.W. Yang, Nat. Commun. 4 (2013) 1894.

[73] Y. Zhu, C. Cao, S. Tao, W. Chu, Z. Wu, Y. Li, Sci. Rep. 4 (2014) 5787.

[74] T. Yan, R. Li, Z. Li, Mater. Res. Bull. 51 (2014) 97.

[75] R.S.L. Liu, T.-C., Pell W.G., Conway B.E., J. Electrochem. Soc. 145 (1998) 1882.

[76] D. Choi, G.E. Blomgren, P.N. Kumta, Adv. Mater. 18 (2006) 1178.

[77] T.A. Centeno, F. Stoeckli, Electrochim. Acta 52 (2006) 560.

[78] W. Li, D. Chen, Z. Li, Y. Shi, Y. Wan, G. Wang, Z. Jiang, D. Zhao, Carbon N. Y. 45 (2007) 1757.

[79] J.P. Zheng, P.J.. Cygan, T.R. Jow, J. Electrochem. Soc. 142 (1995) 2699.

[80] C. Arbizzani, M. Mastragostino, F. Soavi, J. Power Sources (2001).

[81] K.S. Ryu, K.M. Kim, N.-G. Park, Y.J. Park, S.H. Chang, J. Power Sources 103 (2002) 305.

[82] C. Arbizzani, M. Mastragostino, L. Meneghello, Electrochim. Acta 41 (1996) 21.

[83] Clemente, A;Panero, S;Spila, E;Scrosati, B., Solid State Ionics 85 (1996) 273.

[84] W. Li, J. Chen, J. Zhao, J. Zhang, J. Zhu, Mater. Lett. 59 (2005) 800.

[85] P. Pieta, I. Obraztsov, F. D'Souza, W. Kutner, ECS J. Solid State Sci. Technol. 2 (2013) M3120.

[86] K. Lota, V. Khomenko, E. Frackowiak, J. Phys. Chem. Solids 65 (2004) 295.

[87] H. Li, J. Wang, Q. Chu, Z. Wang, F. Zhang, S. Wang, J. Power Sources 190 (2009) 578.

[88] H. Guan, L.-Z. Fan, H. Zhang, X. Qu, Electrochim. Acta 56 (2010) 964.

[89] Y.Z. Wang, Q. Wang, H.Y. Xie, L.P. Ho, D.M.F. Tan, Y.Y. Diao, W. Chen, X.N. Xie, Nanoscale 4 (2012) 3725.

[90] A. Gupta, A.J. Akhtar, S.K. Saha, Mater. Chem. Phys. 140 (2013) 616.

[91] Y. Zhou, H. Xu, N. Lachman, M. Ghaffari, S. Wu, Y. Liu, A. Ugur, K.K. Gleason, B.L. Wardle, Q.M. Zhang, Nano Energy 9 (2014) 176.

[92] P.S. Matsumoto, J. Chem. Educ. 82 (2005) 1660.

[93] X. Xia, J. Tu, Y. Mai, X. Wang, C. Gu, X. Zhao, J. Mater. Chem. 21 (2011) 9319.

[94] S.K. Meher, G.R. Rao, J. Phys. Chem. C 115 (2011) 15646.

[95] Y. Gao, S. Chen, D. Cao, G. Wang, J. Yin, J. Power Sources 195 (2010) 1757.

[96] J.-K. Chang, C.-M. Wu, I.-W. Sun, J. Mater. Chem. 20 (2010) 3729.

[97] M. Toupin, T. Brousse, D. Bélanger, Chem. Mater. 16 (2004) 3184.

[98] N. Nagarajan, H. Humadi, I. Zhitomirsky, Electrochim. Acta 51 (2006) 3039.

[99] A. Bello, O.O. Fashedemi, J.N. Lekitima, M. Fabiane, D. Dodoo-Arhin, K.I. Ozoemena, Y. Gogotsi, A.T. Charlie Johnson, N. Manyala, AIP Adv. 3 (2013) 082118.

[100] V. Srinivasan, J. Electrochem. Soc. 144 (1997) L210.

[101] M.-S. Wu, H.-H. Hsieh, Electrochim. Acta 53 (2008) 3427.

[102] A. Bello, K. Makgopa, M. Fabiane, D. Dodoo-Ahrin, K.I. Ozoemena, N. Manyala, J. Mater. Sci. 40 (2013) 6707.

[103] T. Liu, W.G. Pell, B.E. Conway, Electrochim. Acta 42 (1997) 3541.

[104] Y.R. Ahn, M.Y. Song, S.M. Jo, C.R. Park, D.Y. Kim, Nanotechnology 17 (2006) 2865.

[105] T.-S. Hyun, J.-E. Kang, H.-G. Kim, J.-M. Hong, I.-D. Kim, Electrochem. Solid-State Lett. 12 (2009) A225.

[106] N. Miura, S. Oonishi, K. Rajendra Prasad, Electrochem. Solid-State Lett. 7 (2004) A247.

[107] D.L. Da Silva, R.G. Delatorre, G. Pattanaik, G. Zangari, W. Figueiredo, R.-P. Blum, H. Niehus, A.A. Pasa, J. Electrochem. Soc. 155 (2008) E14.

[108] C.-M. Huang, C.-C. Hu, K.-H. Chang, J.-M. Li, Y.-F. Li, J. Electrochem. Soc. 156 (2009) A667.

[109] X. Zhou, H. Chen, D. Shu, C. He, J. Nan, J. Phys. Chem. Solids 70 (2009) 495.

[110] A.M. Glushenkov, D. Hulicova-Jurcakova, D. Llewellyn, G.Q. Lu, Y. Chen, Chem. Mater. 22 (2010) 914.

[111] X. Zhou, C. Shang, L. Gu, S. Dong, X. Chen, P. Han, L. Li, J. Yao, Z. Liu, H. Xu, Y. Zhu, G. Cui, ACS Appl. Mater. Interfaces 3 (2011) 3058.

[112] C. Xu, H. Du, B. Li, F. Kang, Y. Zeng, J. Electrochem. Soc. 156 (2009) A73.

[113] Q. Yang, Z. Lu, J. Liu, X. Lei, Z. Chang, L. Luo, X. Sun, Prog. Nat. Sci. Mater. Int. 23 (2013) 1.

[114] B. Lu, D. Cao, P. Wang, G. Wang, Y. Gao, Int. J. Hydrogen Energy 36 (2011) 72.

[115] X.-M. Liu, Y.-H. Zhang, X.-G. Zhang, S.-Y. Fu, Electrochim. Acta 49 (2004) 3137.

[116] L. Wang, D. Wang, X.Y. Dong, Z.J. Zhang, X.F. Pei, X.J. Chen, B. Chen, J. Jin, Chem. Commun. (Camb). 47 (2011) 3556.

[117] X. Dong, L. Wang, D. Wang, C. Li, J. Jin, Langmuir 28 (2012) 293.

[118] Y. Song, J. Wang, Z. Li, D. Guan, T. Mann, Q. Liu, M. Zhang, L. Liu, Microporous Mesoporous Mater. 148 (2012) 159.

[119] Y. Tao, L. Zaijun, L. Ruiyi, N. Qi, K. Hui, N. Yulian, L. Junkang, J. Mater. Chem. 22 (2012) 23587.

[120] L. Zhang, X. Zhang, L. Shen, B. Gao, L. Hao, X. Lu, F. Zhang, B. Ding, C. Yuan, J. Power Sources 199 (2012) 395.

[121] A.S. Aricò, P. Bruce, B. Scrosati, J.-M. Tarascon, W. van Schalkwijk, Nat. Mater. 4 (2005) 366.

[122] Z. Gao, J. Wang, Z. Li, W. Yang, B. Wang, Chem. Mater. 23 (2011) 3509.

[123] O. Haas, E. J. Cairns, Annu. Reports Sect. “C” (Physical Chem. 95 (1999) 163.

[124] V. Khomenko, E. Raymundo-Piñero, E. Frackowiak, F. Béguin, Appl. Phys. A Mater. Sci. Process. 82 (2006) 567.

[125] J. Yan, Z. Fan, T. Wei, W. Qian, M. Zhang, F. Wei, Carbon 48 (2010) 3825.

[126] Y. Wang, W. Yang, S. Zhang, D.G. Evans, X. Duan, J. Electrochem. Soc. 152 (2005) A2130.

[127] Q. Pan, W. Tu, L. Ding, G. Mi, Wuhan Univ. J. Nat. Sci. 17 (2012) 200.

[128] P.W. Ruch, D. Cericola, a. Foelske-Schmitz, R. Kötz, a. Wokaun, Electrochim. Acta 55 (2010) 4412.

[129] Z. Zhang, Y. Lai, J. Li, Y. Liu, J. Cent. South Univ. Technol. 16 (2009) 247.

[130] M. Ue, J. Electrochem. Soc. 141 (1994) 2989.

[131] W. Liu, X. Yan, J. Lang, J. Pu, Q. Xue, New J. Chem. 37 (2013) 2186.

[132] M. Galiński, A. Lewandowski, I. Stepniak, Electrochim. Acta 51 (2006) 5567.

[133] H. Ohno, K. Fukumoto, Electrochemistry 76 (2008) 16.

[134] A. Lewandowski, A. Olejniczak, M. Galinski, I. Stepniak, J. Power Sources 195 (2010) 5814.

[135] A. Balducci, R. Dugas, P.L. Taberna, P. Simon, D. Plée, M. Mastragostino, S. Passerini, J. Power Sources 165 (2007) 922.

[136] R. Lin, P.-L. Taberna, S. Fantini, V. Presser, C.R. Pérez, F. Malbosc, N.L. Rupesinghe, K.B.K. Teo, Y. Gogotsi, P. Simon, J. Phys. Chem. Lett. 2 (2011) 2396.

[137] P. Thounthong, S. Raël, B. Davat, J. Power Sources 193 (2009) 376.

[138] J.P. Zheng, J. Electrochem. Soc. 152 (2005) A1864.

[139] J.R. Miller, Electrochim. Acta 52 (2006) 1703.

[140] R.N. Reddy, R.G. Reddy, J. Power Sources 124 (2003) 330.

[141] J.R. Miller, A.F. Burke, Electrochem. Soc. 17 (2008) 53.

[142] P. Harrop, V. Zhitomirsky, IDTechEx (2012).

[143] M. Inagaki, H. Konno, O. Tanaike, J. Power Sources 195 (2010) 7880.

[144] D. Weingarth, A. Foelske-Schmitz, A. Wokaun, R. Kötz, Electrochem. Commun. 18 (2012) 116.

[145] M.D. Stoller, R.S. Ruoff, Energy Environ. Sci. 3 (2010) 1294.

[146] J.R. Miller, A.F. Burke, Electric Vehicle Capacitor Test Procedures Manual, 1994.

[147] R.B. Wright, C. Motloch, FreedomCAR Ultracapacitor Test Manual, 2004.

[148] H. KuanXin, Z. Xiaogang, L. Juan, Electrochim. Acta 51 (2006) 1289.

[149] T. Brezesinski, J. Wang, J. Polleux, B. Dunn, S.H. Tolbert, J. Am. Chem. Soc. 131 (2009) 1802.

[150] V. Khomenko, E. Frackowiak, F. Béguin, Electrochim. Acta 50 (2005) 2499.

[151] W. Yang, Z. Gao, J. Wang, J. Ma, M. Zhang, L. Liu, ACS Appl. Mater. Interfaces 5 (2013) 5443.

[152] Allen J. Bard, L.R. Faulkner, Electrochemical Methods: Fundamentals and Applications, 2nd Editio, Wiley Online Library, New York, 2001.

[153] L. Cui, J. Li, X.-G. Zhang, J. Appl. Electrochem. 39 (2009) 1871.

[154] W. Sun, R. Zheng, X. Chen, J. Power Sources 195 (2010) 7120.

[155] H.-K. Song, H.-Y. Hwang, K.-H. Lee, L.H. Dao, Electrochim. Acta 45 (2000) 2241.

[156] H. Liu, P. He, Z. Li, Y. Liu, J. Li, Electrochim. Acta 51 (2006) 1925.

CHAPTER 3

3.0 EXPERIMENTAL PROCEDURE AND CHARACTERIZATION TECHNIQUES

All the experimental routes and characterization techniques used in this thesis will be presented and discussed in this chapter. The principles governing these characterization techniques will also be briefly elucidated. Detailed specific parameters for each material fabricated and tested will be discussed later in specific sections in chapter 4.

3.1 Chemical Vapor Deposition (CVD)

The chemical vapor deposition (CVD) system used in this study consists of a reaction chamber (a 2 inch diameter quartz tube) which was connected by flow meters to different gas supplies and enclosed in a furnace (as illustrated in figure 3.1). The gases used for graphene growth includes argon (Ar, grade 5 - 99.999%), hydrogen (H_2, grade 5 - 99.999%), methane (CH_4, grade 4.5 – 99.995%).

Chemical vapor deposition is a reliable, cost effective and efficient growth technique for the production of high quality, large area graphene samples with excellent electronic and optical properties suitable for device electrode applications [1,2]. The growth of graphene involves the use of a metal substrate which acts as a catalyst to lower the energy barrier of the reaction.

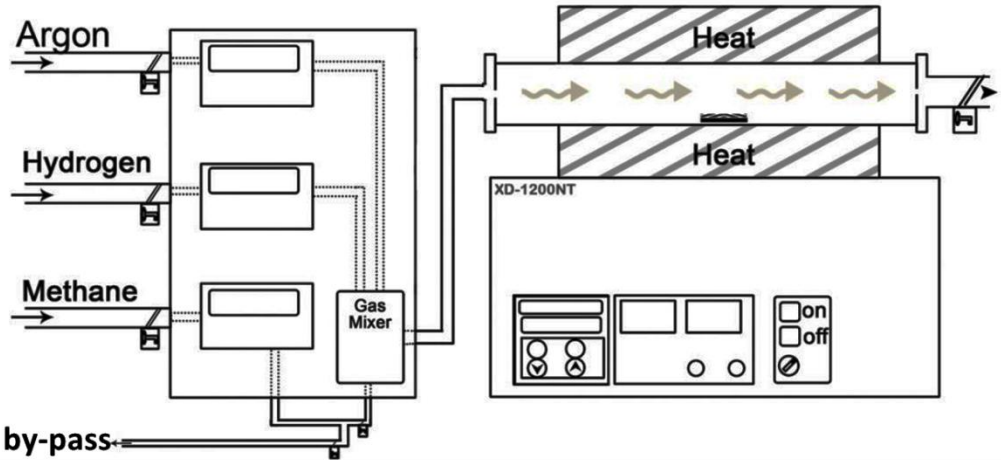

Figure 3.1: Schematic of a chemical vapor deposition system

The most common substrates used for graphene production are mainly transition metals substrates like copper (Cu) and nickel (Ni) [3,4]. Graphene growth on Ni-substrate has been proposed to be due to the segregation or precipitation process of carbons (C) [5]. Different cooling rates (quenching) with respect to thin films formation are required to suppress the formation of multiple-layers graphene (MLG) [6]. Fast, medium and slow rates are illustrated in figure 3.2 and this strongly affects the thickness and quality of graphene films produced due to the non-equilibrium nature of the precipitation process [7]. Medium cooling rates lead to optimal carbon segregation and produce few layer graphene while fast and slow cooling rates have been shown to give patches of graphene deposition on the Ni-substrate [4]. The microstructure of the nickel substrate also plays an important role in the formation of the graphene film morphology [8,9]. The growth mechanism of graphene on a Cu-substrate is based on a surface

adsorption process due to the characteristic low copper affinity to carbon and lower solubility at higher temperature [10].

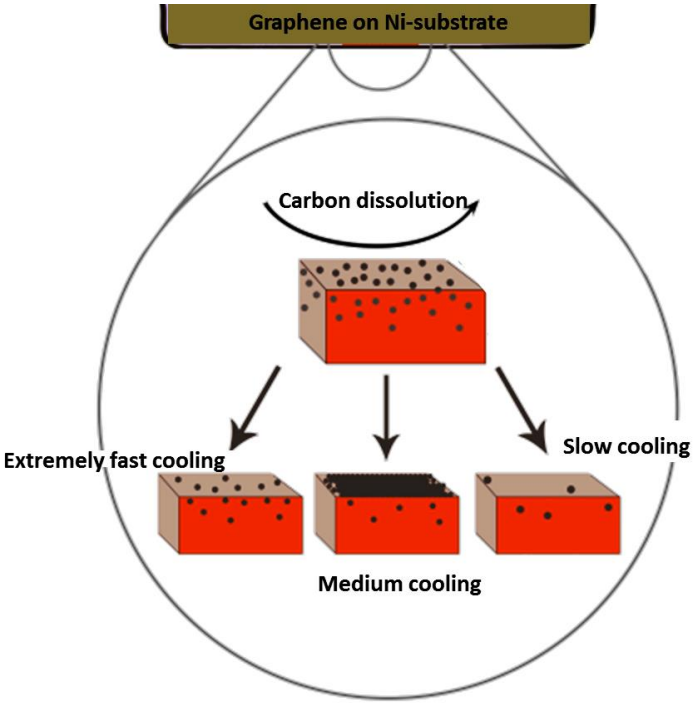

Figure 3.2: Illustration of the different cooling rates during graphene growth

This work mainly focuses on the growth of graphene on a polycrystalline three-dimensional (3D) nickel substrate (Alantum, Munich, Germany) usually referred to as nickel foam (NF). The growth process involves loading the reaction chamber with the precursor gases (Ar:H_2:CH_4) which pass through a flow meters to a gas mixer. The mixed gases pass through a high temperature heating zone and decompose to form radicals of carbons which dissolve into the grain boundaries of the metal substrate. This is subsequently followed by its out-diffusion to create layers of interconnected carbons

known as the graphene lattice. Methane acts as the source of carbon, argon acts as a carrier gas while hydrogen is used to remove any oxide impurities present and also increase the grain size of the transition metal catalyst during the growth process.

The NF-substrate of approx. 430 g m^{-2} in areal density and 1.8 mm average thickness was first pre-treated by annealing at a high temperature of 1000 °C to remove any surface contaminations like oil residues as well as inorganic materials that might have originated from the manufacturing or packaging process. Such contaminations might not be entirely gotten rid of using normal cleaning agents and thus annealing was done at atmospheric pressure in the presence of hydrogen and argon gas for 60 minutes. In addition to cleansing, it also facilitates the growth of larger grains necessary for efficient dissolution and out-diffusion of carbons [3].

The methane gas was then introduced into the reaction chamber after annealing, for the actual growth of the graphene layer at 968 °C and this process was left to proceed for a period of about 25 – 60 minutes. The quartz tube was pushed to a lower temperature region to ensure fast cooling of the sample [11,12]. During the cool down process, carbon atoms diffuse out of the solid Ni-C and precipitate on the Ni-surface to form graphene films [4]. The obtained product was referred to as nickel foam-graphene (NF-G) and will be used extensively in this thesis.

After the growth of graphene film on the nickel foam, the nickel template was removed by a wet chemical etching procedure. Firstly, the NF-G was soaked in 3.0 M hydrochloric (HCl) acid and left for 20 hours to completely remove the Ni-metal. The graphene foam

was then thoroughly washed with deionized water (DI) and dried in Ar/H_2 atmospheres to obtain graphene foam sample.

Composite materials were made using both NF-G substrate as current collector and the pristine graphene foam in other synthesis techniques like solvothermal growth techniques using chosen solvents like water, ethanol, tert-butanol etc.

3.2 Solvothermal Chemical Growth (SCG)

Solvothermal chemical growth (SCG) is an inexpensive and direct synthesis route used to prepare simple bulk and composite materials of different nano-architectures like nanowires, nanorods, nanoflowers, nanoribbons, nanosheets, etc. with their corresponding physical and chemical properties. These materials with their associated morphologies are suitable as electrode materials for energy storage devices [13–17].

The SCG technique is based on the ability of the solvents to serve as a medium for which material precursors (commonly salts) are dissolved or dispersed as the case may be, and subjected to higher temperature and pressure. The growth process is mostly carried out in sealed stainless-steel autoclave systems which is capable of withstanding the high temperature and pressure build-up associated with such processes. The main parameters that define the process kinetics of the chemical growth method and architecture of the final synthesized product include; the type of solvent used, the duration of the synthesis, the temperature of the reaction, the initial pH of the medium, the pressure in the system and the effective fill level in the chamber [18]. Typical

reactions involve an initial nucleation and growth of crystallites followed by their final assembly to form the desired architecture [19].

(a) **(b)**

Figure 3.3: Complete system for the solvothermal chemical growth; (a) shows the stainless steel autoclave system (b) shows the electric oven used for heating

The solvothermal process also allows for direct growth of the synthesized material on numerous substrates which enables the in-situ fabrication of advanced micro-, meso-, and macro-particulate hybrid structures [20,21].

Some key advantages of the solvothermal chemical growth technique include the ability to control and fine-tune the materials' morphology to fit the desired application and the environmentally friendly nature due to the closed system in which the reaction takes place.

3.2.1 Solvent-assisted chemical growth of metal-layered double hydroxides

The solvent-assisted chemical growth method is a bottom-up approach used in this study to synthesize layered double hydroxide (LDH) materials. It is also referred to as a controlled nucleation method involving aqueous precipitation of salts [22].

All chemicals used for this process were of analytical grade purity and were used as received without further purification. The porous metal layered double hydroxides (Nickel-Aluminum LDH) samples were produced by SCG using solvents such as water, ethanol, tert-butanol and a combination of water and alcohols in different volume ratios.

In a typical procedure, weighed masses of the precursor materials comprising of mainly hydrated salts containing the required metals were dissolved in a chosen solvent and continuously stirred. In the case of NiAl LDH nanosheets, 2.400 g of urea, 2.139 g of $Ni(NO_3)_2.6H_2O$ and 0.724 g of $Al(NO_3)_3.9H_2O$ salts were dissolved in 80 ml of water/ethanol mixture of a 1:1 volume ratio. The contents were stirred rigorously for 15 minutes before they were transferred into a 200 ml Teflon-lined autoclave vessel and subjected to a constant heating temperature of 140 °C for 18 hours. The pressure vessel was allowed to cool down naturally to room temperature and the product obtained was filtered, washed several times with deionized water (DI) to remove traces of unreacted materials with a final air drying overnight at 60 °C.

Nickel-Aluminum double hydroxide microspheres (NiAl DHMs) were also grown using tert-butanol (TBA) and water mixture as solvent in a 9:1 ratio. Briefly, 0.582 g of $Ni(NO_3)_2.6H_2O$ and 0.2270 g of $Al(NO_3)_3.9H_2O$ salts were added to a TBA-H_2O solution

containing 1.000 g of urea to give a 3:1 molar-ratio of Ni^{2+} to Al^{3+} ions which aids in tuning the morphology of the double hydroxides obtained. The solution was subjected to an ultrasonic treatment for 20 minutes to ensure an even dispersion and dissolution of the urea and salts, after which it was poured into the same 200 ml autoclave system. The content in the vessel was transferred to an electric oven where it was kept at 120 °C for 19 h. Subsequent procedures to obtain the final product was done in the same manner as described for the NiAl LDH material.

3.2.2 Exfoliation-assisted chemical growth of metal hydroxides-graphene composites

For the composite material with graphene foam, the same bottom-up approach is adopted. In this case however, the graphene foam enhances the electrical and surface area properties of the main matrix of which it is incorporated into. In the case of metal hydroxides nanosheets, it also acts as an exfoliating agent to obtain thinner sheets with higher surface area.

Nickel –aluminum layered double hydroxide –graphene foam (NiAl LDH-GF) composite was prepared by pre-adding 35 mg of GF to the ethanol-water mixture and ultrasonicating it for a period of 12 hours to evenly disperse the flakes of graphene in solution. This was then added to pre-weighed urea, $Ni(NO_3)_2.6H_2O$ and $Al(NO_3)_3.9H_2O$ precursors with continuous stirring vigorously for 15 minutes. The entire combination of NiAl LDH precursors with the graphene foam was then poured into the teflon-lined autoclave vessel and kept at 140 °C for 18 hours. The normal procedure for washing and

cleaning the final composite product (NiAl LDH-GF) described for the solvent-assisted chemical growth method in section 3.2.1 was also carried out here.

Zinc chloride hydroxide monohydrate ($Zn_5(OH)_8Cl_2\ H_2O$) microplatelets also known as "simonkolleite" (simonK) was combined with graphene foam to produce a simonkolleite-graphene foam (simonK/GF) composite. This was prepared by the usual process of dissolving the precursor materials which includes 2.974 g of zinc nitrate-hexahydrate ($Zn(NO_3)_2.6H_2O$), 0.588 g of sodium chloride (NaCl) and 4.102 g of hexamethylenetetramine ($C_6H_{12}N_4$, HMT) in an aqueous solution containing 25 mg of graphene foam which had been earlier subjected to ultrasonication. The contents were then emptied into an autoclave vessel and subjected to a heating in an electric oven at 110 °C for 19 hours. Subsequent washing and cleaning was done with deionized water with the final air drying step for 6 hours to obtain the simonK/GF composite for further characterization and analysis. SimonK samples alone were also prepared for comparison sake to see the effect of the incorporation of graphene foam on the properties of the composite material.

3.3 Materials characterization

3.3.1 Morphological studies

3.3.1.1 Scanning electron microscopy (SEM)

Scanning electron microscopy (SEM) is a characterization technique used to exhibit detailed information like the morphology/external topography and chemical composition of a specimen when using an energy dispersive x-ray spectrometer (EDS) with the scanning electron microscope. It uses focused electron beams which are generated from a schottky field emission source that utilizes a high applied field in an ultra-high vacuum. A field emission cathode consists of a wire shaped into a sharp tip (100 nm or less in radius) braced by a tungsten hairpin which emits electrons with electric field strength of 10 V nm^{-1} with a corresponding current density of 10^5 A cm^{-2} [23]. This is very much higher than electrons emitted from a thermionic source which have a current density of about 3 A cm^{-2}. The advantage of the field emitter is the size of the virtual probe (3 – 5 nm) that requires little demagnification to obtain a 1 nm diameter probe [23]. These electrons are accelerated through a set of deflector plates with electromagnetic lenses in an electron column to the sample surface. The kinetic energy of the accelerated electrons is altered due to the different types of repeated random scatterings, absorptions and deflections with atoms of the sample surface within the interaction purlieu [24]. These interactions between the primary electron beam and sample surface are recorded as signals by suitable detectors. The signals can be grouped into high energy emitted secondary electrons (SE^-) from inelastic collisions, emitted electromagnetic radiation (x-rays) from electron shell re-arrangements at the

energy levels and reflected electrons (RE^-, or back scattered electrons, BSE) from elastic scattering. The secondary electrons are used for imaging to obtain information about the morphology at the sample surface. High resolution images of the order of 1 nm are visible with SEMs having secondary electron detectors for secondary electron imaging. X-ray emission involves electron reshuffling within the energy levels of the electronic structure and as such, the characteristic x-rays are used to identify composition and measure elemental abundance in the sample. The BSE signal is linked to the atomic number of the signatory element at the sample surface. As such, the BSEs are often used for analytical SEM in conjunction with the x-ray to provide information about the elemental distribution of the sample.

The surface morphology and microstructure of all samples in this work were investigated using a Zeiss Ultra Plus 55 field emission scanning electron microscope (FE-SEM) operated at 2 kV in secondary electron detection mode. Samples were placed on the carbon double-sided tape attached to an aluminum substrate holder.

3.3.1.2 Transmission electron microscopy (TEM)

Transmission electron microscopy (TEM) also makes use of an electron beam to illuminate a sample area and create an image [24]. However, in the case of TEM technique, the high accelerating voltage electrons passes through the sample. The elastically scattered electrons within the sample form an imaging contrast [25] and this is magnified by a series of magnetic lenses until it is recorded by a photographic plate. This is then portrayed to a monitor for viewing real time images. A JEOL JEM-2100F

microscope operated at 200 kV was used in this work to analyze the nature of samples. TEM samples were prepared by dispersing the active material in powder form in ethanol and ultrasonicating to evenly disperse it. The ethanol solution containing the sample for study was dropped on a lacey carbon-coated copper grid and left for some minutes to dry before being loaded into the chamber for analysis.

3.3.2 Structural and Qualitative Phase studies

X-ray powder diffraction (XRD) is an analytical technique mainly used to identify the phases of crystalline materials [26] and other additional information such as lattice parameters and phase distribution using Rietveld confinement [27].

Similar to the SEM set-up described in section 3.3.1.1, electrons are also produced from a cathode and accelerated to an anode target (commonly made of copper or cobalt) where bombardment takes place to produce x-rays in a cathode ray tube. Depending on the anode material, characteristic x-rays of different wavelength (Cu-λ = 1.5406 Å or Co-λ = 1.7890 Å) is produced.

The XRD system is circular in nature and consists of the x-ray tube, a sample holder and an x-ray detector all lying on the focus circle. When the x-rays interact with the sample, constructive interference occurs where Bragg's law is satisfied: that is;

$$n\lambda = 2d \sin\theta \qquad (23)$$

where n is an integer value (1,2,3..), λ is the wavelength of the incident x-ray, d is the spacing between the planes in the atomic lattice, θ is the angle between the incident ray and scattering plane. The angle between the projection of the x-ray source and the detector is 2θ.

A detector records and processes the x-ray signals and converts it to a count rate which is then conveyed to a monitor. The XRD analysis is an effective route for obtaining the phases present in a sample since the wavelength of x-rays used is in the same order of magnitude as the interatomic distance and bond lengths in crystalline materials (~ 1 Å). In this study, the XRD spectra of all samples were collected using an XPERT-PRO diffractometer (PANalytical, Netherlands) with Fe-filtered Co-Kα radiation of 1.789 Å. The cobalt tube was operated at 35 kV and 50 mA with a scanning speed of 0.02° per step. The XRD patterns of all specimens were recorded in the 10.0° – 80.0° 2θ range with a counting time of 15.240 seconds per step. Qualitative phase analysis of the sample was conducted using the X'pert Highscore search & match software.

3.3.3 Gas Adsorption Analysis

Analysis of the adsorption/desorption isotherms gives information about the specific surface area, porosity, average pore volume and the general pore size distribution of a sample. In this study, all measurements were done using a Micromeritics TriStar II 3020 (version 2.00) surface area and porosity analyzer. The surface area measurements were obtained using the Brunauer-Emmett-Teller (BET) method with nitrogen gas at 77 K to obtain the adsorption/desorption isotherms. Pore size and pore volume were obtained

by the Barrett-Joyner-Halenda (BJH) method from the desorption branch of the associated isotherm. The process for obtaining the isotherms involved initially degassing the pre-weighed sample at 100 °C in order to remove any traces of moisture within the sample. The degassed sample was then transferred to the main chamber for the complete analysis using N_2 gas at very low pressure and 77 K. Initially, the sample is dosed with a specific amount of gas which is then evacuated to obtain the quantity of gas absorbed by the sample over a relative pressure range, P/P_0 (i.e. $0.01 < P/P_0 < 0.2$). The data points collected were displayed in the form an adsorption/desorption isotherm which is simply a plot of the quantity of gas absorbed as a function of relative pressure. The nature of the isotherm generated also gives an insight to the dominating pore size in the sample.

3.3.4 Raman Analysis

Raman spectroscopy is a non-destructive technique used to study the rotational, vibrational and other low frequency modes in a sample [28]. This technique is based on inelastic scattering of monochromatic light usually emitted from a laser in the visible, near infrared or near ultraviolet region. The laser light interacts with molecular vibrations, phonons or other excitations in the sample lattice resulting in a re-arrangement of the laser photons which provide chemical and structural information about the vibrational modes in the system. These modes are directly linked to the structural characteristics especially in carbon-based materials (e.g. graphene, graphite and carbon nanotubes) due to their flexibility in changing their hybridization states [29].

In particular for graphitic materials, Raman spectroscopy provides useful information on the in-plane vibrations of sp^2 carbon atoms (G-band), disorder (D-band), out-of-plane stacking order (2D band), in plane crystallite size, crystallographic orientation of graphene and graphene doping [30–33].

In this study, all Raman spectra were recorded with a high resolution Jobin–Yvon Horiba T64000 micro-Raman spectrometer equipped with a triple monochromator system to eliminate contributions from Rayleigh scattering. The samples were excited using the 514 nm wavelength of an argon excitation laser with a power of 1.5 mW at the source. The laser was focused on the sample using a 50X objective with an acquisition time of 60 – 120 seconds for each spectrum. Further analysis of the obtained spectra was done using LabSpec (Ver. 5.78.24) analytical software.

3.3.5 Fourier Transform Infra-red Resonance (FTIR) Spectroscopy

Fourier transform infrared (FT-IR) spectroscopy is a non-destructive qualitative analysis technique used to determine unknown sample types by identifying the functional groups present in the sample. This is done by exposing the sample to infrared (IR) radiation of which some part of it passes through (transmittance) the sample while some of it is absorbed (absorbance). A transmission, absorption or emission infrared spectrum is obtained over a wide spectra range expressed as wavenumbers.

FTIR spectra of all samples in this study were recorded using a Bruker Vertex 77v FT-IR spectrometer which was controlled using the Opus 7.0 spectroscopy software. FT-IR measurements were performed to determine the different vibration modes arising from

the IR-excitation of the samples. Furthermore, this technique gives a good insight into the type of the interlayer anions present especially in layered double hydroxide materials [13] which is studied in this work. All measurements were performed within a wavenumber range from 300 to 3600 cm^{-1}.

3.3.6 Thermal Gravimetric Analysis

The thermal stability of synthesized samples were performed using a Q600 Simultaneous TGA/DSC analyzer (TA Instruments, USA) to measure the material weight change as a function of temperature in a controlled environment over time [34]. The results from TGA analysis was used in determining the de-gassing temperature during BET analysis. TGA samples in this work were heated from ambient temperature to about a 1000 °C at a ramp rate of 5°C min^{-1} in nitrogen gas.

3.3.7 Electrochemical Analysis

The electrochemical properties of all samples coated on nickel-foam graphene templates were analyzed using cyclic voltammetry (CV), chronopotentiometry (CP) and electrochemical impedance spectroscopy (EIS) tests from a Biologic SP-300 PGSTAT workstation (Knoxville, TN 37930, USA) controlled by an EC-Lab v10.37 software. The SP-300 PGSTAT workstation is an electronic instrument designed to control the potential difference (E) applied to the working electrode (WE) with a current flow (in form of either a half cell or a full cell) and a reference electrode (RE) with no current.

A potentiostat on the other hand applies a current through the counter electrode (CE) whilst measuring the potential difference between the WE and RE.

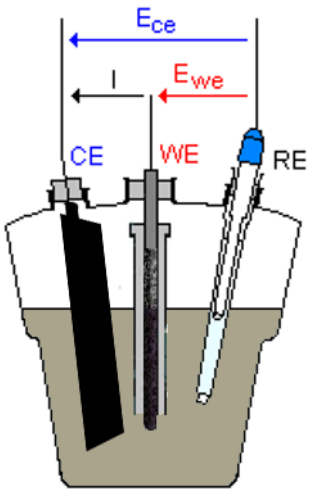

Figure 3.4: Three (3) electrode set-up used for electrochemical testing of active materials electrodes

The SP-300 PGSTAT generates characteristic cyclic voltammetry curves which give us information on the possible thermodynamics of electrochemical reactions of the system. The chronopotentiometry plot gives us an idea of the mechanism of charge storage along with its capacitance retention capability based on the shape of the plot and the time of discharge at a constant current density. The electrochemical impedance spectroscopy involves exciting the active material on the working electrode with a small-amplitude alternating current signal over a frequency range. Frequency sweeping across a range enables the reaction steps with different rate constants such as mass transport,

charge transfer and chemical reactions. The specific parameters applied for the different composite electrodes are reported in the specific sections where they are fully discussed.

All tests in this study were carried out in a three electrode configuration with the active material serving as the working electrode, a rectangular glassy carbon rod serving as the counter electrode and a Ag/AgCl (3 M KCl) serving as the reference. A 6M KOH aqueous solution served as the electrolyte which provides a medium for current flow and ion interaction.

3.4 References

[1] P. Blake, P.D. Brimicombe, R.R. Nair, T.J. Booth, D. Jiang, F. Schedin, L. A. Ponomarenko, S. V. Morozov, H.F. Gleeson, E.W. Hill, A.K. Geim, K.S. Novoselov, Nano Lett. 8 (2008) 1704.

[2] L. Gomez De Arco, Y. Zhang, C.W. Schlenker, K. Ryu, M.E. Thompson, C. Zhou, ACS Nano 4 (2010) 2865.

[3] X. Li, W. Cai, J. An, S. Kim, J. Nah, D. Yang, R. Piner, A. Velamakanni, I. Jung, E. Tutuc, S.K. Banerjee, L. Colombo, R.S. Ruoff, Science 324 (2009) 1312.

[4] Q. Yu, J. Lian, S. Siriponglert, H. Li, Y.P. Chen, S.S. Pei, Appl. Phys. Lett. 93 (2008) 113103.

[5] A. Reina, X. Jia, J. Ho, D. Nezich, H. Son, V. Bulovic, M.S. Dresselhaus, J. Kong, Nano Lett. 9 (2009) 30.

[6] X. Li, W. Cai, L. Colombo, R.S. Ruoff, Nanolett. 9 (2009) 4268.

[7] A. Umair, H. Raza, Nanoscale Res. Lett. 7 (2012) 437.

[8] A. Reina, S. Thiele, X. Jia, S. Bhaviripudi, M.S. Dresselhaus, J. A. Schaefer, J. Kong, (2009).

[9] X. Li, C.W. Magnuson, A. Venugopal, J. An, J.W. Suk, B. Han, M. Borysiak, W. Cai, A. Velamakanni, Y. Zhu, L. Fu, E.M. Vogel, E. Voelkl, L. Colombo, R.S. Ruoff, Nano Lett. 10 (2010) 4328.

[10] C. Mattevi, H. Kim, M. Chhowalla, J. Mater. Chem. 21 (2011) 3324.

[11] A. Bello, M. Fabiane, D. Dodoo-Arhin, K.I. Ozoemena, N. Manyala, J. Phys. Chem. Solids 75 (2014) 109.

[12] A. Bello, K. Makgopa, M. Fabiane, D. Dodoo-Ahrin, K.I. Ozoemena, N. Manyala, J. Mater. Sci. 40 (2013) 6707.

[13] W. Yang, Z. Gao, J. Wang, J. Ma, M. Zhang, L. Liu, ACS Appl. Mater. Interfaces 5 (2013) 5443.

[14] Y. Song, J. Wang, Z. Li, D. Guan, T. Mann, Q. Liu, M. Zhang, L. Liu, Microporous Mesoporous Mater. 148 (2012) 159.

[15] Y. Zhao, F. Xiao, Q. Jiao, J. Nanotechnol. 2011 (2011) 1.

[16] Z. Gao, J. Wang, Z. Li, W. Yang, B. Wang, Chem. Mater. 23 (2011) 3509.

[17] Y. Tao, L. Ruiyi, L. Zaijun, L. Junkang, W. Guangli, G. Zhiquo, RSC Adv. 3 (2013) 19416.

[18] V. Subramanian, H. Zhu, R. Vajtai, P.M. Ajayan, B. Wei, J. Phys. Chem. B 109 (2005) 20207.

[19] C. Burda, X. Chen, R. Narayanan, M. A El-Sayed, Chem. Rev. 105 (2005) 1025.

[20] J. Wang, Y. Song, Z. Li, Q. Liu, J. Zhou, X. Jing, M. Zhang, Z. Jiang, Energy & Fuels 24 (2010) 6463.

[21] S. Khamlich, A. Bello, M. Fabiane, B.D. Ngom, N. Manyala, J. Solid State Electrochem. 17 (2013) 2879.

[22] Q. Wang, D. O'Hare, Chem. Rev. 112 (2012) 4124.

[23] J.I. Goldstein, D.E. Newbury, P. Echlin, D.C. Joy, C.E. Lyman, E. Lifshin, L. Sawyer, J.R. Michael, Scanning Electron Microscopy and X-Ray Microanalysis, 3rd ed., Springer US, Boston, MA, 2003.

[24] R. Egerton, Physical Principles of Electron Microscopy - An Introduction to TEM, SEM, and | Springer, 1st Ed., Springer, 2005.

[25] D.B. Williams, C.B. Carter, Transmission Electron Microscopy, Springer US, Boston, MA, 2009.

[26] B.D. Cullity, S.R. Stock, Elements Of X Ray Diffraction, 3rd ed., Upper Saddle River, NJ : Prentice Hall, New Jersey, 2001.

[27] Charl Jeremy Jafta, Synthetic Strategies to Improve the Performance of Manganese Oxide Based Layered and Spinel Materials for Electrochemical Energy Storage, Thesis (PhD) University of Pretoria, 2015.

[28] D.. Gardiner, P.. Graves, H.. Bowley, Practical Raman Spectroscopy, Springer-Verlag Berlin Heidelberg, 1989.

[29] A. Ferrari, Solid State Commun. 143 (2007) 47.

[30] L.G. Cançado, K. Takai, T. Enoki, M. Endo, Y.A. Kim, H. Mizusaki, A. Jorio, L.N. Coelho, R. Magalhães-Paniago, M.A. Pimenta, Appl. Phys. Lett. 88 (2006) 163106.

[31] A. Jorio, C.A. Achete, E.H.M. Ferreira, L.G. Cançado, R.B. Capaz, Measuring Disorder in Graphene with Raman Spectroscopy, INTECH Open Access Publisher, 2011.

[32] M.A. Pimenta, G. Dresselhaus, M.S. Dresselhaus, L.G. Cançado, A. Jorio, R. Saito, Phys. Chem. Chem. Phys. 9 (2007) 1276.

[33] C. Casiraghi, A. Hartschuh, H. Qian, S. Piscanec, C. Georgi, A. Fasoli, K.S. Novoselov, D.M. Basko, A.C. Ferrari, Nano Lett. 9 (2009) 1433.

[34] A.W. Coats, J.P. Redfern, Analyst 88 (1963) 906.

CHAPTER 4

4.0 RESULTS AND DISCUSSION

In this chapter, the results obtained from all experimental procedures outlined in the preceding chapter are fully explained. The resulting publications from each of the specific research studies are also presented afterwards.

4.1 Incorporation of graphene into the main matrix of NiAl layered double hydroxides and NiAl double hydroxide microspheres

4.1.1 Introduction

The electrochemical performance of the supercapacitor device electrode is dependent on the nature of the active material as well as the substrate (current collector) on which the material is coated for redox capacitor applications.

Transition metal oxides and hydroxides are potential electrode materials for energy storage devices. Specifically, Layered double hydroxides (LDHs) and double hydroxide microspheres (DHMs) have generally been explored by researchers as faradaic materials for supercapacitors applications due to their excellent redox ability, tunable composition, flexible ion-exchangeability and environmentally friendly nature of preparation [1–4]. These properties combined with their mesoporous structure makes them suitable for electrochemical applications by providing the chemical sites necessary

for charge storage [5–7]. However, the problem of a relatively low electron transfer and mass diffusion due to restacking of LDH sheets affects their electrochemical properties. Likewise, the low surface area (< 1 m^2 g^{-1}) attributed to the nickel foam (NF) current collector even with its highly porous nature limits the overall electrochemical performance of the composite device electrode. Thus, tuning the morphology of the synthesized material as well as the introduction of a suitable template or framework in an attempt to reduce the restacking problem is ideal. This could improve electron transfer capability and enhance the surface interaction between the active LDH matrix and current collector.

Recent reports showcase the integration of electrochemical double layer capacitor (EDLC)-based carbonaceous materials of characteristic high energy density with redox-capacitive-based metal hydroxides with high power density [8–11]. Another study also reports the growth of a porous carbon layer to improve surface interaction [12].

In this section, mesoporous NiAl LDH and NiAl DHM were synthesized using a solvothermal technique with ethanol (ETH) and tert-butanol (TBA) as solvents, respectively. Graphene foam (GF) was incorporated into the main LDH material to obtain an LDH-GF composite. Initially, a continuous film of few-layer graphene was grown on pre-cleaned NF using atmospheric pressure chemical vapor deposition (AP-CVD) technique to obtain a nickel foam-graphene (NF-G) substrate as current collector. In order to obtain graphene foam, the NF-G was soaked in 3M aqueous HCl placed on a hot plate at 60 °C to etch away the NF template. After complete etching of the nickel,

the remaining graphene foam was washed several times in deionized water and dried in the oven to obtain the final graphene foam product

The results obtained from the analyses using different characterization techniques will be discussed in detail.

4.1.2 Result and discussion

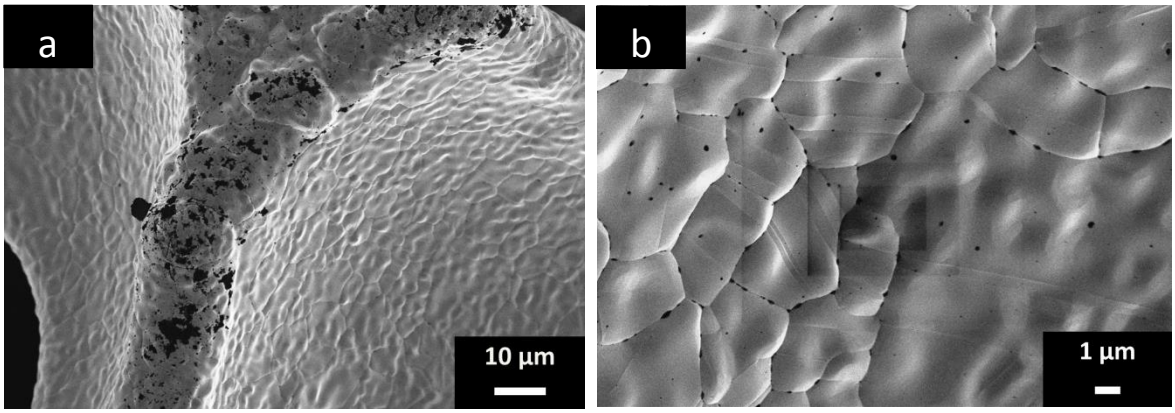

Figure 4.1: SEM of pristine nickel foam substrate (a) at low and (b) high magnification

Figure 4.1 shows the SEM micrographs of clean pristine NF templates (at low and high magnifications) used for the production of the NF-G template. The morphology depicts a typical polycrystalline nickel which clearly shows the grain sizes between 2 to 6 µm at higher magnification as seen in figure 4.1(b) and similar observations have also been reported by Jarrah *et al*. [12].

The morphology of the NF-G substrate from SEM images is displayed in figure 4.2 at low and high magnifications. The wrinkled nature of the continuous graphene layers

covering the nickel foam surface is observed much clearly in figure 4.2(a) and this is attributed to rapid cooling step carried out after the growth process.

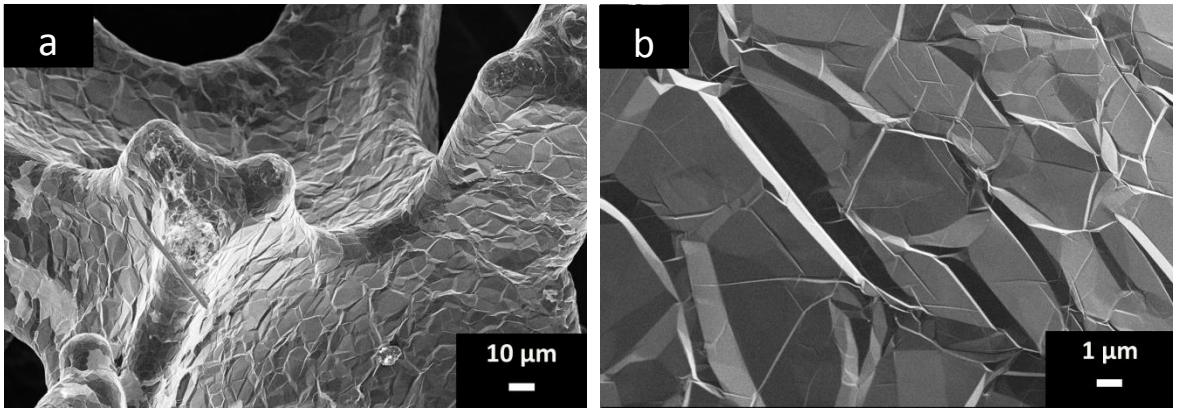

Figure 4.2: SEM of nickel foam-graphene substrate at (a) low and (b) high magnification

This is necessary for the out-diffusion of dissolved carbon atoms at the nickel grain boundaries. The thermal expansion coefficient mismatch between nickel and graphene leads to a strain release with subsequent wrinkling of the graphene layer [13].

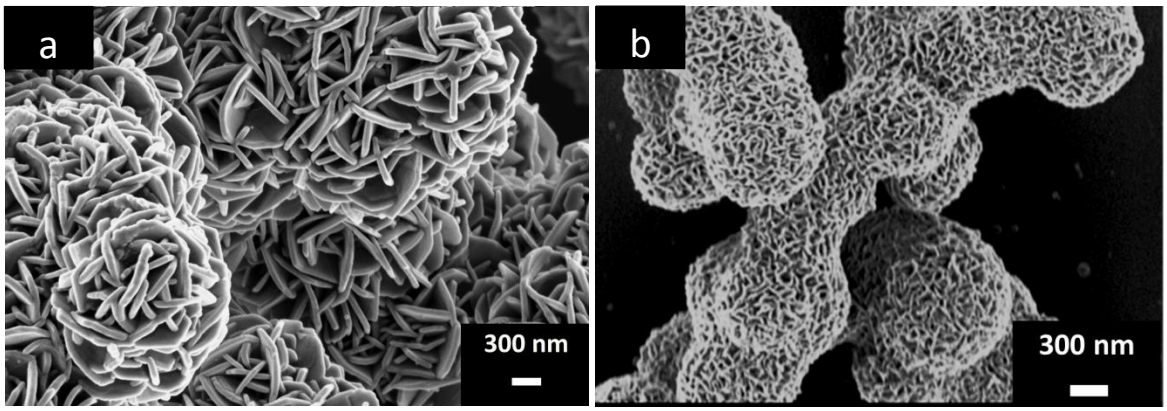

Figure 4.3: SEM micrograph of (a) NiAl LDH and (b) NiAl DHM nanostructures

Figures 4.3(a) and 4.3(b) are the SEM images of pristine NiAl LDH and NiAl DHM, respectively grown by a facile solvothermal technique. Both micrographs are characterized by nanosheets that are interlaced with other sheets to form an interconnected framework suitable for efficient interface reactions in electrochemical applications. The NiAl DHMs have their entire sheets forming a spherical microstructure with an average diameter of 1 µm. The different morphologies obtained for the same material precursors is partly linked to the nature of the solvent used in the synthesis process.

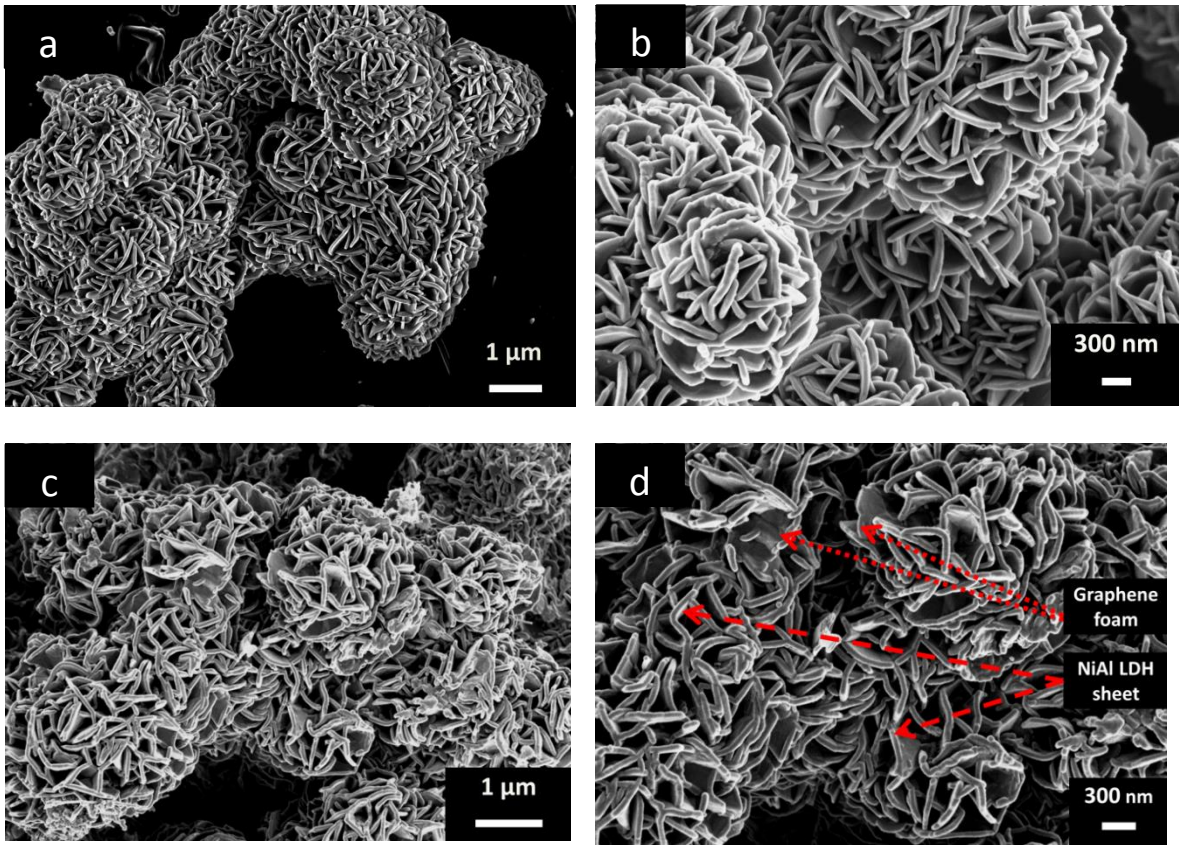

Figure 4.4: SEM micrograph of (a,b) NiAl LDH (c,d) NiAl LDH-GF composite

The morphology of the NiAl LDH before and after graphene foam has been incorporated into it is shown in the set of SEM micrographs in figure 4.4 at low and high magnifications. In figure 4.4(a) and figure 4.4(b), the nature of pristine NiAl LDH is displayed with nanosheets interconnected with each other. In figure 4.4(c) and figure 4.4(d), a successful interlacing of the LDH sheets with the graphene foam is obvious. The presence of graphene foam (GF) flakes is visible from the SEM images shown in figure 4.4(d) with the red dotted arrows used to distinguish the much thinner graphene foam flakes from the much thicker NiAl LDH sheets.

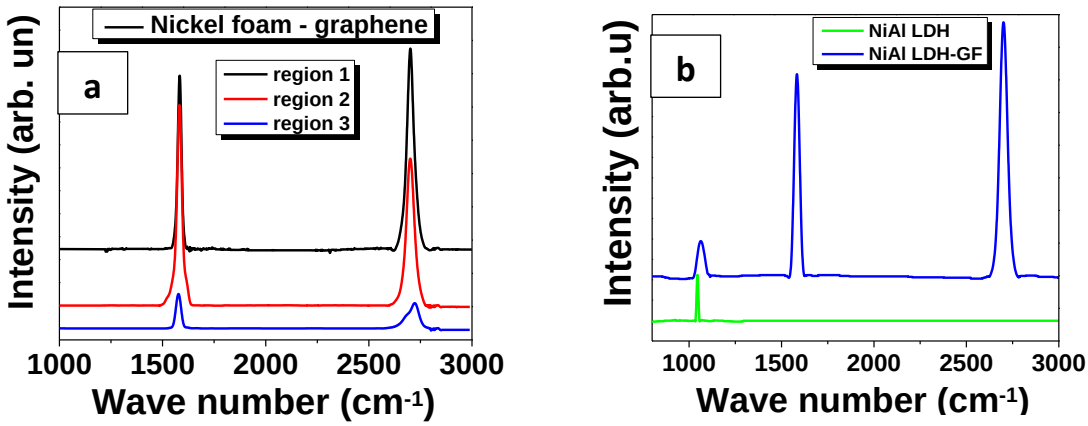

Figure 4.5: Raman spectra of (a) nickel foam-graphene (b) NiAl LDH and NiAl LDH-GF composite showing the distinct graphene and NiAl LDH peaks respectively

The Raman spectra in figure 4.5(a) for pure NF-G is taken in different regions of the sample to demonstrate the characteristic G-band and 2D-bands associated with graphene vibrational modes. This also confirms the complete covering of the NF surface

with graphene as discussed in the SEM images in figure 4.2. The G-band arises from the first-order scattering of the E_{1g} phonon for sp^2 carbon atoms in the wavenumber region of 1500 – 1600 cm^{-1}. The 2D peak in graphene is due to two phonons with opposite momentum in the highest optical branch near the A1 symmetry at K point [14,15].

Figure 4.5(b) shows the Raman spectra recorded for the NiAl LDH and NiAl LDH incorporated with GF (NiAl LDH-GF) samples. The characteristic vibrational band typical for the NiAl LDH/NiAl DHM material recorded at a wave number of approximately 1025 cm^{-1} is observed. The second spectrum for the NiAl LDH-GF also shows the LDH peak in addition to the G-band and 2D-bands associated with graphene vibrational modes described in figure 4.5(a).

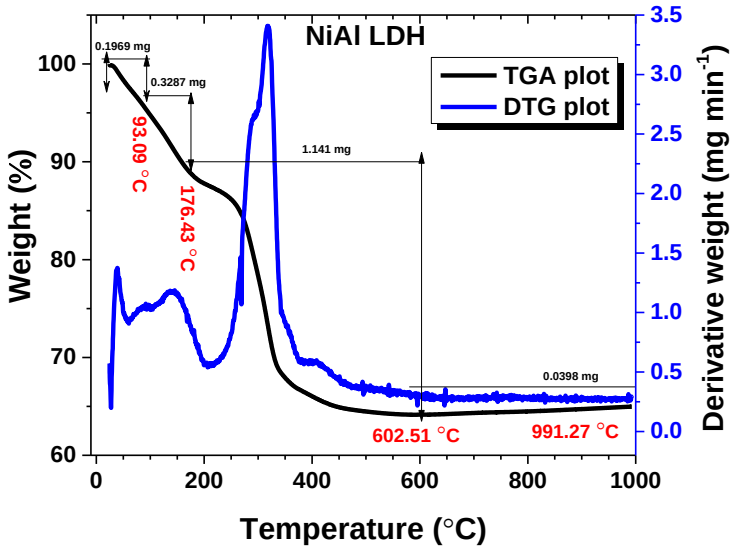

Figure 4.6: Thermal gravimetric analysis (TGA) of NiAl LDH

This is similar to earlier reports associated with NiAl LDH/graphene nanosheet composites [16] and thus confirms the successful interlacing of graphene with the LDH nanosheets.

In order to investigate the thermal stability of the double hydroxide materials, thermal gravimetric analysis (TGA) was also carried out on the NiAl LDH and NiAl DHM samples in nitrogen gas. As stated in chapter 3, this will give an idea of the ideal temperature to degas the samples during BET analysis. For the sake of simplicity, the TGA analysis was carried out for the pristine LDH samples alone and not the composites since reasonable BET specific surface area values are obtained from properly degased samples. The results obtained are shown in figure 4.6 and figure 4.7 respectively.

Figure 4.6 shows the TGA and the derivative of the thermal gravimetric (DTG) curves for NiAl LDH material.

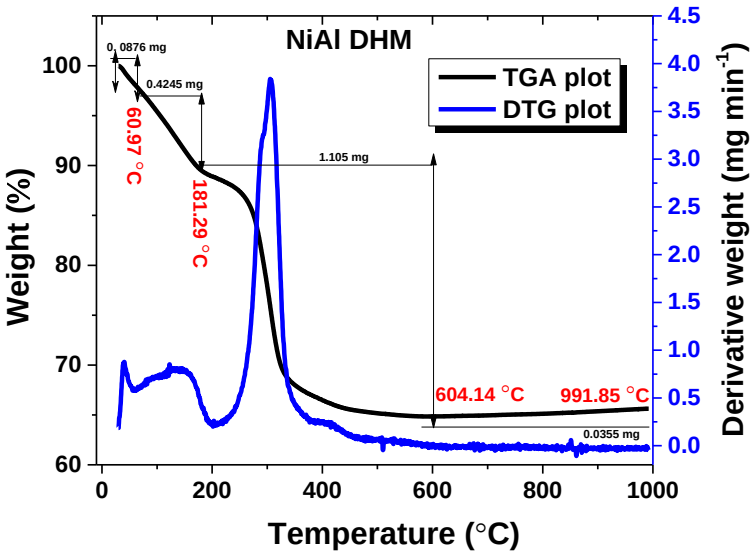

Figure 4.7: Thermal gravimetric analysis (TGA) of NiAl DHM

An initial combined significant decrease in the weight for the NiAl LDH sample of about 0.5256 mg (~10.09 wt. %) is observed which is likely due to loss of moisture and water (H_2O) molecules within the sample; these include both water physisorbed on the external surface of the crystallites as well as water that is intercalated in the interlayer arcades at 176.43 °C [19].

Another weight loss is observed at about 602.51 °C which is attributed to the dehydroxylation of the layers as well as removal of volatile species like carbon dioxide (CO_2) arising from the interlayer carbonate (CO_3^{2-}) anions [20].

Similar TGA and DTG profiles were also recorded for the NiAl DHM material with comparable weight losses as displayed in figure 4.7. The observed weight losses are also due to the same processes elucidated for the NiAl LDH sample.

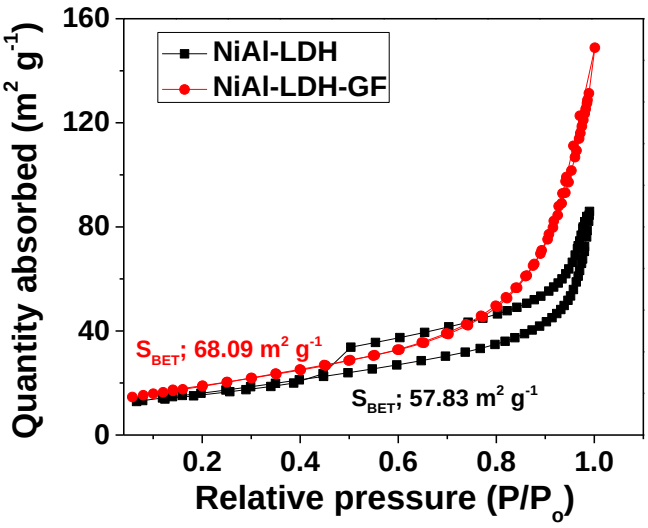

Figure 4.8: N_2 adsorption–desorption isotherms for NiAl-LDH and NiAl-LDH-GF

The physical adsorption/desorption of N_2 at 77K results shown in figure 4.8 displays the surface area of the NiAl LDH and NiAl LDH-GF samples. In the case of LDH alone, a type IV isotherm with a H3-type hysteresis loop ($P/P_o > 0.4$) appears which indicates the presence of mesopores in the LDH material [2,17] with an estimated specific surface area (SSA) of 57.83 $m^2 g^{-1}$. The addition of a highly porous GF produced a higher BET SSA of 68.09 $m^2 g^{-1}$ for the NiAl-LDH-GF thereby increasing the amount of available porous sites. The improvement of the specific surface area of the NiAl LDH material by the introduction of graphene foam is vital in order to ensure the mass transfer reduction of electrolyte during fast redox reactions [2].

The electrochemical behavior of the NiAl LDH and NiAl LDH-GF composite were investigated using cyclic voltammetry (CV) tests and are shown in figure 4.9 (a-d).

GF was added in three different masses, (25 mg, 35 mg & 45 mg) in order to analyze the effect of the incorporating varying amounts of graphene foam on the recorded specific capacitance. Cyclic voltammetry (CV) measurements are used to understand the macroscopic electrochemical surface reactions at the electrode material during operation. The CV curves of the NiAl-LDH-GF composite shown in figures 4.9(b - d) at different scan rates, exhibit higher current responses when compared to the pristine NiAl LDH, indicating a better capacitive performance.

The specific capacitance values obtained from the CV analysis (using equation 16) depicts an initial increase in specific capacitance as compared to the pristine NiAl LDH alone due to the increase in specific surface area and the creation of active mesoporous sites necessary for charge storage [18]. A subsequent decrease in specific capacitance is

observed with further increase in the amount of added GF. This might be due to the incomplete exfoliation of graphene sheets amongst the NiAl LDH sheets which limits the available surface area required for surface interactions. The summary of the specific capacitance values for the pristine NiAl LDH and the NiAl LDH-GF composite with various masses of GF is given in Table 2:

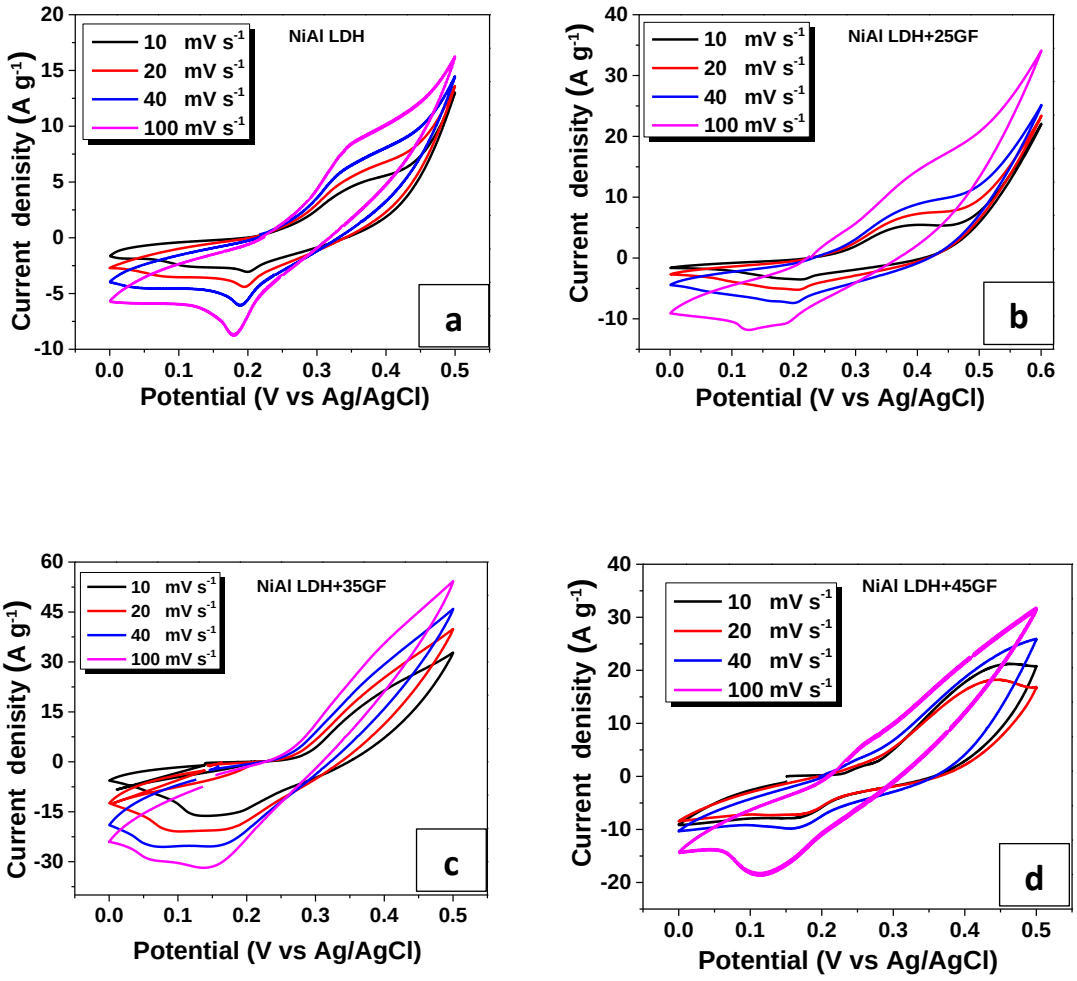

Figure 4.9: Cyclic voltammogram for (a) NiAl LDH and (b-d) NiAl LDH-GF composite with different amounts of GF at various scan rates

Table 2: Summary of specific capacitance values of NiAl LDH and NiAl LDH-GF composite with varying masses of GF

Scan rate	Pristine NiAl LDH	NiAl LDH+25mg GF	NiAl LDH+35mg GF	NiAl LDH+45mg GF
10 mV s^{-1}	401 F g^{-1}	706.6 F g^{-1}	**1228.6 F g^{-1}**	907.7 F g^{-1}
20 mV s^{-1}	229 F g^{-1}	385.4 F g^{-1}	**777.8 F g^{-1}**	532.4 F g^{-1}
40 mV s^{-1}	134.2 F g^{-1}	235.9 F g^{-1}	**474.6 F g^{-1}**	347.6 F g^{-1}
100 mV s^{-1}	66.6 F g^{-1}	144.8 F g^{-1}	**234.4 F g^{-1}**	179.9 F g^{-1}

A detailed summary of the results on the analysis of solvothermally synthesized NiAl double hydroxide microspheres (NiAl DHMs) and the influence of the substrate morphology on the electrochemical performance when applied as faradaic material electrode is presented in the attached publication. It should be noted that the use of “pseudocapacitor materials'' in the following publication should be regarded as ''faradaic materials“ for supercapacitors.

4.1.3 Publication 1: Solvothermal synthesis of NiAl double hydroxide microspheres on a nickel foam-graphene as an electrode material for pseudo-capacitors.

AIP ADVANCES **4**, 097122 (2014)

Solvothermal synthesis of NiAl double hydroxide microspheres on a nickel foam-graphene as an electrode material for pseudo-capacitors

Damilola Momodu,[1] Abdulhakeem Bello,[1] Julien Dangbegnon,[1] Farshad Barzeger,[1] Fatimeh Taghizadeh,[1] Mopeli Fabiane,[1] A. T. Charlie Johnson,[2] and Ncholu Manyala[1,a]
[1]*Department of Physics, Institute of Applied Materials, SARChI Chair in Carbon Technology and Materials, University of Pretoria, Pretoria 0028, South Africa.*
[2]*Department of Physics and Astronomy, University of Pennsylvania, Philadelphia, Pennsylvania 19104, USA*

(Received 12 August 2014; accepted 8 September 2014; published online 17 September 2014)

In this paper, we demonstrate excellent pseudo-capacitance behavior of nickel-aluminum double hydroxide microspheres (NiAl DHM) synthesized by a facile solvothermal technique using tertbutanol as a structure-directing agent on nickel foam-graphene (NF-G) current collector as compared to use of nickel foam current collector alone. The structure and surface morphology were studied by X-ray diffraction analysis, Raman spectroscopy and scanning and transmission electron microscopies respectively. NF-G current collector was fabricated by chemical vapor deposition followed by an ex situ coating method of NiAl DHM active material which forms a composite electrode. The pseudocapacitive performance of the composite electrode was investigated by cyclic voltammetry, constant charge–discharge and electrochemical impedance spectroscopy measurements. The composite electrode with the NF-G current collector exhibits an enhanced electrochemical performance due to the presence of the conductive graphene layer on the nickel foam and gives a specific capacitance of 1252 F g^{-1} at a current density of 1 A g^{-1} and a capacitive retention of about 97% after 1000 charge–discharge cycles. This shows that these composites are promising electrode materials for energy storage devices. © *2014 Author(s). All article content, except where otherwise noted, is licensed under a Creative Commons Attribution 3.0 Unported License.* [http://dx.doi.org/10.1063/1.4896125]

I. INTRODUCTION

The rapid development in the energy sector and the global economy has given rise to an urgent need for new technologies associated with the production and storage of energy. The uncontrollable depletion of fossil fuels and petroleum, with an increasing deterioration of the environment, has further increased the interest in energy research. In numerous applications, the most common, effective and practical technologies for electrochemical energy storage are batteries and electrochemical supercapacitors (ECs).[1,2]

ECs, (which comprises of electric double layer capacitors (EDLCs) or pseudocapacitors, based on their charge storage mechanism) have high power density, long cycle life and low maintenance cost as compared with batteries and conventional dielectric capacitors. Such outstanding characteristics are interesting for a wide range of applications such as mobile electronic devices, power/memory back-up systems, emergency units and hybrid vehicles.[1–4] However, the energy density of ECs is still an order of magnitude lower than that of the hybrid lithium-ion batteries in use today.[5] This limits their use in high-longevity and high-energy density applications. Thus there is an urgent need

[a]Author to whom correspondence should be addressed. Electronic mail: ncholu.manyala@up.ac.za

for the further development of high-performance electro-active and hybrid supercapacitive materials since the energy density is proportional to the specific capacitance of ECs.

Transition-metal oxides (MnO_2,[5,6] Fe_3O_4,[7] NiO)[8,9] and hydroxides ($Co(OH)_2$,[10,11] $Ni(OH)_2$)[12,13] are promising electrode materials for supercapacitor applications. The numerous studies carried out have yielded excellent supercapacitance values with some showing commendable energy densities which depict a promising future for these materials. Among these, a report by Bello *et al.*[5] illustrated using a simple hydrothermal reduction approach to anchor needle-like manganese oxide onto the surface of graphene foam (GF) grown by the atmospheric pressure chemical vapor deposition (AP-CVD) technique. The symmetric supercapacitor consisting of GF/MnO_2 composite exhibited a high capacitance value of 240 F g^{-1} at a current density of 0.1 A g^{-1} composite supercapacitors. A maximum energy density of 8.3 Whkg^{-1} was obtained, with a power density of 20 kWkg^{-1} and no capacitance loss after 1000 cycles. From the study, GF was seen as an excellent support for pseudo-capacitive oxide and hydroxide materials due to the combination of both electric double layer and pseudocapacitance properties.[5] Li *et al.*[13] also studied amorphous $Ni(OH)_2$ nanospheres fabricated by a simple green electrochemistry technique using cleaned graphite electrodes and obtained a specific capacitance of 153 F g^{-1} at a scan rate of 5 mV s^{-1}, with corresponding energy and power densities of 35.7Wh kg^{-1} and 490 W kg^{-1} respectively in an asymmetrical pseudocapacitor with activated carbon (AC) as the negative electrode.

Recently, layered-double hydroxides (LDHs) and double hydroxide microspheres (DHMs) containing transition metals have also been investigated as active electrode materials for supercapacitors.[14–20] A general chemical formula of $[M^{2+}_{1-x}M^{3+}_x(OH)_2]^{x+}[A^{n-}_{x/n}]^{x-}.mH_2O$ is used to synthesis LDH and DHM materials where M^{2+} and M^{3+} are divalent and trivalent cations respectively; A^n is a charge-balancing n-valent anion which usually comes from the precursor salts used in the preparation of the active material; and $x = M^{3+}/(M^{2+}+M^{3+})$. LDHs have an attractive redox property and since most of their growth techniques are environmentally friendly, they have great potential application as electrode materials for pseudocapacitors.[15,16] In addition, their tunable composition and flexible ion-exchangeability also add to the wide range of applications, including sensors, catalysts, drug delivery and matrix materials in hybrid composites, etc.[17,21–23] In particular, the growing interest in their use in electrochemical capacitors is generally due to the active chemical sites present for both electric double layer capacitors and pseudocapacitors.[24] However, they are characterized by relatively low electron transfer and mass diffusion which inhibits the rate of charge–discharge properties and affects their overall electrochemical performance. Hence a composite material that will provide a suitable support for the active material while improving the surface interaction between the current collector and the LDH material is ideal.

Graphene-based supercapacitor electrodes have attracted much attention due to their unique properties such as high electrical conductivity, high surface area and robust mechanical properties.[25–28] In recent studies, Khamlich *et al.*[26] used an in situ aqueous chemical growth technique of simonkolleite ($Zn_5(OH)_8Cl_2 \cdot H_2O$) onto nickel foam-graphene (NF-G) to form a NF-G/simonkolleite composite that acted as an active electrode material with a specific capacitance of 350 F g^{-1} at 0.7 A g^{-1}. Another report by Dong *et al.*[27] adopted an innovative strategy of in situ growth of cobalt oxide (Co_3O_4) nanowires on 3D graphene foam grown by CVD. The graphene/Co_3O_4 composite was used as a monolithic free-standing supercapacitor electrode and exhibited a high specific capacitance of ~1100 F g^{-1} at a current density of 10 A g^{-1} with excellent cycling stability after 1000 cycles. Despite these achievements, if the desire to store energy efficiently is to be met, the need to synthesize materials with higher specific capacitance, combined with an excellent rate performance and even better long-lasting stability, is still crucial. In this regard, most recent studies are therefore inclined towards achieving well-defined micro/nanostructures with excellent surface properties, better electrochemical performance, higher electrical conductivity and adequate pore size distribution in order to enhance interface reactions and enhance the mass/electron transfer of the electroactive species during faradaic redox reactions.[17,29] Song *et al.*[29] used a solvothermal technique in which the ratio of ethanol/water was varied to obtain different structures of NiAl LDHs. The sample prepared with 100% ethanol had a specific surface area of about 300 m^2 g^{-1}. According to their report, 3D flowerlike porous structures assembled by 2D anisotropic LDH nanosheets were obtained using an ethanol solvent alone during the solvothermal growth. Tao *et al.*[30] also

used a tertbutanol-water (TBA-H_2O) mixture as a structure-directing agent to tune the morphology and nanostructure of nickel/cobalt double hydroxide microspheres (Ni-Co DHM). By varying the TBA:H_2O ratio, a unique microspherical architecture of synthesized Ni-Co DHMs was obtained with a 9:1 (TBA:H_2O) ratio with high supercapacitance and excellent capacitance retention at a cycling current density of 10 A g^{-1}.

In this study, TBA was also adopted as a structure-directing agent to fabricate nickel-aluminum double hydroxide microspheres (NiAl DHMs). These unique architectures could potentially improve the faradaic redox reactions and mass transfer. Thus, the pseudocapacitive performance of these microspheres was measured. The active material was coated on a nickel foam-graphene (NF-G) current collector prepared by AP-CVD technique and the electrochemical characterization was performed in a three-electrode configuration. This active electrode exhibited an improved capacitance on NF-G compared with when nickel foam (NF) alone was used as the current collector. Good cyclic retention of 97% after 1000 cycles was also observed for the NiAl DHMs on NF-G current collector. These results demonstrate that the NiAl DHMs are possible material for use in energy storage/conversion devices.

II. EXPERIMENTAL

A. Material Synthesis

1. Synthesis of NiAl DHMs

Urea (Merck, purity $\geq$ 98%), Ni $(NO_3)_2.6H_2O$ and Al $(NO_3)_3.9H_2O$ (Sigma-Aldrich, purity $>$ 99.99%) were used as received without any further purification. The NiAl DHMs were synthesized by a facile and environmentally friendly solvothermal technique with a TBA-H_2O mixture used as solvent, in a ratio of 9:1. In a typical synthesis procedure, 1.8 mmol of $Ni^{2+}$and 0.6 mmol of Al^{3+} salts were added to a TBA-H_2O solution containing 0.5 g of urea. The solution was subjected to ultrasonic treatment for 20 minutes to ensure complete dispersion and dissolution of the salts, after which it was poured into a 200 ml Teflon-lined hydrothermal autoclave system. The vessel was transferred to an electric oven where it was kept at 120 °C for 19 h. After this reaction time, the vessel was allowed to cool down naturally to room temperature. Finally, the solution was filtered and the product was washed several times with deionized water and subsequently left to dry in an oven at 60 °C for 12 h.

2. Synthesis of nickel foam-graphene (NF-G) current collector

The nickel foam-graphene current collector was prepared by an AP-CVD technique. Briefly, a known mass of compressed circular nickel foam template (Alantum, Munich, Germany), with an areal density of 420 g m^{-2} and a diameter of 16 mm, was placed in a quartz tube for the CVD growth of graphene. The nickel foam was first annealed at 800 °C in the presence of Ar and H_2 gas for 60 minutes, prior to the introduction of the carbon source (CH_4 gas) at 1000 °C. The flow rates of the gases Ar:H_2:CH_4 were 300:9:15 SCCM respectively. After 60 minutes of deposition, the samples were rapidly cooled by manually pushing the quartz tube to a lower temperature region.

3. Electrode preparation

The working electrode was fabricated using the method described in the earlier report by Bello *et al.*[5] The procedure involved mixing 80 wt. % of the active material (NiAl DHM powder) with 10 wt. % of carbon black (CB) and 10 wt. % polyvinylidene difluoride (PVdF) binder in an agate mortar. A paste made from this mixture is achieved by adding a few drops of 1-methyl-2-pyrrolidinone (NMP) to the mixture. The paste was coated on the NF-G and also on the NF current collectors respectively, for comparison. The coated samples were dried in an oven at 60 °C for 12 h to ensure complete evaporation of the NMP.

B. Material Characterization

Scanning electron microscopy (SEM) and transmission electron microscopy (TEM) analyses were carried out to reveal the morphology and microstructure of the sample using a Zeiss Ultra Plus 55 field emission scanning electron microscope (FE-SEM) operated at an accelerating voltage of 2.0 kV, and a JEOL JEM-2100F microscope operated at 200 kV respectively. Typically, SEM and TEM samples were prepared by dispersing them in ethanol and dropping them on glass substrates and lacey carbon-coated copper grids respectively for analysis. The sample was also characterized using powder X-ray diffraction (XRD). An XPERT-PRO diffractometer (PANalytical BV, Netherlands) with theta/theta geometry, operating a cobalt tube at 35 kV and 50 mA, was used. The XRD patterns of all specimens were recorded in the 10.0° – 80.0° 2θ range with a counting time of 15.240 seconds per step. Qualitative phase analysis of the sample was conducted using the X'pert Highscore search match software. Fourier transform infrared (FT-IR) spectra of the NiAl DHMs were recorded using a Bruker Vertex 77v FT-IR spectrometer, while the Raman spectra were obtained using a Jobin–Yvon Horiba TX 6400 micro-Raman spectrometer equipped with a triple monochromator system to eliminate contributions from Rayleigh scattering. The samples were excited using the 514 nm wavelength of an argon laser. The laser was focused on the sample using a 509 objective with 100x magnification and the acquisition time of each spectrum was 60 s. Surface area measurements were obtained using the Brunauer-Emmett-Teller (BET) method with N_2 gas. Pore size and pore volume were obtained using Barrett-Joyner-Halenda (BJH) method from the desorption branch of the isotherm.

C. Electrochemical Measurement

The capacitive properties were investigated using a Bio-Logic SP300 workstation (Knoxville TN 37930, USA) in a three-electrode configuration controlled by the EC-Lab® V10.37 software. The electrochemical test was performed also in a three-electrode configuration with the as-prepared NiAl DHM serving as the working electrode in 6 M potassium hydroxide (KOH) electrolyte, glassy carbon plate as the counter electrode and Ag/AgCl (3 M KCl) as the reference electrode.

The cyclic voltammetry tests were carried out in the potential range of 0 to 0.5 V (vs. Ag/AgCl) at different scan rates ranging from 5 to 100 mV s^{-1}. The galvanostatic charge–discharge measurements were also carried out at different current densities from 1 to 5 A g^{-1} and the electrochemical impedance spectroscopy (EIS) measurements were performed in the frequency range of 100 kHz–10 mHz.

III. RESULTS AND DISCUSSION

A. Morphology and Structure

Fig. 1 shows the morphology of the NiAl DHMs from microscopy analysis. Figs. 1(a) and 1(b) show nanoflakes interlaced with each other to form spherical microstructures with an average diameter of 1 μm at different magnifications. Thin flake-like structures are observed from the TEM micrographs, as shown in Figs. 1(c) and 1(d) also at different magnifications. These structures are ideal for electrochemical applications that involve interface reactions. Similar structures were obtained in earlier work by Tao *et al.*[30] in which Ni-Co hydroxide microspheres were hydrothermally synthesized in the same TBA:H_2O ratio of 9:1. The mechanism of the formation was explained to be due to the viscous nature and the spatial structure of the TBA solvent compared with other similar small molecule solvents.

In a particular ratio of TBA:H_2O, the TBA molecules self-assemble to form a nanoemulsion with the surface necessary for the growth of nanoflakes during the solvothermal process.[30,31] To describe the possible formation of the NiAl DHMs, which are spherical layered double hydroxides (LDHs), we refer to the Ostwald ripening mechanism which involves the nucleation and growth of NiAl LDH crystals.[29] In other words, in the presence of a mixture of Ni^{2+} and Al^{3+} salts, the continuous supply

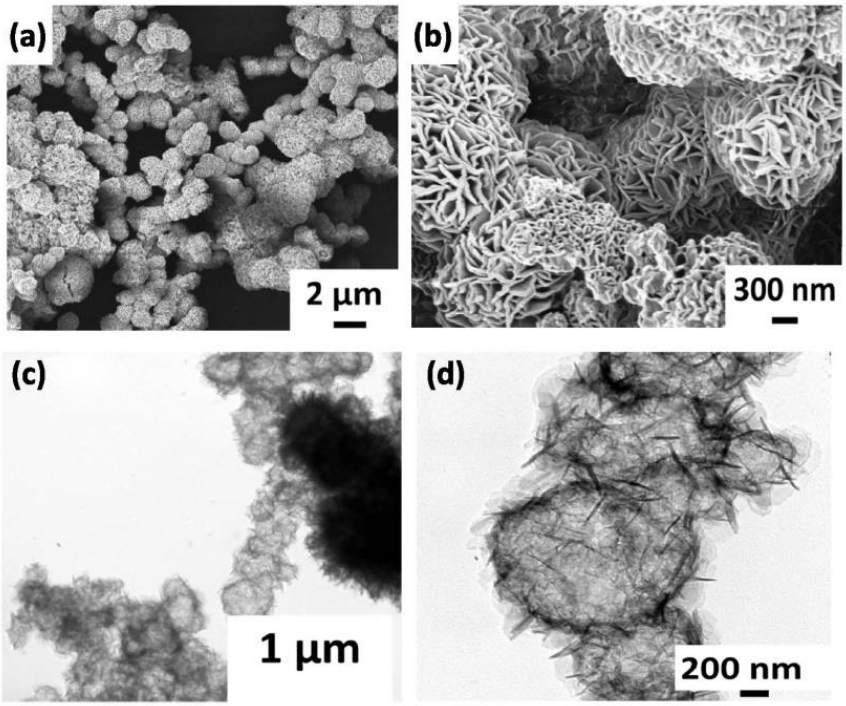

FIG. 1. (a, b) SEM micrograph of NiAl DHM; (c,d) TEM images of NiAl DHM at different magnifications.

of carbonate (CO_2^-) and hydroxide (OH^-) at a controlled rate from urea decomposition leads to the formation of the founding double hydroxide nanoparticles.[14]

The whole evolution/growth process could be likened to the three-stage process reported in previous studies[32] which involves a fast nucleation of amorphous primary particles, followed by crystal growth and final self-assembly. Over the course of the reaction, the concentration of the reactants in the reaction medium is decreased and a chemical equilibrium between the solid–liquid interfaces is established.

Meanwhile, the smaller interior crystallites are still in a non-equilibrium state. In this process, the exterior crystallites will serve as starting points to attract the smaller metastable crystallites. Subsequently, double hydroxide nanosheets gradually grow into their final form.[33] Many forces contribute to this unique structure, including electrostatic forces, crystal–face interaction, hydrogen bonds and van der Waals forces.[34]

The SEM micrographs in Fig. 2(a) to 2(d) display the morphology of the NF and NF-G current collectors at different magnifications. Fig. 2(b) shows the grain boundaries of nickel at higher magnifications, while the wrinkled nature of continuous few-layer graphene covering the nickel surface is shown in Fig. 2(d). The wrinkles are formed during the rapid cooling process that is necessary for the out-diffusion of carbon atoms onto the NF surface to form graphene layers. Due to the difference in the thermal expansion coefficients of the NF substrate and the grown graphene layer, these wrinkles appear as a result of the release of strain occurring from this mismatch.[35] The SEM micrographs in Figs 2(e) and 2(f) show the nature of the coating of the NF-G current collector with the NiAl DMH active material mixed with carbon black and PVdF binder. The active material is seen to fill in the pores of the NF-G current collector material. The spherical nature of the active material is seen to be retained in the higher magnification image of Fig. 2(f), although other materials have been added to form the paste coated onto the NF-G.

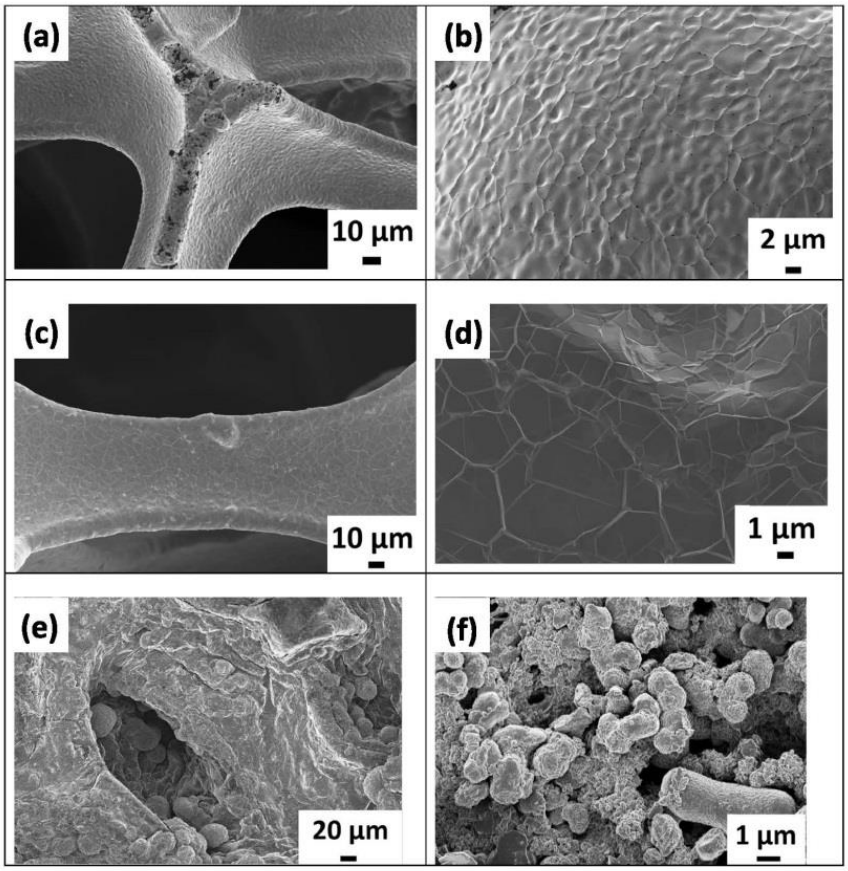

FIG. 2. SEM micrograph of (a,b) NF; (c,d) NF-G grown by CVD at different magnifications; (e, f) NiAl DHM paste coated on NF-G at different magnifications.

Figs 3(a) and 3(b) show the XRD patterns of the synthesized NiAl DHM powder and the composite electrode material, with typical diffraction peaks indexed to a hydrotalcite-like structure for LDH [Joint Committee on Powder Diffraction Standards (JCPDS) 15-0087/01-089-1777)], Ni and graphene respectively. The NiAl DHM peaks are also similar to those reported in earlier studies[14] in which characteristic reflection patterns of the LDH structure were studied, showing strong peaks with their relatively high crystallinity. However, these peaks exhibit a shift due to the nature of the X-ray source (cobalt) used in the analysis of the samples. For example, the reflection from the (003) plane with a strong diffraction peak usually ascribed to the 2θ angle of $\sim 11.30°$[14] is now observed at 13.1°. Likewise, similar peak shifts exist for other planes, such as the (006), (015), (018) and (110) planes, which show diffraction peaks at 2θ values of 26.7°, 40.7°, 47.5° and 72.7° respectively. The shifts are due to the difference in wavelength of the incoming X-rays which are dependent on the X-ray source, according to the Bragg equation: $n\lambda = 2d \sin\theta$. In general, X-rays from a cobalt source ($\lambda = 1.79$ Å) with longer wavelengths result in greater 2θ positions compared with those from a copper source ($\lambda = 1.54$ Å). The former usually allows the observation of low-angle peaks that are not observable using the shorter wavelength X-rays and provides better peak separation.[36]

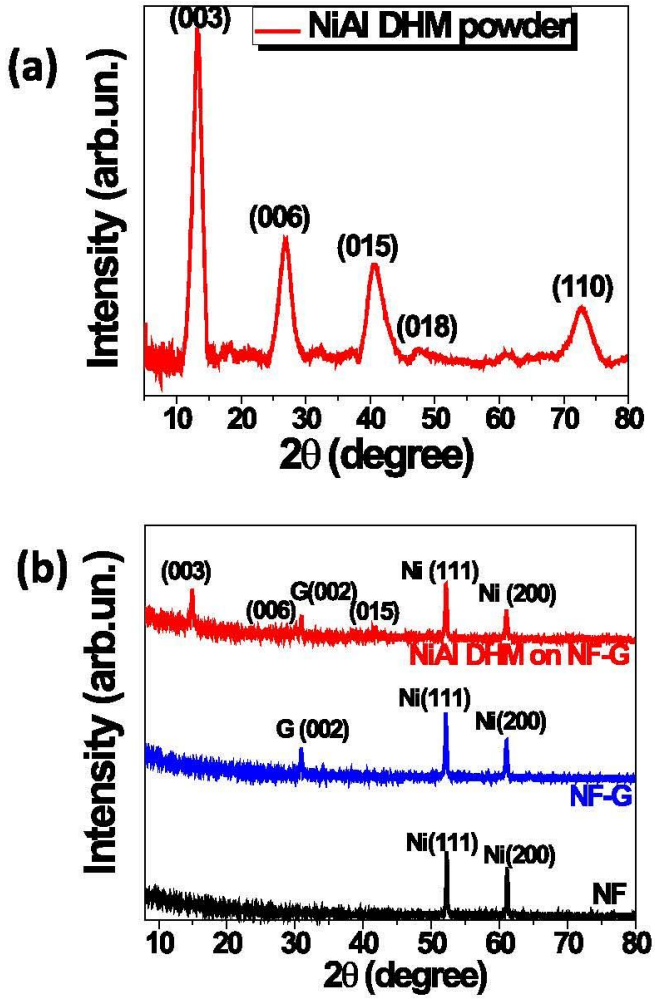

FIG. 3. (a) XRD patterns of NiAl DHM powder and (b) XRD pattern of NF, GF, NF-G and NiAl DHM on NF-G.

These observed peaks indicate that the sample analyzed is a layered structure belonging to a hydroxide layered system and to NiAl DHM in particular. The *d*-spacing of the (003) and (006) planes are dependent on the charge and the size of the charge-balancing interlayer anion. When CO_3^{2-} is the interlayer anion, the *d*-spacing values are approximately 0.78 nm and 0.39 nm for the (003) and (006) planes respectively.[37,38] From the position of the (003) and (006) reflections, *d*-spacing values of 0.78 nm and 0.39 nm were obtained when calculated with the XRD data thus confirming the CO_3^{2-} intercalation. The CO_3^{2-} ions could arise from the deionized water and the decomposition of urea. The gallery height, which was calculated by subtracting the thickness of the brucite-like layer (0.477 nm)[39] from the thickness of the unit layer ($d_{(0\,0\,3)}$ basal spacing), is 3.07 nm. This value is lower than the corresponding free anion diameter (D = 0.37 nm), which implies strong interaction of the anion with the brucite-like layer.[40] The XRD patterns for the coated material on the different current collectors are also shown in Fig. 3(b) with their characteristic peaks. The XRD pattern for NF consists of two very strong peaks recorded at 52.1° and 60.9°, which could be assigned to the (1 1 1), (2 0 0) phase of nickel. The diffraction peak at $2\theta = 31°$ corresponds to the

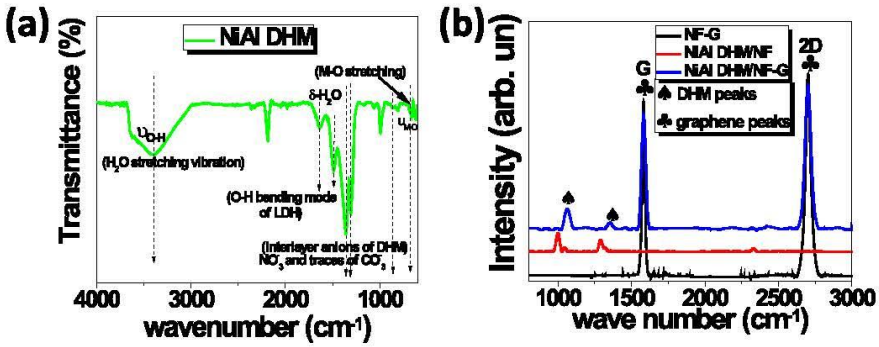

FIG. 4. (a) FT-IR spectra for NiAl DHM and (b) Raman spectra for NF-G, NiAl DHM on NF and NF-G.

(002) reflection of hexagonal graphitic carbon, which is an indication of the presence of graphene (G).[8,41] For the XRD pattern of the active material on the NF-G current collector, all characteristic reflections of NiAl DHMs, NF and G are observed and indexed as shown.

Figs. 4(a) and 4(b) show the FT-IR and Raman spectroscopic images of the NiAl DHM on the NF and NF-G templates respectively. These measurements were performed to determine the nature of the material from the different vibration modes arising from the excitation of the samples. Furthermore, this technique can give good insights into the type of the interlayer anion. The infrared spectrum of the NiAl DHM powder is shown in Fig. 4(a) within a range from 600 to 4000 cm^{-1}. A broad absorption band centered at about 3408 cm^{-1} corresponds to the O-H stretching vibrations of the interlayer water molecules and the hydrogen-bonded OH-groups of the hydrotalcite layers accompanied by bending at 1643 cm^{-1}.[17,42] The peaks at 1300 and 1363 cm^{-1} originate from vibrations of the interlayer CO_3^{2-} anions.[17] This is in good agreement with the XRD results which show evidence of the presence of CO_3^{2-} charge-balancing interlayer anions. The remaining bands below 800 cm^{-1} are attributed to metal-oxygen (M-O)/metal-hydroxyl (M-OH) stretching and bending modes (with M corresponding to Ni and Al).[42–44]

Fig. 4(b) shows the Raman spectra for NF-G, NiAl DHM on NF (NiAl-DHM/NF) and NF-G (NiAl-DHM/NF-G) respectively. The Raman spectrum in Fig. 4(b) for pure NF-G shows the characteristic G-band and 2D-bands associated with graphene vibrational modes. The G-band arises from the first-order scattering of the E_{1g} phonon for sp^2 carbon atoms in the wavenumber region of 1500 – 1600 cm^{-1}.[45] The 2D peak in graphene is due to two phonons with opposite momentum in the highest optical branch near the A_1 symmetry at K point.[46] The Raman spectra for NiAl DHM/NF and NiAl DHM/NF-G exhibit features that are typical of NiAl hydrotalcite structure. The peaks at 1049 cm^{-1} and 1331 cm^{-1} are typical Raman peaks related to NiAl LDH.[19]

The supercapacitive performance of the active electrode material is dependent on its ability to accommodate as much active electrochemical sites for charge storage during operation. The presence of suitable mesopores within the electrode material is also ideal to ensure the reduction of mass transfer of electrolyte during fast redox reactions and facilitates power delivery.[17]

The physical adsorption/desorption of N_2 at 77K results shown in Fig. 5 displays the surface area and pore size distribution for the prepared NiAl DHM powder sample. Fig. 5(a) shows a type IV isotherm with a H_3-type hysteresis loop ($P/P_o > 0.4$) which indicates the presence of mesopores in the active double hydroxide material[17,47] with a specific surface area (SSA) of 90.36 $m^2\ g^{-1}$. This value is comparable to or even larger than those reported in earlier studies for NiAl-double hydroxide materials published elsewhere.[17,29,48] Fig. 5(b) shows the corresponding pore size distribution with a major pore diameter ranging from 1.7 to 4 nm which shows the successful inclusion of both microporous and mesoporous sites. The micropores (diameter <2 nm) present serve as the ion traps for energy storage, while the mesopores are used as pathways for transport of ions necessary for power delivery.[2,49]

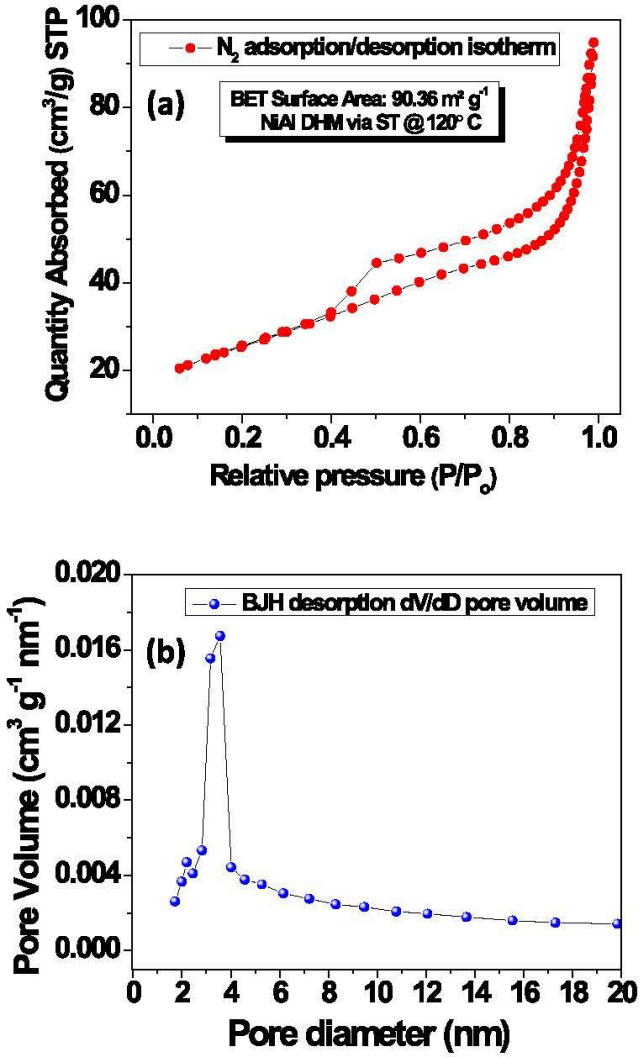

FIG. 5. (a) N_2-adsorption/desorption isotherms for NiAl DHMs; (b) the pore size distribution of the NiAl DHMs.

B. Electrochemical Performance

Cyclic voltammetry (CV) measurements are used to understand the macroscopic electrochemical surface reactions at the electrode material during operation. Fig. 6(a) shows the CV curves for a bare NF current collector, NF-G current collector, and NiAl DHMs coated onto NF (NiAl-DHM/NF) and NiAl DHM on NF-G (NiAl-DHM/NF-G) current collectors at a scan rate of 20 mV s^{-1}. The CV plots are characterized by symmetrical characteristic profiles that are well defined by cathodic (reduction reaction) and anodic (oxidation reaction) peaks.[30] This reveals that the electrode reaction corresponds to a quasi-reversible process, indicating that the measured capacitance in these materials is mainly based on the redox mechanism due to the pseudocapacitive behavior of the material.[50] It can be clearly seen that the integral area of the CV graph of NiAl DHM/NF-G curve is the largest among the three electrode materials presented, implying that it possesses the highest specific capacitance. This improvement in pseudocapacitance could be due to the contribution of

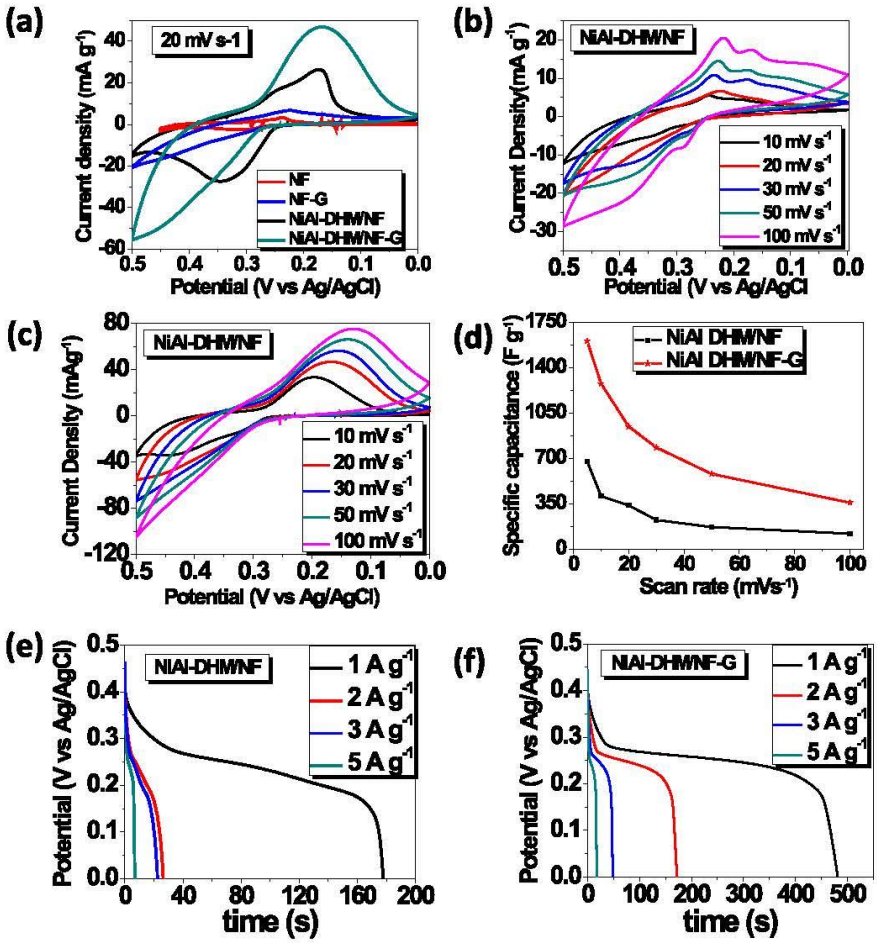

FIG. 6. (a) Cyclic voltammetry of NF, NF-G, NiAl DHM on NF and NF-G at a scan rate of 20 mV s^{-1}; cyclic voltammetry of NiAl DHM at different scan rates on (b) NF and (c) NF-G; (d) specific capacitance of NiAl DHM on NF and NF-G versus scan rates; (e) galvanostatic charge–discharge measured at different current densities for NiAl DHM on NF; (f) galvanostatic charge–discharge measured at different current densities for NiAl DHM on NF-G.

more electronegative species existing within the interlayer region of the LDH structure,[14,15] together with the high conductivity of the graphene on nickel foam.

Fig. 6(b) shows the CV plot for NiAl DHM/NF current collector at a scan rate ranging from 5 to 100 mV s^{-1} with redox peaks that undergo small shifts towards the negative potential with increasing scan rate. The first sets of peaks at 0.36 V and 0.23 V are related to the cathodic and anodic peaks of the NF current collector material at a scan rate of 30 mV s^{-1}. The second set of redox peaks shows symmetrical CV plots with well-defined redox peaks which occur at 0.28 V and 0.17 V respectively at the same scan rate. These peaks are related to the pseudocapacitive nature of NiAl DHM and the strong redox peaks correspond to the following redox reactions where Ni undergoes a transition between different oxidation states:[14]

$$Ni(OH)_2 + OH^- \leftrightarrow NiOOH + H_2O + e^- \quad (1)$$

Fig. 6(c) shows the CV plots of the NiAl DHM/NF-G with the cathodic and anodic peaks observed to occur at around 0.40 V and 0.15 V respectively at a scan rate of 30 mV s^{-1}. The peaks ascribed to

the NF current collector are not seen for NiAl DHM/NF-G; this could be assumed to be due to the complete coverage of NF by graphene thus confirming an effective coating of the NF surface with the graphene layer. The successful growth of a thin layer of graphene on the NF could be further confirmed from the current response value recorded from the CV plots when compared with those where NF current collector was used (Fig. 6(b)).

Using equation (2) below, the specific capacitance can be calculated from the CV:[17,51]

$$C_s\left(\frac{\mathrm{F}}{\mathrm{g}}\right) = \frac{\bar{A}}{m\Delta V f} \tag{2}$$

where $\bar{A}$ is the integrated area under the curve for the cathodic current of the CV curve (in mA-V); m is the mass of the coated active material (in g); and f is the scan rate (in mV/s) used during the CV measurement. The specific capacitance calculated from the CV measurements is 409 F g^{-1} for NiAl DHM/NF; this increases to 1276 F g^{-1} when NF-G is used as current collector, both at a scan rate of 10 mV s^{-1}. The higher specific capacitance calculated for NiAl coated on NF-G may be due to the presence of the graphene layer deposited on the surface of the NF. This layer provides the higher conductivity required for fast ion transport at the electrolyte/electrode surface.

Fig. 6(d) shows the variation of the specific capacitance values with increasing scan rate; a decrease in specific capacitance is observed at a higher scan rate. Indeed, at a low scan rate, most of the electrode's active surface area is in good contact with the ions contained in the electrolyte, allowing complete interactions between them. However, at a higher scan rate, the effective interaction is greatly reduced, leading to lower observed specific capacitance values. Also at higher scan rates, the movement of ions is limited by the diffusion, and only outer active surfaces are used for charge storage, leading to lower specific capacitance values.[52]

The galvanostatic discharge plots for NiAl DHM/NF and NiAl DHM/NF-G are shown in Figs. 6(e) and 6(f) at current densities of 1, 2, 3 and 5 A g^{-1} respectively. An enhancement in the discharge time for the NiAl DHM/NF-G composite electrode at 1 A g^{-1} current density is observed in Fig. 6(f) as compared with that of NiAl DHM/NF (Fig. 6(e)). The specific capacitance was also calculated from the galvanostatic discharge curves using the formula:[14,17]

$$C_S\,(\mathrm{F/g}) = \frac{IT_\mathrm{d}}{m\Delta \mathrm{V}} \tag{3}$$

where I is a current (A), T_d is the discharge time (s), m is the mass of active material (g), and ΔV is the voltage range (V).

A specific capacitance of 1252 F g^{-1} is obtained for NiAl DHM/NF-G compared with a value of 354 F g^{-1} for NiAl DHM/NF at a current density of 1 A g^{-1}. This is an enhancement of 3.5 times for the NF-G current collector and is a great improvement over similar studies on NiAl DHM prepared by a solvothermal technique reported elsewhere.[29] We therefore propose that the improvement in supercapacitance value is a result of the addition of a graphene layer to form the NF-G current collector which provides an improved electron transfer rate and better structural support for the DHM material[26,30] and could also ensure the retention of the capacitance even after long cycling.

The stability of the electrode material of supercapacitors is also a very important characteristic for their application as energy storage devices. Figs 7(a) and 7(b) show the continuous cycling in galvanostatic charge–discharge and the associated capacitance retention of NiAl-DHM on both NF and NF-G current collectors, respectively, within a potential window of 0 – 0.5 V at a 30 A g^{-1} current density for 1000 cycles. The stability plot was characterized by little change in the specific capacitance obtained from repeated charging and discharging, which initially increased after 200 cycles before stabilizing at a higher number of cycles for both cases. This observation is unique to LDH-based materials and has also been previously reported in earlier studies.[17,42] It is suggested that this increase is as a result of the full exposure of some inner sites of the DHM material which were not exposed during the initial cycling stage, and due to the activation of NiAl LDH sites which contribute to an increase in capacitance after some initial cycling of the active electrode material.[17,42] The capacitive retention stabilizes to a value of 97.9% for NiAl DHM on NF-G and to a slightly lower value of 95.7% for NiAl DHM on NF after 700 cycles. This is also an improvement over

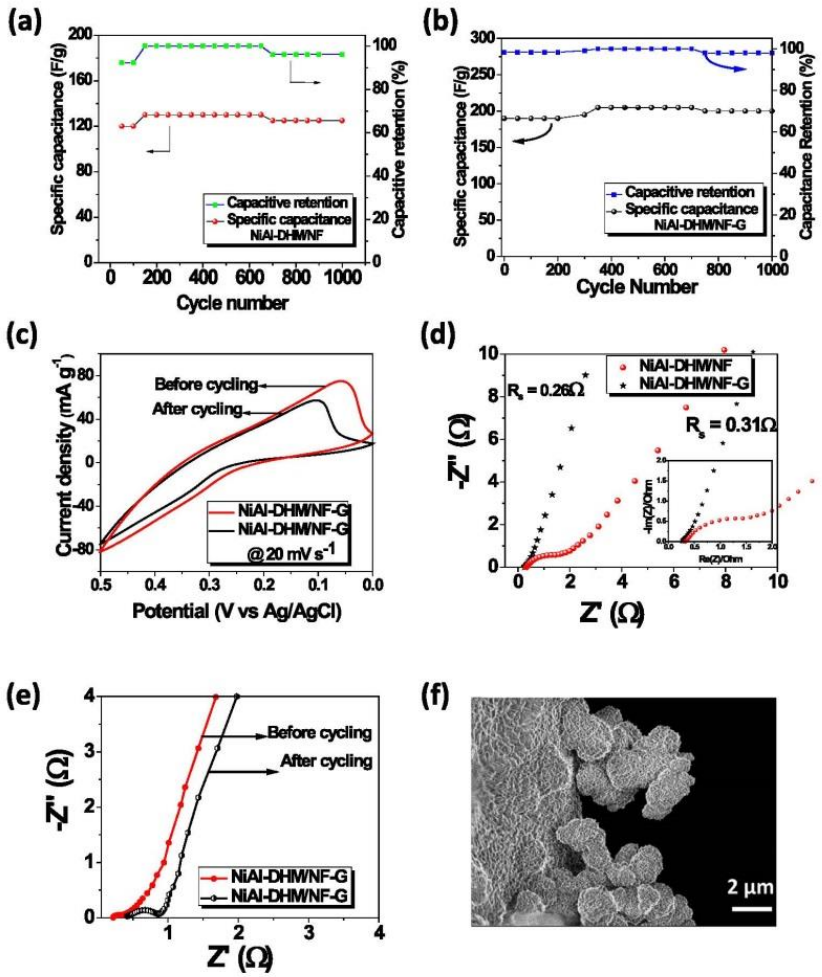

FIG. 7. Dependence of the cycling discharge specific capacitance and capacitive retention on the charge–discharge cycle numbers for NiAl DHM on (a) NF and (b) NF-G respectively at a current density of 30 A g^{-1}; (c) CV comparison of NiAl DHM on NF-G before and after cycling at a scan rate of 20 mV s^{-1}; (d) EIS of NiAl DHM on NF and NF-G current collector at a potential of 0.2 V; (e) EIS comparison of NiAl DHM on NF-G before and after cycling at a potential of 0.2 V; (f) SEM image for comparison of NiAl DHM on NF-G before and after cycling.

similar reports[29] for NiAl DHM prepared using a solvothermal technique where a solvent was used to direct the growth of the double layer hydroxides. Although a longer cycling time was adopted here as compared with that adopted by Song *et al.*,[29] an improvement from 95% to 97.5% was still observed for the capacitive retention. Since redox reactions also take place during the continuous cycling charge–discharge process, a comparison was made for the CV curves before and after cycling to further analyze the cyclic stability of the electrode material (i.e. NiAl DHM/NF-G in Fig. 7(c)). Similar CV curves were obtained (Fig. 7(c)) before and after the 1000th cycle; in other words, both CV curves appear with their usual redox peaks which confirm the stability of the NiAl DHM material. However, a slight reduction in the intensity and shift of the anodic peak positions towards

the positive potential is observed. This is caused by consumption of some of the active sites in the material which leads to some subsequent capacitance loss.[44]

Fig. 7(d) shows the Nyquist plots from the EIS test done at open circuit (E_{oc}) potential to further evaluate the electrochemical behavior for the NiAl DHM on NF and NF-G. The frequency range used for the measurement was from 10 mHz to 100 kHz. At high frequency, a partial semi-circular arc is formed which is attributed to the dispersion effect.[44] At low frequency, the impedance plot should, theoretically, be a vertical line parallel to the vertical -Im (Z) axis. This vertical line indicates a pure capacitive behavior of the DHMs and low diffusion resistance of ions within the structure of the material.[17] The electrode series resistance of the active material on both NF and NF-G was deduced from the intercept on the real Z-axis, while the charge transfer resistance (R_{ct}) was obtained based on the semi-circular arc radius.[44] The electrode series resistance value from the Nyquist plots improves from 0.31 Ω for NiAl DHM/NF to 0.26 Ω for NiAl DHM/NF-G due to the presence of a graphene layer on the NF current collector. From the inset to Fig. 7(d), the radius of the semi-circular arc is related to the resistance of the charge transfer process. This radius is also observed to be smaller for the NiAl DHM on NF-G when the partial semi-circular arc is extrapolated to a complete a semi-circle. These enhancements could be attributed to the better conductivity and favorable electron transfer rate when the NF-G current collector was used. A similar explanation for this occurrence was reported in an earlier study where GF grown by CVD was used as an electrode material.[27]

Fig. 7(e) shows the Nyquist plots for the NiAl DHM on NF-G before and after the last cycle. Both plots were characterized by semi-circular arcs with intercepts on the Z'–axis and an increase in the radius of the semi-circle after cycling is observed, which could be ascribed to a slight increase in the internal resistance. In principle, an increase in the internal resistance could be linked to the capacitance loss described earlier when referring to the decrease in intensity of the CV peaks. The morphological characterization of the electrode after cycling tests was done to conclude analysis on stability. The SEM image of the electrode showed the retention of the microspherical nature of the NiAl double hydroxides (Fig. 7(f)). Thus, these results show the suitable use of the electrode for full device supercapacitor applications.

IV. CONCLUSION

Using a facile solvothermal technique that is environmentally friendly, nickel-aluminum double hydroxide microspheres (NiAl DHMs) have been successfully prepared in a tertbutanol-water (TBA-H_2O) medium as a suitable electrode material for pseudocapacitor devices. This study demonstrated the unique morphology of the NiAl DHMs with relatively thin flakes grown on microspheres, as seen from the scanning and tunneling electron microscopy results. The addition of graphene to the surface of the pristine nickel foam (NF) current collector retains the spherical morphology, while greatly enhancing the electrochemical performance, electrical characteristics and stability of the DHMs. Overall, the simple strategy adopted to synthesize NiAl DHM structures and coat them on nickel foam graphene (NF-G) templates to fabricate electrodes with superior electrochemical properties makes NiAl DHMs a good and promising material for application in hybrid electrochemical capacitors.

ACKNOWLEDGMENTS

This work is based on research supported by the South African Research Chairs Initiative (SARChI) of the South African Department of Science and Technology (DST) and the National Research Foundation (NRF). Any opinion, findings and conclusions or recommendations expressed in this work are those of the authors and the NRF and DST do not accept any liability with regard thereto. A.T.C.J acknowledges support from the LRSM, through the U.S. National Science Foundation MRSEC, Grant No. DMR-1120901. D M acknowledges the financial support from the University of Pretoria and the NRF Doctorate Innovation Fund for his study. The authors will also like to acknowledge the invaluable discussions and inputs from Prof. Yury Gogotsi.

[1] B. Conway, J. Electrochem. Soc. **138**, 1539 (1991).
[2] C. Liu, F. Li, L.-P. Ma, and H.-M. Cheng, Adv. Mater. **22**, E28 (2010).
[3] A. Burke, J. Power Sources **91**, 37 (2000).
[4] P. Simon and Y. Gogotsi, Nat. Mater. **7**, 845 (2008).
[5] A. Bello, O. O. Fashedemi, J. N. Lekitima, M. Fabiane, D. Dodoo-Arhin, K. I. Ozoemena, Y. Gogotsi, A. T. Charlie Johnson, and N. Manyala, AIP Adv. **3**, 082118 (2013).
[6] G. Yu, L. Hu, M. Vosgueritchian, H. Wang, X. Xie, J. R. McDonough, X. Cui, Y. Cui, and Z. Bao, Nano Lett. **11**, 2905 (2011).
[7] D. Liu, X. Wang, X. Wang, W. Tian, J. Liu, C. Zhi, D. He, Y. Bando, and D. Golberg, J. Mater. Chem. A **1**, 1952 (2013).
[8] A. Bello, K. Makgopa, M. Fabiane, D. Dodoo-Ahrin, K. I. Ozoemena, and N. Manyala, J. Mater. Sci. **40**, 6707 (2013).
[9] D.-W. Wang, F. Li, and H.-M. Cheng, J. Power Sources **185**, 1563 (2008).
[10] C. Zhao, W. Zheng, X. Wang, H. Zhang, X. Cui, and H. Wang, Sci. Rep. **3**, 2986 (2013).
[11] G. Chen, S. S. Liaw, B. Li, Y. Xu, M. Dunwell, S. Deng, H. Fan, and H. Luo, J. Power Sources **251**, 338 (2014).
[12] H. Wang, H. S. Casalongue, Y. Liang, and H. Dai, J. Am. Chem. Soc. **132**, 7472 (2010).
[13] H. B. Li, M. H. Yu, F. X. Wang, P. Liu, Y. Liang, J. Xiao, C. X. Wang, Y. X. Tong, and G. W. Yang, Nat. Commun. **4**, 1894 (2013).
[14] J. Wang, Y. Song, Z. Li, Q. Liu, J. Zhou, X. Jing, M. Zhang, and Z. Jiang, Energy & Fuels **24**, 6463 (2010).
[15] L. Wang, D. Wang, X. Y. Dong, Z. J. Zhang, X. F. Pei, X. J. Chen, B. Chen, and J. Jin, Chem. Commun. (Camb). **47**, 3556 (2011).
[16] X. Dong, L. Wang, D. Wang, C. Li, and J. Jin, Langmuir **28**, 293 (2012).
[17] W. Yang, Z. Gao, J. Wang, J. Ma, M. Zhang, and L. Liu, ACS Appl. Mater. Interfaces **5**, 5443 (2013).
[18] S. Huang, G.-N. Zhu, C. Zhang, W. W. Tjiu, Y.-Y. Xia, and T. Liu, ACS Appl. Mater. Interfaces **4**, 2242 (2012).
[19] Z. Gao, J. Wang, Z. Li, W. Yang, and B. Wang, Chem. Mater. **23**, 3509 (2011).
[20] Z. Lu, W. Zhu, X. Lei, G. R. Williams, D. O'Hare, Z. Chang, X. Sun, and X. Duan, Nanoscale **4**, 3640 (2012).
[21] L. Zhang, X. Zhang, L. Shen, B. Gao, L. Hao, X. Lu, F. Zhang, B. Ding, and C. Yuan, J. Power Sources **199**, 395 (2012).
[22] J. Yang, C. Yu, X. Fan, Z. Ling, J. Qiu, and Y. Gogotsi, J. Mater. Chem. A **1**, 1963 (2013).
[23] Q. Wang and D. O'Hare, Chem. Rev. **112**, 4124 (2012).
[24] X.-M. Liu, Y.-H. Zhang, X.-G. Zhang, and S.-Y. Fu, Electrochim. Acta **49**, 3137 (2004).
[25] M. T. Pettes, H. Ji, R. S. Ruoff, and L. Shi, Nano Lett. **12**, 2959 (2012).
[26] S. Khamlich, A. Bello, M. Fabiane, B. D. Ngom, and N. Manyala, J. Solid State Electrochem. **17**, 2879 (2013).
[27] X.-C. Dong, H. Xu, X.-W. Wang, Y.-X. Huang, M. B. Chan-Park, H. Zhang, L.-H. Wang, W. Huang, and P. Chen, ACS Nano **6**, 3206 (2012).
[28] U. M. Patil, J. S. Sohn, S. B. Kulkarni, S. C. Lee, H. G. Park, K. V. Gurav, J. H. Kim, and S. C. Jun, ACS Appl. Mater. Interfaces **6**, 2450 (2014).
[29] Y. Song, J. Wang, Z. Li, D. Guan, T. Mann, Q. Liu, M. Zhang, and L. Liu, Microporous Mesoporous Mater. **148**, 159 (2012).
[30] Y. Tao, L. Ruiyi, L. Zaijun, L. Junkang, W. Guangli, and G. Zhiquo, RSC Adv. **3**, 19416 (2013).
[31] G. Hu and D. O'Hare, J. Am. Chem. Soc. **127**, 17808 (2005).
[32] C. Burda, X. Chen, R. Narayanan, and M. A. El-Sayed, Chem. Rev. **105**, 1025 (2005).
[33] L.-S. Zhong, J.-S. Hu, H.-P. Liang, A.-M. Cao, W.-G. Song, and L.-J. Wan, Adv. Mater. **18**, 2426 (2006).
[34] L. Xu, Y. Ding, C. Chen, L. Zhao, C. Rimkus, R. Joesten, and S. L. Suib, 308 (2008).
[35] S. J. Chae, F. Güneş, K. K. Kim, E. S. Kim, G. H. Han, S. M. Kim, H.-J. Shin, S.-M. Yoon, J.-Y. Choi, M. H. Park, C. W. Yang, D. Pribat, and Y. H. Lee, Adv. Mater. **21**, 2328 (2009).
[36] W. L. Bragg, in *Proc. Camb. Philol. Soc.* (1913), pp. 43–57.
[37] G. Brindley and S. Kikkawa, Thermochim. Acta **2**, 385 (1978).
[38] J. Olanrewaju, B. Newalkar, C. Mancino, and S. Komarneni, Mater. Lett. 307 (2000).
[39] E. Kanezaki, K. Kinugawa, and Y. Ishikawa, Chem. Phys. Lett. **226**, 325 (1994).
[40] S. Velu, V. Ramkumar, A. Narayanan, and C. Swamy, J. Mater. Sci. **32**, 957 (1997).
[41] A. Bello, O. O. Fashedemi, M. Fabiane, J. N. Lekitima, K. I. Ozoemena, and N. Manyala, Electrochim. Acta **114**, 48 (2013).
[42] L. Zhang, J. Wang, J. Zhu, X. Zhang, K. San Hui, and K. N. Hui, J. Mater. Chem. A **1**, 9046 (2013).
[43] H. Saikia, N. Sarmah, and J. N. Ganguli, Bull. Catal. Soc. India **11**, 1 (2012).
[44] B. Wang, Q. Liu, Z. Qian, X. Zhang, J. Wang, Z. Li, H. Yan, Z. Gao, F. Zhao, and L. Liu, J. Power Sources **246**, 747 (2014).
[45] G. Wang, J. Yang, J. Park, X. Gou, B. Wang, H. Liu, and J. Yao, J. Phys. Chem. C **112**, 8192 (2008).
[46] A. C. Ferrari and J. Robertson, Phys. Rev. B **61**, 14095 (2000).
[47] J. Yu, J. C. Yu, W. Ho, M. K.-P. Leung, B. Cheng, G. Zhang, and X. Zhao, Appl. Catal. A Gen. **255**, 309 (2003).
[48] Z. Wang, X. Zhang, J. Wang, L. Zou, Z. Liu, and Z. Hao, J. Colloid Interface Sci. **396**, 251 (2013).
[49] M. Zhi, C. Xiang, J. Li, M. Li, and N. Wu, Nanoscale **5**, 72 (2013).
[50] H. KuanXin, Z. Xiaogang, and L. Juan, Electrochim. Acta **51**, 1289 (2006).
[51] V. Khomenko, E. Frackowiak, and F. Béguin, Electrochim. Acta **50**, 2499 (2005).
[52] Z. J. Lao, K. Konstantinov, Y. Tournaire, S. H. Ng, G. X. Wang, and H. K. Liu, J. Power Sources **162**, 1451 (2006).

4.1.4 Concluding Remarks

In summary, the synthesis of NiAl layered double hydroxide and NiAl double hydroxide microspheres have been successfully carried out using a facile environmentally friendly technique involving different solvents to tune their morphological properties. The surface morphology of both samples was extensively studied using scanning and transmission electron microscopes. The results obtained show the existence of nanosheets interlinked with each other to form a continuous interconnected framework.

The dehydroxylation of the layered sheets in temperature ranges of 200 – 600 °C was also recorded from thermal stability tests done in nitrogen gas. This is in agreement with earlier reports done by researchers on NiAl double hydroxide materials.

The incorporation of a thin-film of few layer graphene on the polycrystalline nickel foam surface used as a current collector shows a significant improvement in the electrochemical performance and stability of the NiAl DHM active material when adopted as redox capacitor electrodes.

4.1.5 References

[1] L. Zhang, X. Zhang, L. Shen, B. Gao, L. Hao, X. Lu, F. Zhang, B. Ding, C. Yuan, J. Power Sources 199 (2012) 395.

[2] W. Yang, Z. Gao, J. Wang, J. Ma, M. Zhang, L. Liu, ACS Appl. Mater. Interfaces 5 (2013) 5443.

[3] Y. Tao, L. Ruiyi, L. Zaijun, L. Junkang, W. Guangli, G. Zhiquo, RSC Adv. 3 (2013) 19416.

[4] M. Shao, F. Ning, Y. Zhao, J. Zhao, M. Wei, D.G. Evans, X. Duan, Chem. Mater. 24 (2012) 1192.

[5] Q. Wang, D. O'Hare, Chem. Rev. 112 (2012) 4124.

[6] L.-H. Su, X.-G. Zhang, Y. Liu, J. Solid State Electrochem. 12 (2007) 1129.

[7] X.-M. Liu, Y.-H. Zhang, X.-G. Zhang, S.-Y. Fu, Electrochim. Acta 49 (2004) 3137.

[8] S. Huang, G.-N. Zhu, C. Zhang, W.W. Tjiu, Y.-Y. Xia, T. Liu, ACS Appl. Mater. Interfaces 4 (2012) 2242.

[9] S.C. Jun, U.M. Patil, S.C. Lee, S.B. Kulkarni, J.S. Sohn, M.S. Nam, S. Han, Nanoscale (2015).

[10] U.M. Patil, J.S. Sohn, S.B. Kulkarni, S.C. Lee, H.G. Park, K. V Gurav, J.H. Kim, S.C. Jun, ACS Appl. Mater. Interfaces 6 (2014) 2450.

[11] S. Dong, A.Q. Dao, B. Zheng, Z. Tan, C. Fu, H. Liu, F. Xiao, Electrochim. Acta 152 (2015) 195.

[12] N.A. Jarrah, F. Li, J.G. van Ommen, L. Lefferts, J. Mater. Chem. 15 (2005) 1946.

[13] S.J. Chae, F. Güneş, K.K. Kim, E.S. Kim, G.H. Han, S.M. Kim, H.-J. Shin, S.-M. Yoon, J.-Y. Choi, M.H. Park, C.W. Yang, D. Pribat, Y.H. Lee, Adv. Mater. 21 (2009) 2328.

[14] G. Wang, J. Yang, J. Park, X. Gou, B. Wang, H. Liu, J. Yao, J. Phys. Chem. C 112 (2008) 8192.

[15] A.C. Ferrari, J. Robertson, Phys. Rev. B 61 (2000) 14095.

[16] Z. Gao, J. Wang, Z. Li, W. Yang, B. Wang, Chem. Mater. 23 (2011) 3509.

[17] J. Yu, J.C. Yu, W. Ho, M.K.-P. Leung, B. Cheng, G. Zhang, X. Zhao, Appl. Catal. A Gen. 255 (2003) 309.

[18] Z. Wang, X. Zhang, J. Wang, L. Zou, Z. Liu, Z. Hao, J. Colloid Interface Sci. 396 (2013) 251.

[19] Q. Liu, G. Fan, S. Zhang, Y. Liu, F. Li, Mater. Lett. 82 (2012) 4.

[20] H. Wang, G. Fan, C. Zheng, X. Xiang, F. Li, Ind. Eng. Chem. Res. 49 (2010) 2759.

4.2 Enhancement of the electrochemical properties of P3HT:PCBM polymer-blend electrodes using NiAl layered double hydroxide-graphene composites

4.2.1 Introduction

Conducting polymers (CP) and their associated blends are characterized with an interpenetrating matrix of donor and acceptor materials which provides excellent electrical properties for numerous device applications. They have recently been applied as supercapacitor electrodes due to their promising redox capacitive capabilities. Among these polymers, the most common conductive polymers used for supercapacitor applications include polyaniline (PANI) [1], poly (3-hexylthiophene) (P3HT) [2] and P3HT-polymer with fullerene acceptor material, [6, 6]-phenyl C61-butyric acid methyl ester (PCBM), to form a hybrid blend of P3HT:PCBM nanostructures [3] with efficient donor-acceptor charge carriers. However, the hydrophobic nature of the CPs [2] as well as the limited access of the electrolyte ions to the material surface which plagues them with low specific capacitance values, are still some of the problems associated with polymer-based supercapacitors [3,4]. This issue could be addressed by initially incorporating a high surface area material into the main polymer matrix in a bid to improve the overall electrochemical performance of the polymer.

Composite materials containing conjugated polymer blends with carbonaceous materials or other highly pseudoactive materials have gained much attention due to the ease in synergizing their individual properties. Recent reports involve a direct mixing of

individual materials synthesized separately to form the composite material [5,6]. Layered double hydroxides-graphene foam (LDH-GF) composites are seen to be an attractive choice for incorporation into the polymer blend due to the existence of both redox capacitive properties coupled with an enhanced electric double layer contribution from the higher surface area graphene.

In this study, the P3HT:PCBM blend was mixed with NiAl LDH-GF material and rigorously stirred in the dark for several hours to obtain a P3HT:PCBM/NiAl LDH-GF paste. The polymer blend was obtained by mixing weighed portions of regioregular P3HT conjugated polymer and PCBM fullerene in a ratio of 1:0.8 in chlorobenzene solvent while the NiAl-LDH-GF material was obtained via an exfoliation-assisted solvothermal technique described in section 3.2.2. Thereafter, a facile dip coating technique was adopted in coating the active material onto pre-cleaned NF substrate to obtain the final composite electrode. No previous report has been established so far on this type of polymer composite electrode and the novel results obtained, show a significant increase in the areal specific capacitance (C_s, F cm^{-2}) of the composite electrode by an order of magnitude as compared to that of the pristine P3HT:PCBM electrode.

The results obtained from the analyses using different characterization techniques will now be discussed in detail.

4.2.2 Result and discussion

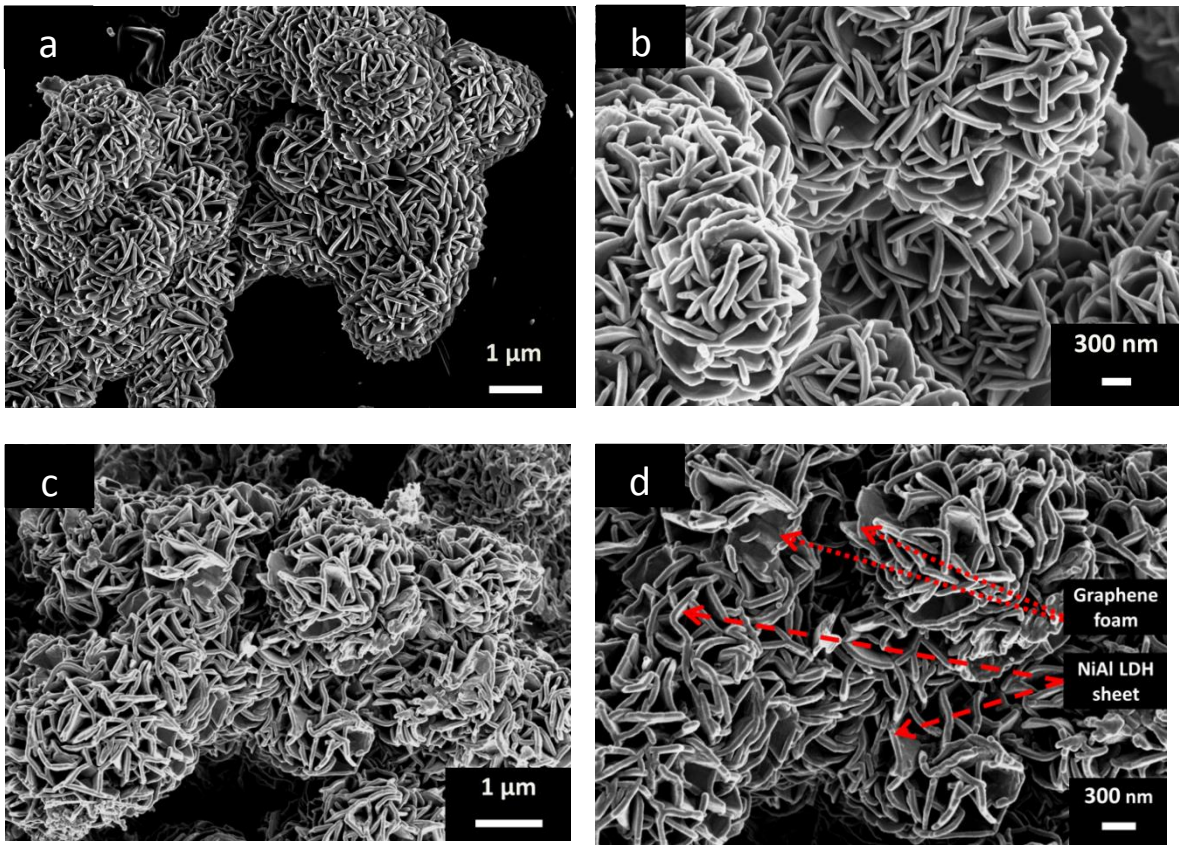

Figure 4.10: SEM micrograph of (a,b) NiAl LDH (c,d) NiAl LDH-GF composite

Figure 4.10 (a-d) displays the morphology of the NiAl LDH and NiAl LDH-GF composite at low and high magnifications. In figure 4.10(c & d), a successful interlacing of the LDH sheets with the graphene foam is obvious. The presence of flakes of graphene foam (GF) is visible from the SEM images shown in figure 4.10(d) at high magnification with the red dotted arrows used to distinguish the much thinner graphene foam flakes from the much thicker NiAl LDH sheets. This is confirmed from the Raman spectra (Figure 4.11) obtained for both samples in which the characteristic vibrational band typical of NiAl LDH is recorded at a wave number of approximately 1025 cm^{-1} similar to reports

involving graphene nanosheet/NiAl LDH composites [7]. The second spectrum for the NiAl LDH-GF also shows the LDH peak in addition to the G-band and 2D-bands associated with graphene vibrational modes. As stated in section 4.1.2, the G-band is related to the first-order bond stretching while the 2D peak is linked to the second-order two-phonon process of opposite momentum [8,9].

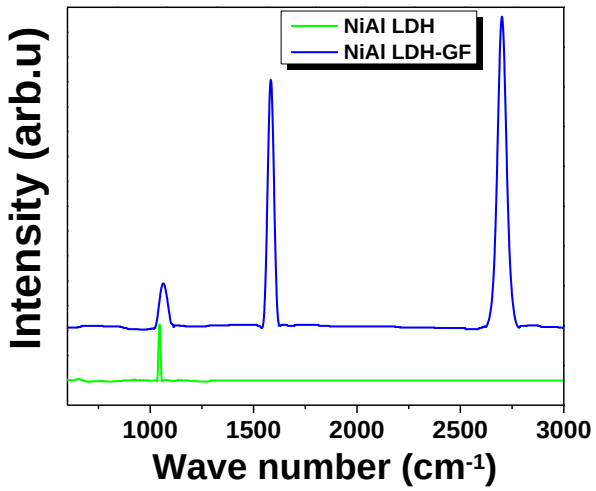

Figure 4.11: Raman spectra of NiAl LDH and NiAl LDH-GF composite

The Raman spectra for the NiAl LDH, NiAl-LDH-GF composite, P3HT:PCBM blend, and the P3HT:PCBM/NiAl-LDH-GF composite is shown in figure 4.12. A peak shift is observed for some of the Raman modes due to the interaction between the different material components in the P3HT:PCBM/NiAl-LDH-GF composite. For example, the LDH peak is shifted from 1025 cm^{-1} in its pristine state to 1059 cm^{-1} in the NiAl LDH-GF composite. This is accompanied by a reduction in the intensity of those peaks and such observations have been described to be due to the coexistence of the different materials of the

composite which disrupts the initial order of the P3HT:PCBM polymer matrix [10]. Other vibrational modes observed include the peak at ~1,365 cm^{-1} and the shoulder peak appearing at ~1,445 cm^{-1} which are both related to the vibrational modes from the C–C intra-ring and the symmetric C=C stretching modes in the P3HT:PCBM blend respectively [10–12]. They are usually described as "in-plane ring skeleton modes" which quantify the degree of molecular order of the P3HT phase in the blend due to the fact that they are sensitive to π-electron delocalization of P3HT molecules. The vibrational mode for fullerene-derived PCBM films usually appears at 1,469 cm^{-1}, based on earlier literature, and can be assigned to the dominant pentagonal-pinch mode $A_g(2)$ of C_{60} [13].

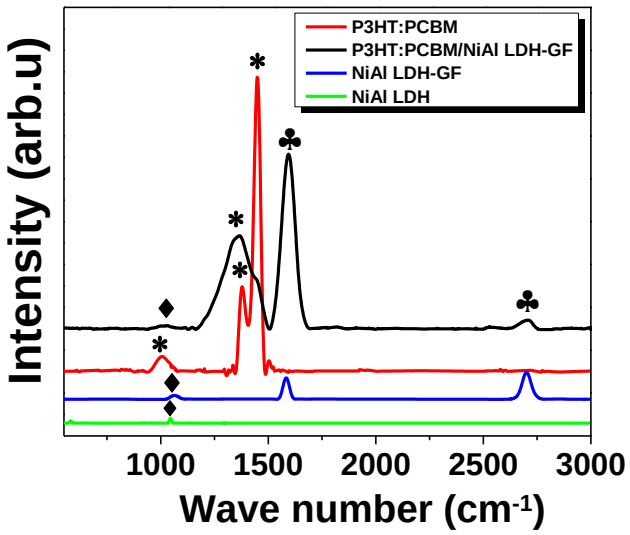

Figure 4.12: Raman spectra of NiAl-LDH (green spectrum), NiAl LDH-GF (blue spectrum in figure inset), P3HT:PCBM (red spectrum), and P3HT:PCBM/NiAl-LDH-GF (black spectrum), respectively (note: Diamond symbol denotes LDH peak, asterisk symbol denotes P3HT:PCBM peaks, and club symbol denotes graphene peaks)

An excellent improvement in the electrochemical behavior of the composite electrode is reported and is suggested to be due to the addition of a higher surface area NiAl LDH-GF material to the polymer blend. This improvement is attributed to the creation of active mesopores within the composite material necessary for efficient charge storage. The presence of suitable mesopores in the electrode material is also vital in order to ensure the mass transfer reduction of electrolyte during fast redox reactions [14]. The BET surface area results for the pristine P3HT:PCBM polymer blend and the P3HT:PCBM/NiAl-LDH-GF composite are displayed in figure 4.13 with the physical adsorption/desorption isotherms. The specific surface area (SSA) of the P3HT:PCBM/NiAl-LDH-GF composite is drastically increased to 22.33 m^2 g^{-1} from an initial value of 2.58 m^2 g^{-1} for the P3HT:PCBM polymer blend alone due to the addition of . NiAl LDH-GF material to the polymer blend

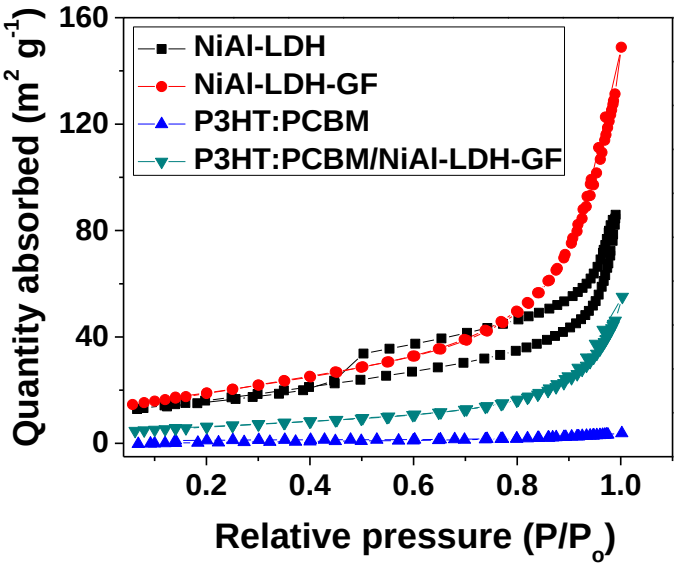

Figure 4.13: N_2 adsorption–desorption isotherms for NiAl-LDH, NiAl-LDH-GF, P3HT:PCBM and P3HT:PCBM/NiAl-LDH-GF samples

Figure 4.14 shows the pore size distribution for the P3HT:PCBM polymer blend and the P3HT:PCBM/NiAl-LDH-GF composite sample. It is observed from the figure that the composite has a higher volume of mesopores which is typically within the mesopore size diameter range of 2 – 5 nm thus confirming the successful inclusion of more mesoporous sites necessary for charge storage.

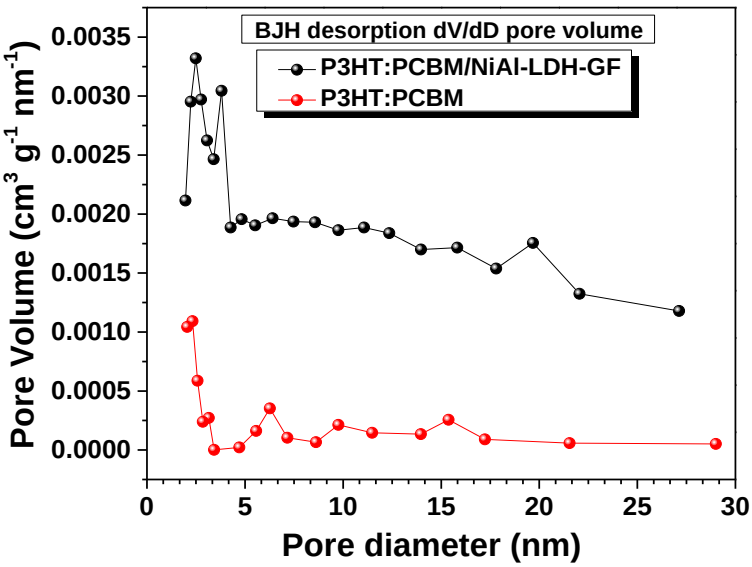

Figure 4.14: Pore size distribution of the P3HT:PCBM and P3HT:PCBM/NiAl-LDH-GF composite

An in-depth summary on the complete analysis of the enhancement of the polymer blend with NiAl LDH-GF is presented in the following attached publication entitled; "P3HT:PCBM/nickel-aluminum layered double hydroxide-graphene foam composites for supercapacitor electrodes."

4.2.3 Publication 2: P3HT:PCBM/nickel-aluminum layered double hydroxide-graphene foam composites for supercapacitor electrodes.

J Solid State Electrochem (2015) 19:445–452
DOI 10.1007/s10008-014-2602-0

ORIGINAL PAPER

P3HT:PCBM/nickel-aluminum layered double hydroxide-graphene foam composites for supercapacitor electrodes

Damilola Momodu · Abdulhakeem Bello · Julien Dangbegnon · Farshad Barzeger · Mopeli Fabiane · Ncholu Manyala

Received: 12 April 2014 / Revised: 26 July 2014 / Accepted: 1 August 2014 / Published online: 31 August 2014

Abstract In this paper, a simple dip-coating technique is used to deposit a poly (3-hexylthiophene) and [6, 6]-phenyl C_{61}-butyric acid methyl ester (P3HT:PCBM)/nickel–aluminum-layered double hydroxide-graphene foam (NiAl-LDH-GF) composite onto a nickel foam (NF) serving as a current collector. A self-organization of the polymer chains is assumed on the Ni-foam grid network during the slow "dark" drying process in normal air. Electrochemical cyclic voltammetry (CV) and constant charge–discharge (CD) measurements show an improvement in the supercapacitive behavior of the pristine P3HT:PCBM by an order of magnitude from 0.29 F cm^{-2} (P3HT:PCBM nanostructures) to 1.22 F cm^{-2} (P3HT:PCBM/NiAl-LDH-GF composite structure) resulting from the addition of NiAl-LDH-GF material at a current density of 2 mA cm^{-2}. This capacitance retention after cycling at 10 mA cm^{-2} also demonstrates the electrode material's potential for supercapacitor applications.

Keywords Dip coating, P3HT:PCBM · Graphene foam · Nickel–aluminum-layered double hydroxide (NiAl-LDH) · Supercapacitor

Introduction

The rising energy demand for the future generation is one of the major concerns of most countries around the world today. The increasing cost of energy and the issues related to environmental pollution which are associated with energy production and use compel the search for alternative sources of energy that are renewable, sustainable, clean, and efficient. This has stimulated intense research into new methods for energy generation and efficient storage. In order to provide a sustainable and continuous supply of energy to meet the ever-increasing demand, there is a need to set up storage systems that will store excess energy produced by different energy-generation methods.

Supercapacitors (SCs, or ultracapacitors) and hybrid solid-state batteries are but a few examples of the most recent technological innovations in the field of electrical energy storage [1–9]. Among the latter, SCs possess higher power density and longer cycle life but lower energy density. Therefore, one of the main aims in the ongoing research into SCs is to improve their energy densities considerably, to bring the densities close to those of batteries or even better [2]. For efficient energy storage, the performance of SCs should easily meet technological requirements in present and future applications. Some important factors that determine the performance of SCs include the nature of the electrode and the operating voltage. The storage mechanism is used to classify SCs into two main types: the electric double-layer capacitors (EDLCs), in which the charge is stored at the electrode/electrolyte interface with the main material used being carbon, and the pseudocapacitors in which the charge arises from reversible redox reactions in materials like conducting polymers, metal oxides or hydroxides, etc. [2, 4]. The electrode porous structure and material surface area are very important for optimum capacitance due to the surface phenomena associated with supercapacitors [4].

Graphene, planar sheet of sp^2 bonded carbon atoms densely packed in a honeycomb lattice, has recently attracted much attention from scientific communities due to its unique properties such as high electrical conductivity, high surface area, and robust mechanical properties [4, 10, 11]. In the past few

D. Momodu · A. Bello · J. Dangbegnon · F. Barzeger · M. Fabiane · N. Manyala (✉)
Department of Physics, Institute of Applied Materials, SARChI Chair in Carbon Technology and Materials, University of Pretoria, Pretoria 0028, South Africa
e-mail: Ncholu.Manyala@up.ac.za

years, many studies have focused on combining graphene with metal oxides or hydroxides [9, 12–16], conducting polymers [12, 17–19], and other activated carbon materials [20, 21]. Among the conducting polymers, polyaniline (PANI) and poly (3-hexylthiophene) (P3HT), which have the characteristic property of donating electrons, have recently been used in SC applications [17, 18]. Recent studies by A. Gupta et al. [17] involved an in situ synthesis of P3HT incorporated with graphene to form polymer/graphene composites with a good specific capacitance of 244 F g^{-1} at a current density of 0.2 A g^{-1}. Other researchers have also blended the P3HT polymer with fullerene acceptor material: [6, 6]-phenyl C_{61}-butyric acid methyl ester (PCBM), to form a hybrid blend of highly ordered P3HT:PCBM nanostructures with efficient donor–acceptor charge carriers. Wang et al. [22] reported a capacitance value of 0.14 F cm^{-2} for nanowires of P3HT:PCBM blend, obtained from cyclic voltammetry (CV) measurements. In general, conductive polymer blends with efficient electrical properties are obtained by an interpenetrating matrix of donor and acceptor materials. P3HT:PCBM blends have been extensively applied in organic solar cells [23–25] and recently in SCs due to their promising capacitive properties. However, reported values are still low due to the limited accessibility of electrolyte ions to the surface of the material [22, 26]. This could be mitigated by hybridizing this polymer with a material with a high surface area and which has additional properties necessary to improve the overall capacitive performance of the final composite.

Layered double hydroxides (LDHs), also known as hydrotalcite-like compounds, are a family of layered solids with structurally positively charged layers and interlayer balancing anions [27]. They have been used extensively for various applications due to their tunable composition, large surface area, and flexible ion exchangeability [28, 29]. Hence, the synergetic properties of both P3HT:PCBM and the LDHs should, in theory, improve the capacitive properties of the composite.

On the basis of the attractive properties of both graphene and LDH stated above, we report on the effect of the addition of nickel–aluminum-LDH-graphene foam (NiAl-LDH-GF) composite to the P3HT:PCBM polymer blend through a simple dip-coating approach in an effort to improve the capacitive performance of the latter. To the best of our knowledge, there has been no previous report on a composite of LDH-graphene (LDH-G) with a P3HT:PCBM polymer blend for supercapacitor application.

Experimental

Synthesis of NiAl-LDH-GF composite

GF was synthesized by chemical vapor deposition (CVD) onto catalytic nickel foam (NF) (Alantum Innovations in Alloy Foam Munich, Germany). The nickel foam with graphene was then immersed in 3.0 M hydrochloric acid (HCl) at 80 °C for 8 h to etch away the nickel template completely and thereafter rinsed several times in deionized water to obtain the graphene foam. NiAl-LDH composites were synthesized by adopting a facile solvothermal method reported in earlier work [3]. Typically, 2.400 g of urea, 2.139 g of $Ni(NO_3)_2$, and 0.724 g of $Al(NO_3)_3$ salts were dissolved in 80 ml of a pre-sonicated deionized water/ethanol solution containing graphene foam. After ultrasonication for a few minutes, the above mixture was transferred into an autoclave vessel and kept at 140 °C for 18 h. Finally, the composite was filtered and dried at 60 °C overnight for 8 h to obtain the final material.

Synthesis of P3HT-PCBM blend

Regioregular P3HT and PCBM (Sigma-Aldrich, purity >99.9 %) were used as received without further purification. In the preparation of the polymer blend, 45 mg of P3HT and 40 mg of PCBM (with a ratio of P3HT to PCBM=1:0.8) were dissolved in 3 ml of 1,2-chlorobenzene to form a 15 mg/ml solution.

Synthesis of the P3HT-PCBM/NiAl-LDH-GF composite

Ninety milligrams of the NiAl-LDH-GF powder obtained was dissolved and sonicated in 1 ml of ethanol. The solutions of P3HT:PCBM and NiAl-LDH-GF were then mixed and sonicated for 2 h. Lastly, the mixed solution was stirred for 24 h in the dark at 65 °C in order to obtain thorough mixing of the final product of the P3HT:PCBM/NiAl-LDH-GF composite. Thereafter, the composite solution was applied via a simple dip-coating technique to pre-weighed nickel foam (3×1 cm^2) as illustrated in Fig. 1. The foam was then re-weighed to obtain the amount of material coated onto it, and the coated area was also measured. This was then placed in a dark enclosure and allowed to dry slowly in normal air overnight due to the instability of the polymer blend under normal light [30]. Nickel foam dip-coated with a solution containing P3HT:PCBM blend alone was also prepared simultaneously for comparison purposes. The morphology of the samples was studied with a high-resolution Zeiss Ultra Plus 55 field emission scanning electron microscope (FE-SEM) operated at 1.0 kV. Raman spectra of the P3HT:PCBM, GF, NiAl-LDH, and P3HT:PCBM/Ni-Al-LDH-GF composite were recorded using a Jobin Yvon Horiba TX 6400 micro-Raman spectrometer equipped with a triple monochromator system to eliminate contributions from Rayleigh scattering. The samples were analyzed with a 514-nm argon excitation laser using a 509 objective lens with ×100 magnification and an acquisition time of 120 s. Surface area measurements were performed using the Brunauer–Emmett–Teller (BET) method. Pore size

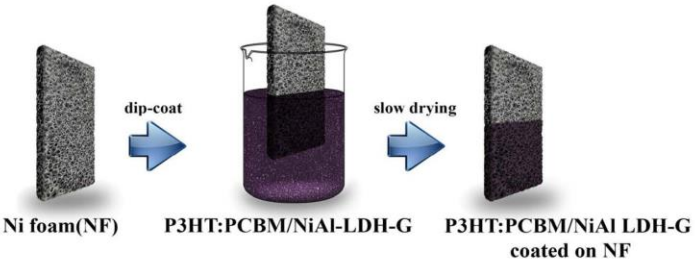

Fig. 1 The dip-coating technique using P3HT:PCBM/NiAl-LDH-GF solution

and pore volume were obtained using Barrett–Joyner–Halenda (BJH) method from the desorption branch of the isotherm. Electrochemical measurements were carried out using a Bio-Logic SP-300 workstation (Knoxville, TN 37930, USA) in a three-electrode configuration. The as-prepared P3HT:PCBM/NiAl-LDH-GF on NF served as the working electrode, a glassy carbon plate was used as the counter electrode, and Ag/AgCl (3.0-M KCl solution) was used as the reference electrode in a 6.0-M KOH electrolyte. Electrochemical impedance spectroscopy (EIS) was performed in the frequency range of 100 kHz–10 mHz.

Results and discussion

Figure 2 shows the morphology of the NF before and after coating with the P3HT:PCBM/NiAl-LDH-GF composite. Figure 2a shows the three-dimensional NF macroporous structure which makes it an excellent choice for use as a current collector. The inset in Fig. 2a is of higher magnification showing the grain boundaries of the NF. Figure 2b shows the NF coated with the P3HT:PCBM polymer blend. A view at a higher magnification is shown in the inset in Fig. 2b with dark patches appearing on the NF after coating. Figure 2c shows the NF coated with the P3HT:PCBM/NiAl-LDH-GF composite material. The presence of the composite material is evidenced at higher magnification of 1 μm by the rough ridges appearing on the NF after dip coating in the composite solution (see inset in Fig. 2c). As reported in an earlier study [22], a random orientation of the polymer chains occurs during a fast drying process. However, a slow drying process enhances a thermodynamically favorable re-orientation of the polymer chains leading to ordered nanostructures of the polymer on the supporting substrate. Thus, a degree of polymer

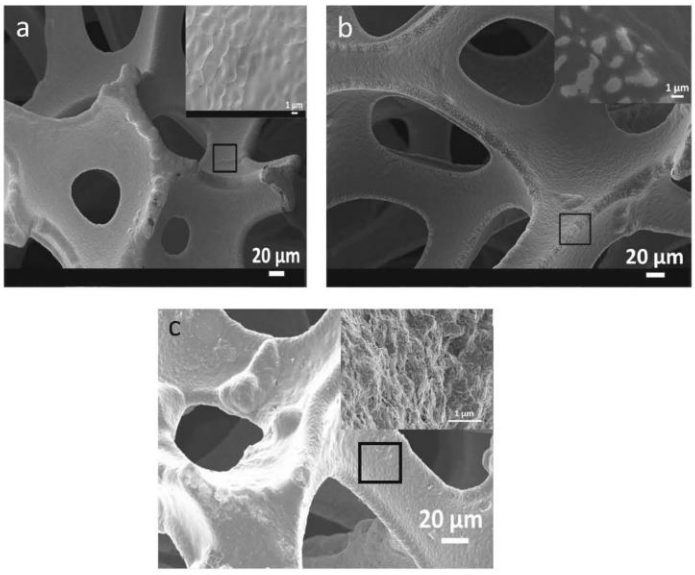

Fig. 2 SEM image of **a** Ni-foam (NF), **b** P3HT:PCBM on NF, and **c** P3HT:PCBM/NiAl-LDH-GF on NF (*insets* in **a**, **b**, and **c** show a higher magnification view at 1 μm of the region in the *square* on the NF)

nanostructure ordering should also occur on the supporting Ni foam; however, one should bear in mind that the addition of NiAl-LDH and graphene to the polymer solution may be detrimental for this ordering during dip coating.

Raman spectroscopy was used here to confirm the presence of the constituents of the composite material by studying their characteristic vibrational modes. Figure 3 shows the Raman spectra for NiAl-LDH, the P3HT:PCBM blend, and the P3HT:PCBM/NiAl-LDH-GF composite. The inset in the figure shows the Raman spectrum of GF. The peaks seen in the spectrum correspond to those of the composite material and are typical of each component of the composite with the bands at 1,594 and 2,704 cm^{-1} corresponding to the G and 2D bands of graphene but shifted because of the interaction between graphene and other materials in the composite (see the inset in Fig. 3) [31–33]. The peak at ~1,365 cm^{-1} and the shoulder appearing at ~1,445 cm^{-1} are very close to those related to the vibrational modes from the C–C intra-ring and the symmetric C=C stretching modes in the P3HT:PCBM blend, respectively [34–36]. These two modes, usually described as "in-plane ring skeleton modes", are used to quantify the degree of molecular order of the P3HT phase in the blend due to the fact that they are sensitive to π-electron delocalization of P3HT molecules [34]. The vibrational mode for fullerene-derived PCBM films usually appears at 1,469 cm^{-1}, based on earlier literature, and can be assigned to the dominant pentagonal-pinch mode $A_g(2)$ of C_{60} [37]. The Raman peak at around 1,469 cm^{-1} is usually overshadowed by the intense peak at ~1,450 cm^{-1} and cannot be resolved in our spectrum [36]. The band at ~1,025 cm^{-1} is typical of the NiAl-LDH vibrational mode [4, 33]. Furthermore, the Raman spectrum for the P3HT:PCBM/NiAl-LDH-GF composite clearly shows a broadening of the peaks at ~1,365 and ~1,445 cm^{-1}. This is accompanied by a reduction in the intensity of those peaks. These observations could be explained by the coexistence of the different materials of the composite which disrupts the initial order of the P3HT:PCBM polymer matrix [34]. Thus, from the Raman spectra, one can suggest that there is an interaction between the GF, the LDH material, and the P3HT:PCBM blend.

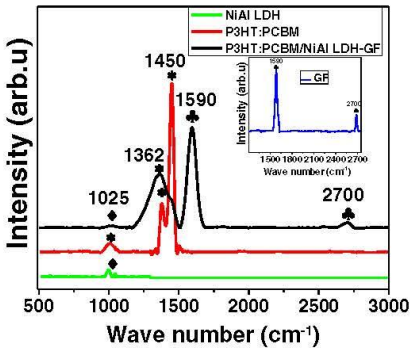

Fig. 3 Raman spectra of NiAl-LDH (*green spectrum*), GF (*blue spectrum* in figure inset), P3HT:PCBM (*red spectrum*), and P3HT:PCBM/NiAl-LDH-GF (*black spectrum*), respectively (note: *Diamond symbol* denotes LDH peak, *asterisk symbol* denotes P3HT:PCBM peaks, and *club symbol* denotes graphene peaks)

The supercapacitive performance of the P3HT:PCBM/NiAl-LDH-GF composite electrode material is dependent on its ability to accommodate as much active electrochemical sites for charge storage during operation. The presence of suitable mesopores within the electrode material (especially within the range of 2–5 nm) is also ideal to ensure the reduction of mass transfer of electrolyte during fast redox reactions [4]. As such, surface area measurements using the BET technique are necessary. The physical adsorption/desorption of N_2 at 77-K results shown in Fig. 4 displays the surface area and porosity for the prepared samples.

In the case of LDH alone, a type IV isotherm with a H_3-type hysteresis loop ($P/P_o>0.4$) appears, which indicates the presence of mesopores in the LDH material [4, 38] with an estimated specific surface area (SSA) of 57.8249 $m^2\ g^{-1}$. A higher BET SSA of 68.09 $m^2\ g^{-1}$ was observed for the NiAl-LDH-GF where GF has been added thereby increasing the availability of porous sites suitable for the polymer composite and possibly reducing the aggregation of LDH platelets (Fig. 4b). Thus, the addition of the mesoporous material to the P3HT:PCBM polymer blend was done to increase the surface area of the polymer-based composite, improving its charge storage capability by the availability of active mesoporous sites. This improvement is shown in Fig. 4c where the SSA of the P3HT:PCBM/NiAl-LDH-GF composite is drastically increased to 22.33 $m^2\ g^{-1}$ from an initial value of 2.58 $m^2\ g^{-1}$ for the P3HT:PCBM blend alone. Figure 4d shows the pore size distribution for the composite with a pore diameter range of 2–5 nm which shows the successful inclusion of mesoporous sites necessary for charge storage.

Figure 5a compares the CV curves of the NF current collector, the pristine P3HT:PCBM blend, and the P3HT:PCBM/NiAl-LDH-GF composite at a scan rate of 10 mV s^{-1}. The CV curve of the NF current collector shows a very low current density response when compared to P3HT:PCBM and the P3HT:PCBM/NiAl-LDH-GF composite, respectively. This shows the negligible capacitive contribution of the NF current collector in both the P3HT:PCBM and the P3HT:PCBM/NiAl-LDH-GF composite active electrodes. The CV measurements at different scan rates of the

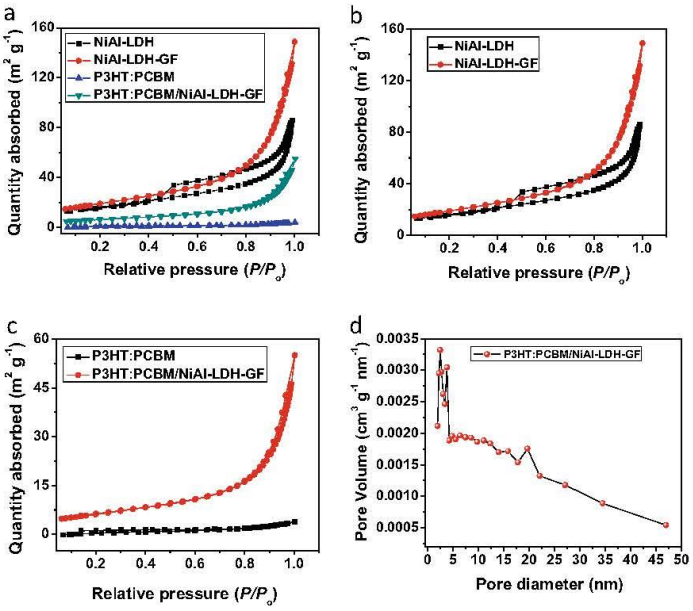

Fig. 4 **a**–**c** N_2 adsorption/desorption isotherms for NiAl-LDH, NiAl-LDH-GF, P3HT:PCBM, and P3HT:PCBM/NiAl-LDH-GF samples; (**b**) the pore size distribution of the P3HT:PCBM/NiAl-LDH-GF composite

pristine P3HT:PCBM are shown in Fig. 5b. The oxidation and reduction peaks appear at 0.35 and 0.24 V, respectively. The ratio of the absolute values of the anodic to cathodic current (I_{pa}/I_{pc}) is approximately unity, which is a clear indication that the redox reaction of P3HT:PCBM is a reversible process. The CV curves of the P3HT:PCBM/NiAl-LDH-GF composite shown in Fig. 5c, also at different scan rates, exhibit higher current responses when compared to the pristine

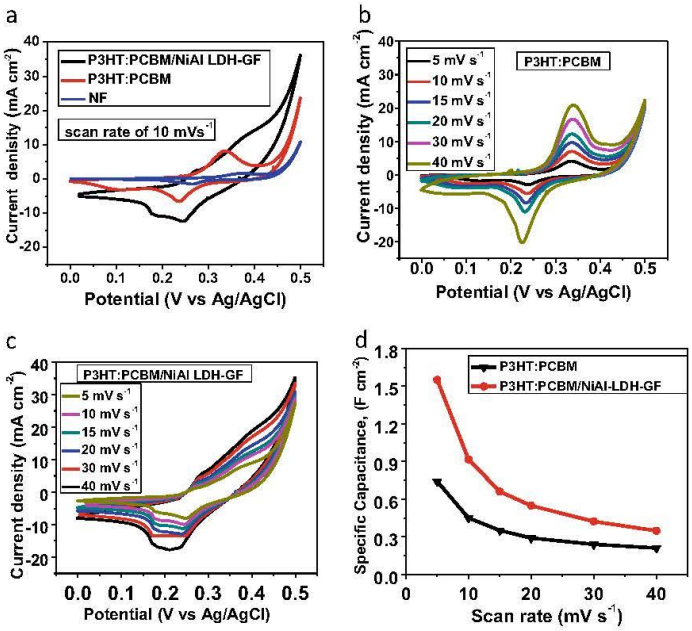

Fig. 5 Cyclic voltammetry curves of **a** NF, P3HT:PCBM and P3HT:PCBM/NiAl-LDH-GF samples at 10 mV s^{-1} scan rate in a 6-M KOH three-electrode configuration; **b**, **c** P3HT:PCBM alone and P3HT:PCBM/NiAl-LDH-GF composite, respectively, measured at scan rates of 5–40 mV s^{-1}; **d** specific capacitance of P3HT:PCBM/NiAl-LDH-GF composite electrode at different scan rates calculated from the CV curves

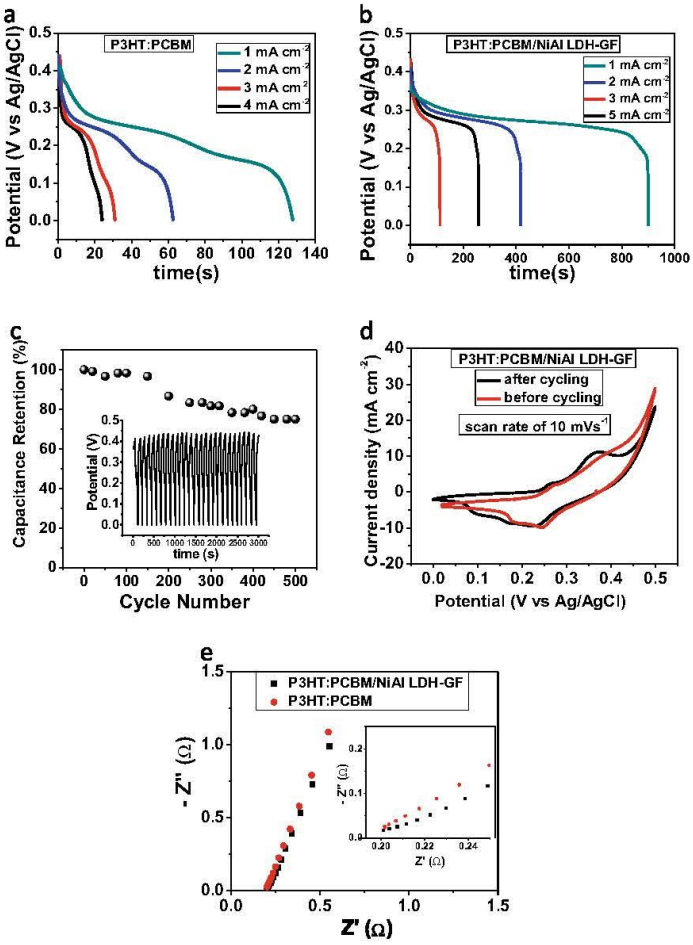

Fig. 6 Galvanostatic charge–discharge profiles of **a** P3HT:PCBM/NiAl-LDH-GF and **b** P3HT:PCBM electrodes at different current densities in a three-electrode configuration; **c** the capacity retention of the composite at a current density of 10 mA cm^{-2} (the *inset* in the figure shows the continuous charge–discharge curve); **d** the CV curves of P3HT:PCBM/NiAl-LDH-GF on NF at 10 mV s^{-1} scan rate before and after cycling showing stability of the electrode and **e** the Nyquist plot for the pristine P3HT:PCBM polymer alone and P3HT:PCBM/NiAl-LDH-GF composite electrode

P3HT:PCBM, indicating a better capacitive performance. The specific capacitance was calculated using the following formula from the CV curves [17]:

$$C_S\left(\frac{F}{cm^2}\right) = \frac{1}{\overline{a}v(V_2-V_1)}\int_{V1}^{V_2} I(V)dV \quad (1)$$

where $\overline{a}$ is the area of the coated surface with the active material (in cm^2), υ is the scan rate (in mV s^{-1}), V_1 and V_2 are the integration limits, and $I(V)$ is the response current during the CV measurement.

A higher specific capacitance was obtained for the composite which contains the LDH-GF material, for each scan rate. For example, a specific capacitance of the pristine P3HT:PCBM nanostructure on NF is calculated as 0.34 F cm^{-2}, while an improved value of 0.92 F cm^{-2} is recorded for the P3HT:PCBM/NiAl-LDH-GF composites, both at 10 mV s^{-1}. Figure 5d shows the trend of the specific capacitance as a function of the scan rate. As expected, the specific capacitance decreases with increasing scan rate. This is due to the limited movement of ions and protons by diffusion at higher scan rates, which leaves only the outer active surface for charge storage [4, 39].

Figure 6a, b shows the variation in discharge time with current density for both pristine P3HT:PCBM and the P3HT:PCBM/NiAl-LDH-GF composite, respectively. A higher discharge time is observed for the composite material compared to the P3HT:PCBM polymer. The presence of the graphene and hydrotalcite structure within the polymer creates more surface interaction for charge transport. The mechanism of the charge storage for the polymer alone is based on both interfacial electric double-layer capacitance (EDLC) and

redox processes from pseudocapacitance. The EDLC is based on electrostatic charge separation and accumulation, while the redox process arises from the electron transfer between the $P3HT^{+}$ donor and the $PCBM^{-}$ acceptor with electrosorption and surface redox processes at the electrolyte/electrode material interface. Similar pseudocapacitive nature has been reported for other conductive polymers which have been used for supercapacitor applications [17, 18]. For an ideal SC, the discharge curves should be linear; however, the nonlinearity observed in the composite material confirms the pseudocapacitive nature of the LDH material and the polymer blend.

The specific capacitance was also calculated from the galvanostatic charge–discharge (CD) curves using the formula [28]:

$$C_S\left(\mathrm{F/cm^2}\right) = \frac{IT_d}{\overline{a}\Delta V} \tag{2}$$

where I is the current (A), T_d is the discharge time (s), $\overline{a}$ is the area of the coated electrode with active material (in cm^2), and ΔV is the voltage range (in V).

An improvement in specific capacitance was also observed from the charge–discharge measurements for the composite containing the LDH-GF material. For example, at a current density of 2 mA cm^{-2}, the specific capacitance was found to increase from 0.29 F cm^{-2} for the pristine P3HT:PCBM nanostructure to a value of 1.22 F cm^{-2} for the composite structure. Thus, the results of both the CV and CD measurements showed improved capacitance of the polymer due to the presence of the NiAl-LDH-GF. The improvement is attributed to the creation of active mesopores necessary for charge storage in the composite material. This is seen from the improvement in the specific surface area obtained from the BET analysis.

Figure 6c shows the continuous CD curve of the composite at a current density of 10 mA cm^{-2}. The composite retained 75 % of its initial capacitance after 500 galvanostatic CD cycles, which shows the reliable stability of the composite material for use as an SC electrode. Most polymer electrodes begin to exhibit degradation after 200–300 cycles due to mechanical degradation during cycling [40], hence the idea of adding other materials to form a composite which will improve the overall polymer stability. Furthermore, in an effort to study the effect of cycling on the electrochemical stability of the P3HT:PCBM/NiAl-LDH-GF composite, the electrodes were subjected to CV tests once again after 500 cycles. An insignificant shift was observed in the redox peaks after cycling as illustrated in Fig. 6d. This further confirms the stability of the composite electrode for possible applications in supercapacitors.

The EIS result for the composite electrode is shown in Fig. 6e (Nyquist plot), alongside that of the P3HT:PCBM. The Nyquist plot is a representation of the real and imaginary parts of the impedance in the electrode material. The plot is usually divided into two regions, namely, the high-frequency region, which is characteristic of the charge-transfer process taking place at the electrode/electrolyte interface, and a straight line in the low-frequency region, which represents the diffusion process taking place at this interface. The intercept in the high-frequency region with the x-axis corresponds to the equivalent series resistance (ESR), which consists of the resistance of the aqueous electrolyte and the intrinsic resistance of the composite material [4]. An internal resistance of 0.2 Ω was recorded for the composite electrode (figure inset), which is very similar to that of the P3HT:PCBM polymer. This suggests that there was no change in the internal resistance resulting from the addition of the LDH-GF material.

Conclusion

We synthesized and incorporated NiAl-LDH-GF into a P3HT:PCBM polymer to obtain a composite material with an improved specific capacitive behavior. The composite exhibits a specific capacitance of 1.22 F cm^{-2} at a current density of 2.0 mA cm^{-2} from galvanostatic charge–discharge measurements and 0.92 F cm^{-2} at a scan rate of 10 mV s^{-1} from cyclic voltammetry measurements, which is an order of magnitude higher than for the pristine sample and is, to the best of our knowledge, among the highest values reported so far for P3HT:PCBM nanostructure supercapacitors [22]. The 75 % capacitance retention of the composite after 500 galvanostatic charge–discharge cycles also shows the reliable stability of the composite material for use in energy storage devices.

Acknowledgments This work is based on research supported by the South African Research Chairs Initiative (SARChI) of the Department of Science and Technology (DST) and the National Research Foundation (NRF).

Conflict of interest Any opinion, findings, and conclusions or recommendations expressed in this work are those of the authors, and therefore, the NRF and DST do not accept any liability with regard thereto. D.M acknowledges the financial support from the NRF Innovation Doctoral Fund and the University of Pretoria PhD bursary scheme for his study.

References

1. Conway B (1991) Transition from "supercapacitor" to "battery" behavior in electrochemical energy storage. J Electrochem Soc 138: 1539–1548
2. Tao Y, Ruiyi L, Zaijun L, Junkang L, Guangli W, Zhiquo G (2013) A free template strategy for the fabrication of nickel/cobalt double hydroxide microspheres with tunable nanostructure and morphology for high performance supercapacitors. RSC Adv 3:19416
3. Song Y, Wang J, Li Z, Guan D, Mann T, Liu Q, Zhang M, Liu L (2012) Self-assembled hierarchical porous layered double

hydroxides by solvothermal method and their application for capacitors. Microporous Mesoporous Mater 148:159–165
4. Yang W, Gao Z, Wang J, Ma J, Zhang M, Liu L (2013) Solvothermal one-step synthesis of Ni-Al layered double hydroxide/carbon nanotube/reduced graphene oxide sheet ternary nanocomposite with ultrahigh capacitance for supercapacitors. ACS Appl Mater Interfaces 5:5443–5454
5. Simon P, Gogotsi Y (2008) Materials for electrochemical capacitors. Nat Mater 7:845–854
6. Notten PHL, Roozeboom F, Niessen RAH, Baggetto L (2007) 3D integrated all solid state rechargeable batteries. Adv Mater 19:4564–4567
7. Ruzmetov D, Oleshko VP, Haney PM, Lezec HJ, Karki K, Baloch KH, Agrawal AK, Davydov AV, Krylyuk S, Liu Y (2011) Electrolyte stability determines scaling limits for solid-state 3D Li ion batteries. Nano Lett 12:505–511
8. Hall PJ, Mirzaeian M, Fletcher SI, Sillars FB, Rennie AJR, Shitta-Bey GO, Wilson G, Cruden A, Carter R (2010) Energy storage in electrochemical capacitors: designing functional materials to improve performance. Energy Environ Sci 3:1238–1251
9. Tao Y, Haiyan Z, Ruiyi L, Zaijun L, Junkang L, Guangli W, Zhiquo G (2013) Microwave synthesis of nickel/cobalt double hydroxide ultrathin flowerclusters with three-dimensional structures for high-performance supercapacitors. Electrochim Acta 111:71–79
10. Yang W, Ratinac KR, Ringer SP, Thordarson P, Gooding JJ, Braet F (2010) Carbon nanomaterials in biosensors: should you use nanotubes or graphene? Angew Chem Int Ed 49:2114–2138
11. Neto AHC, Castro Neto AH, Peres NMR, Neto AHC, Castro NAH, Peres NMR, Novoselov KS, Geim AK (2009) The electronic properties of graphene. Rev Mod Phys 81:109–162
12. Shen J, Yang C, Li X, Wang G (2013) High-performance asymmetric supercapacitor based on nanoarchitectured polyaniline/graphene/carbon nanotube and activated graphene electrodes. ACS Appl Mater Interfaces 5:8467–8476
13. Bello A, Fashedemi OO, Fabiane M, Lekitima JN, Ozoemena KI, Manyala N (2013) Microwave assisted synthesis of MnO_2 on nickel foam-graphene for electrochemical capacitor. Electrochim Acta 114:48–53
14. Bello A, Makgopa K, Fabiane M, Dodoo-Ahrin D, Ozoemena KI, Manyala N (2013) Chemical adsorption of NiO nanostructures on nickel foam-graphene for supercapacitor applications. J Mater Sci 40:6707–6712
15. Khamlich S, Bello A, Fabiane M, Ngom BD, Manyala N (2013) Hydrothermal synthesis of simonkolleite microplatelets on nickel foam-graphene for electrochemical supercapacitors. J Solid State Electrochem 17:2879–2886
16. Bello A, Fashedemi OO, Lekitima JN, Mopeli F, Dodoo-Arhin D, Ozoemena KI, Gogotsi Y, Charlie Johnson AT, Manyala N (2013) High-performance symmetric electrochemical capacitor based on graphene foam and nanostructured manganese oxide. AIP Adv 3:082118
17. Gupta A, Akhtar AJ, Saha SK (2013) In-situ growth of P3HT/graphene composites for supercapacitor application. Mater Chem Phys 140:616–621
18. Wu Q, Xu Y, Yao Z, Liu A, Shi G (2010) Supercapacitors based on flexible graphene/polyaniline nanofiber composite films. ACS Nano 4:1963–1970
19. Lai L, Yang H, Wang L, Teh BK, Zhong J, Chou H, Chen L, Chen W, Shen Z, Ruoff RS, Lin J (2012) Preparation of supercapacitor electrodes through selection of graphene surface functionalities. ACS Nano 6:5941–5951
20. Stoller M, Park S, Zhu Y, An J, Ruoff RS (2008) Graphene-based ultracapacitors. Nano Lett 8:3498–3502
21. Zhang W, Ma C, Fang J, Cheng J, Zhang X, Dong S, Zhang L (2013) Asymmetric electrochemical capacitors with high energy and power density based on graphene/CoAl-LDH and activated carbon electrodes. RSC Adv 3:2483–2490
22. Wang YZ, Wang Q, Xie HY, Xie HY, Ho LP, Tan DMF, Diao YY, Chen W, Xie XN (2012) Fabrication of highly ordered P3HT:PCBM nanostructures and its application as a supercapacitive electrode. Nanoscale 4:3725–3728
23. Dennler G, Scharber MC, Brabec CJ (2009) Polymer-fullerene bulk-heterojunction solar cells. Adv Mater 21:1323–1338
24. Gomez De Arco L, Zhang Y, Schlenker CW, Ryu K, Thompson ME, Zhou C (2010) Continuous, highly flexible, and transparent graphene films by chemical vapor deposition for organic photovoltaics. ACS Nano 4:2865–2873
25. Tan MJ, Zhong S, Li J, Chen Z, Chen W (2013) Air-stable efficient inverted polymer solar cells using solution-processed nanocrystalline ZnO interfacial layer. ACS Appl Mater Interfaces 5:4696–4701
26. Zhang Z, Chen X, Chen P, Guan G, Qiu L, Lin H, Yang Z, Bai W, Luo Y, Peng H (2014) Integrated polymer solar cell and electrochemical supercapacitor in a flexible and stable fiber format. Adv Mater 26:466–470
27. Wang J, Zhou J, Li Z, Liu Q, Yang P, Jing X, Zhang M (2010) Design of magnetic and fluorescent Mg–Al layered double hydroxides by introducing Fe_3O_4 nanoparticles and Eu^{3+} ions for intercalation of glycine. Mater Res Bull 45:640–645
28. Wang J, Song Y, Li Z, Liu Q, Zhou J, Jing X, Zhang M, Jiang Z (2010) In situ Ni/Al layered double hydroxide and its electrochemical capacitance performance. Energy Fuel 24:6463–6467
29. Wang Q, O'Hare D (2012) Recent advances in the synthesis and application of layered double hydroxide (LDH) nanosheets. Chem Rev 112:4124–4155
30. Rivaton A, Chambon S, Manceau M (2010) Light-induced degradation of the active layer of polymer-based solar cells. Polym Degrad Stab 95:278–284
31. Ferrari A, Basko D (2013) Raman spectroscopy as a versatile tool for studying the properties of graphene. Nat Nanotechnol 8:235–246
32. Ferrari AC, Robertson J (2000) Interpretation of Raman spectra of disordered and amorphous carbon. Phys Rev B 61:14095
33. Gao Z, Wang J, Li Z, Yang W, Wang B (2011) Graphene nanosheet/Ni^{2+}/Al^{3+} layered double-hydroxide composite as a novel electrode for a supercapacitor. Chem Mater 23:3509–3516
34. Tsoi WC, James DT, Kim JS, Nicholson PG, Murphy CE, Bradley DDC, Nelson J, Kim JS (2011) The nature of in-plane skeleton Raman modes of P3HT and their correlation to the degree of molecular order in P3HT:PCBM blend thin films. J Am Chem Soc 133:9834–9843
35. Saini V, Li Z, Bourdo S, Dervishi E, Xu Y, Ma X, Kunets VP, Salamo GJ, Viswanathan T, Biris AR, Saini D, Biris AS (2009) Electrical, optical, and morphological properties of P3HT-MWNT nanocomposites prepared by in situ polymerization. J Phys Chem C 113:8023–8029
36. Falke S, Eravuchira P, Materny A, Lienau C (2011) Raman spectroscopic identification of fullerene inclusions in polymer/fullerene blends. J Raman Spectrosc 42:1897–1900
37. Kuzmany H, Matus M, Burger B, Winter J (1994) Raman scattering in C_{60} fullerenes and fullerides. Adv Mater 6:731–745
38. Yu J, Yu JC, Ho W, Leung MKP, Cheng B, Zhang G, Zhao X (2003) Effects of alcohol content and calcination temperature on the textural properties of bimodally mesoporous titania. Appl Catal A Gen 255:309–320
39. Lao ZJ, Konstantinov K, Tournaire Y, Ng SH, Wang GX, Liu HK (2006) Synthesis of vanadium pentoxide powders with enhanced surface-area for electrochemical capacitors. J Power Sources 162:1451–1454
40. Wang G, Zhang L, Zhang J (2012) A review of electrode materials for electrochemical supercapacitors. Chem Soc Rev 41:797–828

4.2.4 Concluding Remarks

A simple dip-coating technique has been used to coat a P3HT:PCBM/NiAl-LDH-GF active material onto pre-cleaned nickel foam current collectors. The composite electrode were successfully characterized and found to exhibit an improved areal specific capacitance of over an order of magnitude (from 0.29 F cm^{-2} for the pristine P3HT:PCBM nanostructure to a value of 1.22 F cm^{-2} for the composite electrode). This improvement was attributed to the addition of NiAl LDH-GF to the main polymer matrix and is so far the highest value reported for P3HT:PCBM based supercapacitors in aqueous electrolyte. Thus, the composite electrode serves as a potential candidate in energy storage applications.

4.2.5 References

[1] Q. Wu, Y. Xu, Z. Yao, A. Liu, G. Shi, ACS Nano 4 (2010) 1963.

[2] A. Gupta, A.J. Akhtar, S.K. Saha, Mater. Chem. Phys. 140 (2013) 616.

[3] Y.Z. Wang, Q. Wang, H.Y. Xie, L.P. Ho, D.M.F. Tan, Y.Y. Diao, W. Chen, X.N. Xie, Nanoscale 4 (2012) 3725.

[4] Z. Zhang, X. Chen, P. Chen, G. Guan, L. Qiu, H. Lin, Z. Yang, W. Bai, Y. Luo, H. Peng, Adv. Mater. 26 (2014) 466.

[5] Q. Liu, Z. Liu, X. Zhang, L. Yang, N. Zhang, G. Pan, S. Yin, Y. Chen, J. Wei, Adv. Funct. Mater. 19 (2009) 894.

[6] L. Lai, H. Yang, L. Wang, B.K. Teh, J. Zhong, H. Chou, L. Chen, W. Chen, Z. Shen, R.S. Ruoff, J. Lin, ACS Nano 6 (2012) 5941.

[7] Z. Gao, J. Wang, Z. Li, W. Yang, B. Wang, Chem. Mater. 23 (2011) 3509.

[8] A.C. Ferrari, J. Robertson, Phys. Rev. B 61 (2000) 14095.

[9] G. Wang, J. Yang, J. Park, X. Gou, B. Wang, H. Liu, J. Yao, J. Phys. Chem. C 112 (2008) 8192.

[10] W.C. Tsoi, D.T. James, J.S. Kim, P.G. Nicholson, C.E. Murphy, D.D.C. Bradley, J. Nelson, J.-S. Kim, J. Am. Chem. Soc. 133 (2011) 9834.

[11] V. Saini, Z. Li, S. Bourdo, E. Dervishi, Y. Xu, X. Ma, V.P. Kunets, G.J. Salamo, T. Viswanathan, A.R. Biris, D. Saini, A.S. Biris, J. Phys. Chem. C 113 (2009) 8023.

[12] S. Falke, P. Eravuchira, A. Materny, C. Lienau, J. Raman Spectrosc. 42 (2011) 1897.

[13] H. Kuzmany, M. Matus, B. Burger, J. Winter, Adv. Mater. 6 (1994) 731.

[14] W. Yang, Z. Gao, J. Wang, J. Ma, M. Zhang, L. Liu, ACS Appl. Mater. Interfaces 5 (2013) 5443.

4.3 In-situ growth of simonkolleite-graphene foam composites for pseudocapacitor electrodes

4.3.1 Introduction

Simonkolleite (simonK, $Zn_5(OH)_8Cl_2{\cdot}H_2O$) has a rhombohedral structure with $R\bar{3}m$ space group. It also crystallizes hexagonally with a perfect cleavage parallel to the (001) direction [1]. The detailed structural arrangement of the individual atoms in a simonkolleite lattice including the presence of hydrogen bonding from the OH groups as well as the oxygen vacancies available on the surface makes them electrically and chemically active [1,2] for numerous applications ranging from sensing to electrochemical capacitor material electrodes [3,4].

However, the specific capacitance (C_s) values recorded so far for pristine simonkolleite platelets are still very low when compared with other metal hydroxides and this limits their use for energy storage device applications since lower C_s values implies lower energy density values. This poor specific capacitance is attributed to the high tendency of the simonK sheets to restack together, low surface area as well as low electrical conductivity. In order to overcome this problem, numerous researchers have adopted various methods such as the use of surfactants [5], incorporation of high surface area carbon materials [4,6] to address the issues cited by creating porous sites for easier charge transport and storage. This would also create more available surface area for electrochemical surface reactions associated with efficient charge storage.

Based on the proposed ideas and assumptions made, an in situ solvothermal growth technique was used to synthesize simonkolleite sheets in the presence of high surface

area graphene foam (GF) flakes to obtain simonkolleite-graphene foam (simonK/GF) nanostructures on a nickel foam-graphene (NF-G) template. This choice of template was based on the improved electrochemical performance recorded in section 4.2.1 for similar metal hydroxide nanosheets interlaced with each other to form an interconnected framework. This approach ensures the natural growth of the simonK sheets in the midst of the GF flakes. The growth method presents a simplified all-in-one procedure of fabricating composite electrodes. Thereafter, detailed analyses on the morphological, structural, surface and electrochemical properties are explored.

4.3.2 Results and discussion

The results obtained from the in situ growth of hexagonal simonK sheets interlaced with graphene on NF-G current collector are presented. The NF-G surface acts as a nucleation site for the growth of the simonK sheets while the graphene sheets ensured the exfoliation of the sheets and prevented their restacking. These were confirmed from the comparison of the SEM micrographs obtained for both pristine simonK and simonK/GF nanostructures.

The specific surface area (SSA) values obtained from the BET measurements for both simonK and simonK/GF composite materials show an improvement which was confirmed from the electrochemical characterization subsequently carried out.

Results from the electrochemical analysis show an excellent specific capacitance value for the simonK/GF composite as compared to the simonK alone.

Detailed information on the analyses using different characterization technique and the results is presented in the attached publication below.

4.3.3 Publication 3: Simonkolleite-graphene foam composites and their superior electrochemical performance

Electrochimica Acta 151 (2015) 591–598

Contents lists available at ScienceDirect

Electrochimica Acta

journal homepage: www.elsevier.com/locate/electacta

Simonkolleite-graphene foam composites and their superior electrochemical performance

D.Y. Momodu, F. Barzegar, A. Bello, J. Dangbegnon, T. Masikhwa, J. Madito, N. Manyala *

Department of Physics, Institute of Applied Materials, SARCHI Chair in Carbon Technology and Materials, University of Pretoria, Pretoria 0028, South Africa

ARTICLE INFO

Article history:
Received 19 September 2014
Received in revised form 28 October 2014
Accepted 4 November 2014
Available online 6 November 2014

Keywords:
simonkolleite sheets
graphene foam
composites
supercapacitor

ABSTRACT

Simonkolleite-graphene foam (SimonK/GF) composite has been synthesized by a facile solvothermal and environmentally friendly technique with excellent electrochemical properties. The obtained product was initially analyzed by scanning electron microscopy (SEM), Brunauer–Emmett–Teller (BET), X-ray diffraction (XRD), Fourier transform infrared resonance (FTIR) spectroscopy and cyclic voltammetry (CV) techniques. The microscopy results reveal hexagonal sheets interlaced with each other and adjacent graphene sheets. The existence of graphene foam in the simonK/GF composite is further confirmed from the structural and the optical characteristics obtained from XRD and FTIR respectively. The BET results obtained indicate an improvement in the surface area due to the addition of graphene foam to a value of 39.58 $m^2 g^{-1}$. The N_2 adsorption/desorption also shows the presence of active mesopores required for charge transport. As a promising electrode material for supercapacitors, the composite shows a high specific capacitance value of 1094 F/g at 1 A/g with a coulombic efficiency of 100% after 1000 cycles. These results show a potential for adoption of this composite in energy storage applications.

1. Introduction

In the developing field of energy storage technology, the design and fabrication of efficient energy storage devices with high energy and power densities are of growing concern today. Numerous scientists have engaged in active research to develop robust and reliable energy storage systems which will match the increasing demand for energy in a variety of applications from energy storage systems in portable hand-held devices to back-up systems in hybrid electric motor vehicles.

Supercapacitors (SCs) with high power densities and long cycle life as compared to much common hybrid batteries in use today are promising candidates for such applications. However, they are also characterized with low energy densities in comparison to batteries which creates a drawback for their wide applications [1]. The nature of the electrode material which makes up the SC is one of the most important factors that determine its performance.

Based on the device operation mechanism, SCs can be broadly divided into two classes; the electric double layer capacitors (EDLCs) and the pseudocapacitors [2]. In order to deal with the problem of low energy density, most recent studies include combining materials with pseudocapacitive and electric double layer capacitive (EDLC) properties [2–8]. This is achieved by combining high specific surface area carbonaceous materials (e.g. graphene [3,4], carbon nanotubes [5–7], activated carbon [8,9]) with transition metal oxides and hydroxides with good redox properties.

For example, Gao's research group illustrated the production of graphene nanosheet-layered double hydroxide (GNS/LDH) by a simple hydrothermal technique [3]. In the study, glucose was used as a reducing agent in place of toxic hydrazine to exfoliate graphene oxide (GO) and obtain an even dispersion of GNS in water. The observed remarkable specific capacitance was attributed to be due to the combination of electric double layer capacitance (EDLC) and Faradaic pseudocapacitance from the open structure system with improved contact between the electrode/electrolyte interface [3]. The conductive network of graphene sheets overlapping each other was reported to facilitate fast electron transfer between the active composite material and the charge collector. Another study by Fao et al., [8] reports a graphene/MnO_2 composite as positive electrode synthesized by microwave irradiation with activated carbon nanofibres (ACN) as negative electrode in an asymmetrical cell with Na_2SO_4 aqueous electrolyte. A maximum energy density of 51.1 Wh Kg^{-1} at a corresponding

* Corresponding author. Tel.: +27 012 420 3549; fax: +27 012 420 2516.
E-mail address: ncholu.manyala@up.ac.za (N. Manyala).

http://dx.doi.org/10.1016/j.electacta.2014.11.015
0013-4686/

power density of 102.2 W kg^{-1} was obtained with excellent cycling stability retention of 97% after 1000 cycles. The observed device performance was attributed to the synergistic properties of both electrodes which provided an extended voltage window necessary for an improved energy density.

Recently, simonkolleites (SimonK, also known as zinc chloride hydroxide monohydrate, $Zn_5(OH)_8Cl_2 \cdot H_2O$) have received enormous attention due to their morphological properties composed of slabs and platelets suitable for numerous applications ranging from gas sensing [10] to materials for supercapacitor applications [11]. They also crystallize hexagonally with a perfect cleavage parallel to the (001) direction [12]. Similar to metal oxides, simonkolleites contain electrochemically active sites necessary for efficient charge storage. SimonK is electrically and chemically active due to the oxygen vacancies available on its surface, as in the case of ZnO. These vacancies may then act as n-type donors and subsequently improve the material's conductivity [10]. For supercapacitor applications, the abundance of a hexagonal microplatelet interactive network will likely provide the surface required for ionic surface interactions during operation. However, the pseudocapacitance of pristine simonK for energy storage is still low when compared with other metal oxides and hydroxides due to their lower electrical conductivity, lower surface area and tendency of the sheets to stack together. To overcome such limitations, efforts have been made by previous researchers to use carbon materials, such as graphene [3,11] or surfactants [13], to reduce the restacking and also improve the sheet thickness which would consequently improve the surface area and active porous sites for charge transport and storage.

The obtained hybrid system composed of simonkolleite-graphene will most likely have an improved electron transport rate, high electrolyte contact area for ion accessibility by creating more pores within the composite material. The combination of the graphene foam with simonkolleite microplatelets integrates the positive properties of electric double layer capacitance and pseudocapacitance. In addition, an in situ solvothermal synthesis approach of the simonK in the presence of evenly dispersed graphene foam leads to the synthesis of a simonkolleite-graphene foam composite (SimonK/GF) electrode with successful delamination/spacing of the simonkolleite sheets and will subsequently produce thinner sheets with improved surface properties and specific capacitance [4,14]. The in situ growth approach on a conductive substrate such as nickel-foam graphene ensures the simplification of the entire fabrication process and the direct acquisition of the composite electrode for device application. Although these are the desired properties for energy storage nanomaterials suitable for supercapacitors applications, limited studies have been done in this regards in relation to simonkolleite microplatelets.

In this present study, based on the considerations mentioned above, the synthesis of simonkolleite-graphene foam composite (SimonK/GF) is carried out with a subsequent study on the morphological, structural and electrochemical properties of the synthesized product. Analysis of the scanning microscopy images reveal relatively thin hexagonal sheets of simonkolleite interlaced with graphene sheets. Notably, the SimonK/GF composite showed an improved surface area with a superior electrochemical performance from cyclic voltammetry (CV) compared with SimonK alone. These results is a considerable improvement over earlier studies on simonkolleite structures for supercapacitor applications [11], wherein a similar in situ approach was adopted to grow simonkolleite on nickel foam-graphene template as electrode material for electrochemical applications. These results show the potential application of SimonK/GF composites as suitable electrodes for pseudocapacitors.

2. EXPERIMENTAL

2.1. Synthesis of nickel foam-graphene template and graphene foam

The nickel foam-graphene (NF-G) current collector was prepared by an atmospheric pressure chemical vapor deposition (AP-CVD) technique. Briefly, a known mass of compressed nickel foam template (Alantum, Munich, Germany), with an areal density of 420 g m^{-2} was placed in a quartz tube for the CVD growth of graphene. The nickel foam was first annealed at 1000 °C in the presence of Ar and H_2 gas for 60 minutes, prior to the introduction of the carbon source (CH_4 gas) at 968 °C. The flow rates of the gases Ar:H_2:CH_4 were 300:200:10 SCCM respectively. After 60 minutes of deposition, the samples were rapidly cooled by manually pushing the quartz tube to a lower temperature region to obtain the nickel foam-graphene.

In order to obtain the graphene foam, the samples were further immersed in 3.0 M HCl and placed on a hot plate at 60 °C to ensure complete etching of the nickel supporting structure. After complete etching of the nickel, the remaining graphene foam was washed several times in deionized water and dried in the oven to obtain the final graphene foam product.

2.2. In situ synthesis of simonkolleite-graphene foam composite

Simonkolleite-graphene foam composite was deposited directly on the NF-G template using an aqueous chemical growth technique whereby a solution containing equimolar portions of 2.974 g of zinc nitrate hexahydrate ($Zn(NO_3)_2 \cdot 6H_2O$), 0.588 g of sodium chloride (NaCl) and 4.102 g of hexamethylenetetramine ($C_6H_{12}N_4$, HMT) were first dissolved in deionized water. The next step involved adding 25 mg of graphene foam sonicated for 12 hours in water to the mixture prepared earlier and stirring the combined mixture with graphene foam for 15 minutes. Subsequently, the final mixture was transferred into a 150 ml Teflon-lined autoclave vessel and nickel foam-graphene substrate were immersed vertically into the reaction vessel kept at 110 °C for 19 hours. Thereafter, the autoclave was allowed to gradually cool down to ambient temperature. The final simonK/GF composite electrode was obtained after washing and drying at 60 °C.

The formation of simonkolleite ($Zn_5(OH)_8Cl_2 \cdot H_2O$) proceeds competitively in the solution following a set of successive chemical reactions as reported in our earlier publication [11]:

$$C_6H_{12}N_4 + 6H_2O \rightarrow 6HCHO + 4NH_3 \quad (1)$$

$$NH_3 + H_2O \rightarrow NH^{4+} + OH^- \quad (2)$$

$$NaCl + H_2O \rightarrow Na^+ + Cl^- + H_2O \quad (3)$$

$$Zn\,(NO_3)_2 \cdot 6H_2O + H_2O \rightarrow Zn^{2+} + 2NO_3^- + 7H_2O \quad (4)$$

$$Zn^{2+} + 8OH^- + 2Cl^- + H_2O \rightarrow Zn_5(OH)_8Cl_2 \cdot H_2O \quad (5)$$

Initially, HMT ($C_6H_{12}N_4$) disintegrates into formaldehyde (HCHO) and ammonia (NH_3). Ammonia tends to disintegrate deionized water to produce OH^- anions. Furthermore, NaCl disintegrates in water to form sodium cations (Na^+) and (Cl^-) chloride anions while Zn $(NO_3)_2 \cdot 6H_2O$ simultaneously disintegrates into zincate (Zn^{2+}) and nitrate (NO_3^-) ions. Lastly, OH^- and Cl^- anions react with Zn^{2+} cations to synthesize simonkolleite nanoplatelets ($Zn_5(OH)_8Cl_2 \cdot H_2O$).

2.3. Material Characterization

Scanning electron microscopy (SEM) analysis was carried out to reveal the morphology of the sample using a Zeiss Ultra Plus 55 field emission scanning electron microscope (FE-SEM) operated at an accelerating voltage of 2.0 kV. Surface area measurements were obtained using the Brunauer-Emmett-Teller (BET) method with N_2 gas. Pore size and pore volume were obtained using Barrett-Joyner-Halenda (BJH) method from the desorption branch of the isotherm. The sample was also characterized using X-ray diffraction (XRD). An XPERT-PRO diffractometer (PANalytical BV, Netherlands) with theta/theta geometry, operating a cobalt tube at 35 kV and 50 mA, was used. The XRD patterns of all specimens were recorded in the 10.0° – 70.0° 2θ range with a counting time of 15.240 seconds per step. Qualitative phase analysis of the sample was conducted using the X'pert Highscore search match software. Fourier transform infrared (FT-IR) spectra of the SimonK were recorded using a Bruker Vertex 77 v FT-IR spectrometer. The electrochemical properties were investigated using a Bio-Logic SP300 workstation (Knoxville TN 37,930, USA) in a three-electrode configuration controlled by the EC-Lab® V10.37 software. The simonK/GF composite on NF-G served as the working electrode in a 6.0 M potassium hydroxide (KOH) electrolyte; glassy carbon plate was used as the counter electrode and Ag/AgCl (3 M KCl) as the reference electrode.

The cyclic voltammetry tests were carried out in the potential range of 0 to 0.5 V (vs. Ag/AgCl) at different scan rates ranging from 10 to 100 mV s^{-1}. The galvanostatic charge–discharge measurements were also carried out at different current densities from 1 to 10 A g^{-1} and the electrochemical impedance spectroscopy (EIS) measurements were performed in the frequency range of 100 kHz–10 mHz.

3. Results and Discussion

Fig. 1 shows the morphology of the in situ grown simonkolleite microplatelets with and without graphene foam obtained from microscopy analysis. Figs. 1a and b show the simonK sheets interlaced with each other at lower and higher magnifications respectively. Thinner microplatelets are obtained (shown by dashed-arrows in Figs. 1c and 1d at different magnification respectively) as a result of adding graphene foam to simonkolleite growth precursors which shows the successful exfoliation of the simonkolleite sheets with graphene flakes to form the simonK/GF composite. The average thickness of the pure simonK sheets is between 52–96 nm while the thickness is observed to reduce to about 30–45 nm for simonK/GF composite sheets. SimonK and simonK/GF interlaced sheets growing on the surface of a NF-G substrate are shown in Figs. 1e and f respectively. The combination of thin sheets of both simonkolleite and graphene is visible which

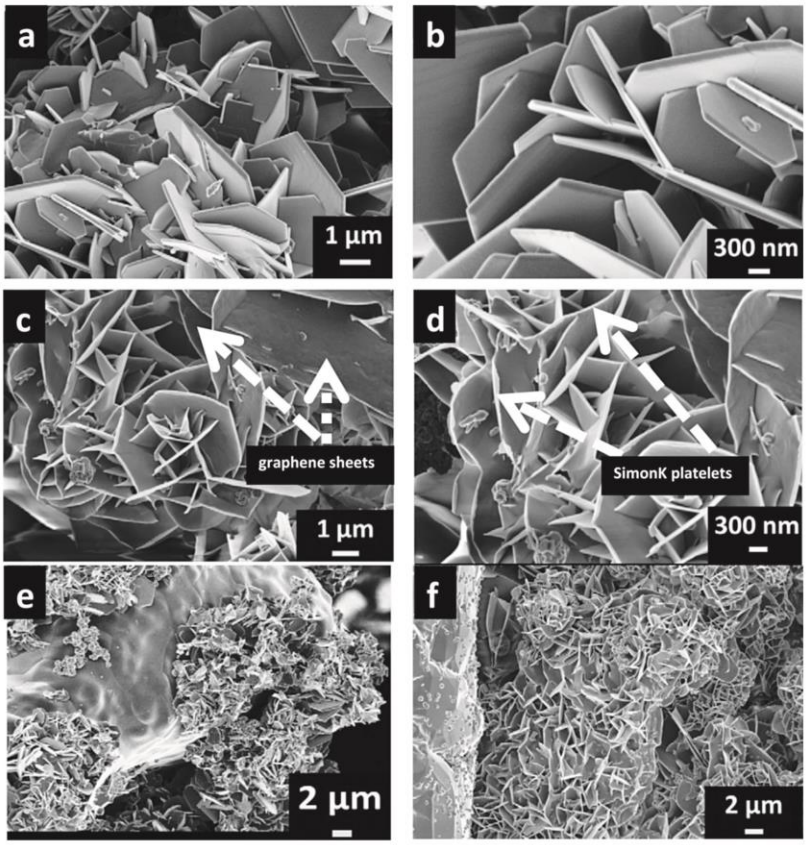

Fig. 1. SEM of; (a,b) simonkolleite at low and higher magnification; (c,d) simonkolleite-graphene foam at low and high magnification (e) simonkolleite and (f) simonkolleite-graphene foam on NF-G.

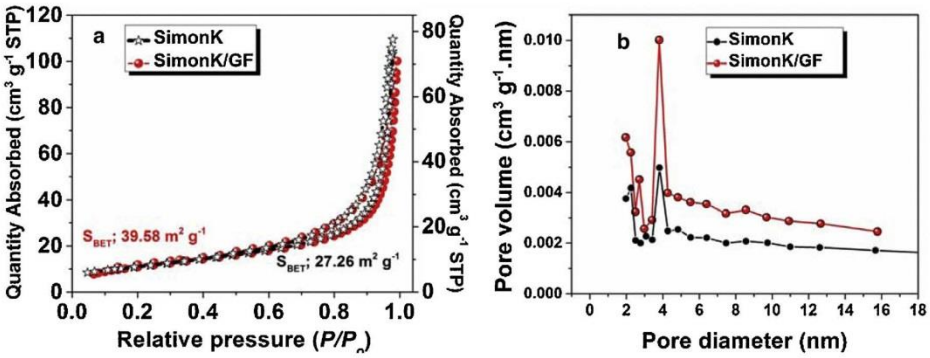

Fig. 2. (a) N_2 absorption/desorption isotherms; (b) pore size distribution of simonkolleite and simonkolleite-graphene foam composite.

is necessary for providing the surface required for charge transport and storage. The effect of the addition of graphene foam is clearly visible from the thickness of the hexagonal sheets. The morphology observed from the microscopy images of the composite is ideal for electrochemical applications involving interface reactions.

The presence of a porous structure in the composite is confirmed from the Brunauer-Emmett-Teller (BET) method displayed in Fig. 2. Pore size distribution was obtained using Barrett-Joyner-Halenda (BJH) method from the desorption branch of the isotherm. The physical adsorption/desorption of N_2 at 77 K results are shown in Fig. 2a. The BET specific surface area (SSA) values for the simonK and simonK/GF composite were calculated to be 27.26 $m^2 g^{-1}$ and 39.58 $m^2 g^{-1}$ respectively. These values are comparable to or even larger than values reported in earlier research work on simonkolleite-based materials [15]. Fig. 2b shows the corresponding pore size distribution with a major pore diameter ranging from 2 – 4 nm which further confirms the presence of mesoporous sites which are used as pathways for transport of ions necessary for power delivery [16,17]. The supercapacitive performance of the active electrode material is dependent on its ability to accommodate as much active electrochemical sites for charge storage during operation. The presence of suitable mesopores within the electrode material is also ideal to ensure the reduction of mass transfer of electrolyte during fast redox reactions and facilitates power delivery [5].

Fig. 3a shows the XRD patterns of the synthesized simonK microplatelets and the composite electrode material with graphene foam added (simonK/GF). Typical diffraction peaks which correspond to the simonkolleite material are indexed to pure rhombohedra simonkolleite [Joint Committee on Powder Diffraction Standards (JCPDS No. 07-0155). These simonkolleite peaks are also similar to those reported in earlier studies [10,11] in which characteristic reflection patterns of the same material were studied. The sharp and strong peaks show the relatively high crystallinity of the sample. However, these peaks exhibit a shift due to the nature of the X-ray source (cobalt) used in the analysis of the samples. For example, the reflection from the (003) plane with a strong diffraction peak usually ascribed to the 2θ angle of ~ 11.30° [10] is now observed at 15.10°. Likewise, similar peak shifts exist for other planes, such as the (015), (110) and the graphene peak indexed as (002) plane which show diffraction peaks at 2θ values of 28.00°, 32.50° and 30.90° respectively. The shifts are due to the difference in wavelength of the incoming X-rays which are dependent on the X-ray source, according to the Bragg equation $n\lambda = 2dsin\theta$. In general, X-rays from a cobalt source (λ=1.79 Å) with longer wavelengths result in greater 2θ positions compared with those from a copper source (λ=1.54 Å). The former usually allows the observation of low-angle peaks that are not observable using the shorter wavelength X-rays and provides better peak separation [18]. The XRD analysis shows that simonkolleite has a strong preferential orientation along (003). The corresponding angular position of about $2\theta_{(003)}$ which is ~15.10° is related to the highly ordered reticular planes characterized by a *d*-spacing value of ~6.812 Å when calculated from the XRD data. The lattice constants for <a> and <c> are obtained as ~7.651 Å and ~20.435 Å, respectively.

Fig. 3b shows the FT-IR spectrum of the simonkolleite, simonkolleite-graphene foam composite and graphene foam

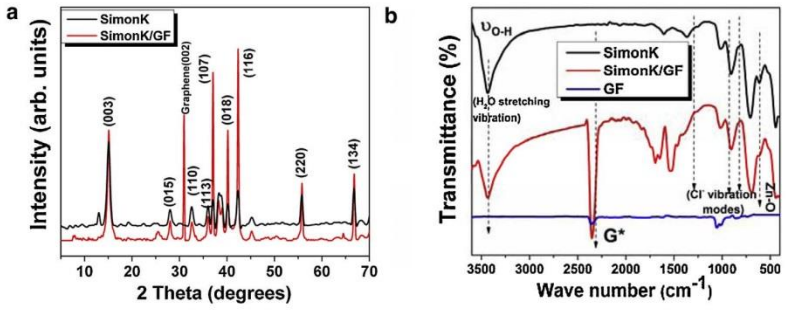

Fig. 3. (a) XRD patterns and (b) FTIR spectra of simonkolleite and simonkolleite-graphene foam composite.

(GF), respectively. These measurements were performed within a wavenumber range from 360 to 3600 cm^{-1}. A broad absorption band centered at about 3435 cm^{-1} corresponds to the O-H stretching vibrations of the interlayer water molecules [10,15]. The observed band at 2358 cm^{-1} is not observed in pure simonkolleite sample and is related to the presence of graphene foam (G*) in the composite. This band is attributed to the C-H vibrations of the methylene group. Intensive bands at 898 cm^{-1} and 719 cm^{-1} are also observed and are due to stretching vibration modes of chloride (Cl^-) ion [19,20]. The bands at approx. 453 cm^{-1} corresponds to translational modes of the Zn-O bonds [10].

Cyclic voltammetry (CV) measurements are used to understand the macroscopic electrochemical surface reactions at the electrode material during operation. Fig. 4a shows the CV curves for a NF-G current collector, simonkolleite and simonkolleite-graphene foam composite electrodes on the NF-G current collector at a scan rate of 20 mV s^{-1} in a potential window range of 0.0 – 0.5 V. The CV plots are characterized by symmetrical characteristic profiles that are well defined by cathodic (reduction reaction) and anodic (oxidation reaction) peaks [21]. This reveals that the electrode reaction corresponds to a quasi-reversible process, indicating that the measured capacitance in these materials is mainly based on the redox mechanism due to the pseudocapacitive behavior of the material [22]. The NF-G exhibited the lowest intensity current peaks due to the quasi-super hydrophobicity which is attributed to poor surface wetting leading to a reduced access to and limited

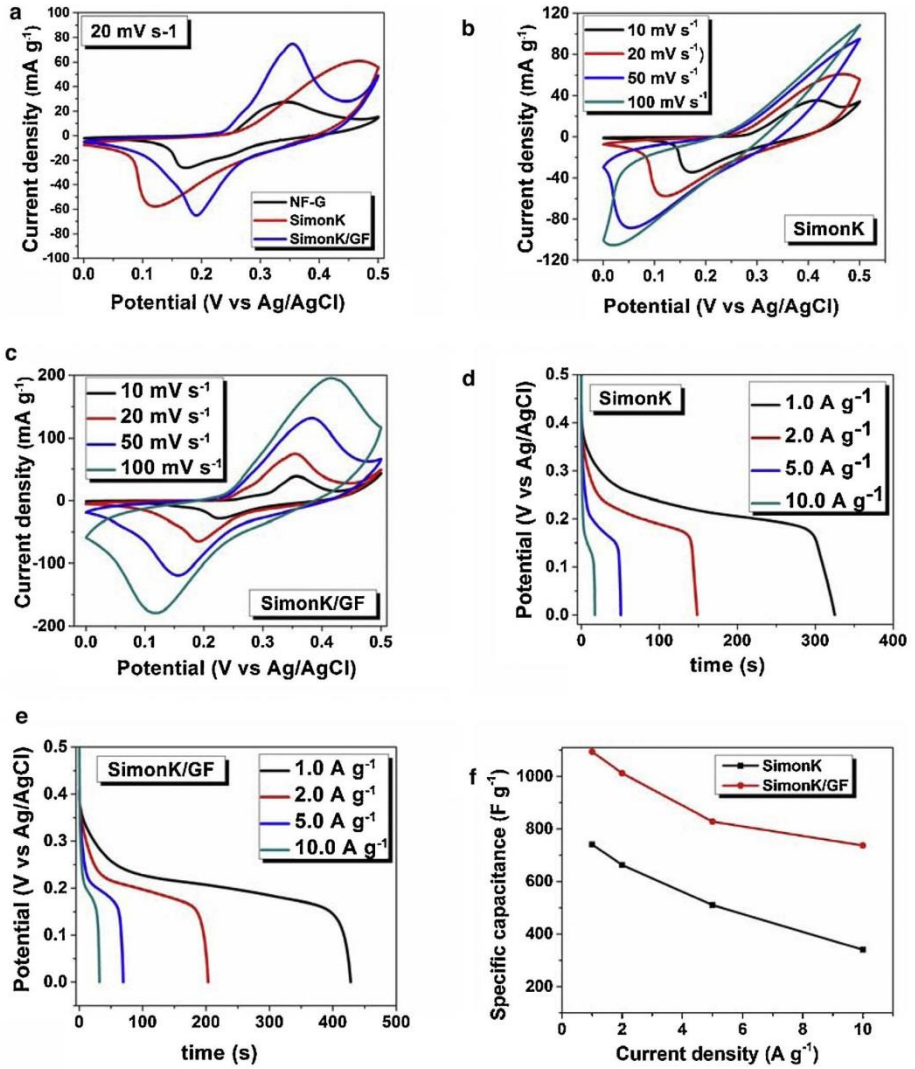

Fig. 4. (a) Cyclic voltammetry (a) nickel foam-graphene, simonkolleite and simonkolleite-graphene foam composite; (b) simonkolleite and (c) simonkolleite-graphene foam grown in situ on NF-G at scan rates of 10–100 mV s^{-1}; Galvanostatic charge–discharge of (d) simonkolleite and (e) simonkolleite-graphene foam composite measured at current densities of 1–10 A g^{-1}; (f) specific capacitance of simonkolleite and simonkolleite-graphene foam composite electrode at different current densities calculated from the galvanostatic discharge curves.

utilization of the available surface area of pristine graphene [11]. It can also be clearly seen that the integral area of the CV graph of simonK/GF composite is the largest among the three materials in the plot, implying that it possesses the highest specific capacitance. The improved pseudocapacitance could be due to the contributing effect from the added graphene foam which prevents the restacking of simonkolleite sheets, thus producing thinner sheets with higher electrolyte ion (K^+) accessibility and the highly conductive graphene layer on nickel foam.

Figs. 4b and 4c show the CV plot for simonK and simonK/GF composite in a potential window of 0.0 – 0.5 V at a scan rates ranging from 10 to 100 mV s^{-1}. The redox peaks are much precisely defined in the composite material compared to simonK alone. This is due to high thickness of the simonkolleite platelets owing to aggregation, resulting in retarded transport of electrolyte ions [11]. On the other hand, for the composite electrode material containing graphene, the highly conductive sheets of graphene becomes entangled with the simonkolleite platelets and provide unobstructed pathways for K^+ ion transport during the rapid charge–discharge process. The twin redox peaks are more visible in the composite material even at higher scan rates and are seen to undergo small shifts towards the left (negative potential) with increasing scan rate. The peaks at 0.39 V and 0.16 V are related to the anodic and cathodic peaks of the simonK/GF composite material at a scan rate of 30 mV s^{-1}. These peaks result from the intercalation and de-intercalation of K^+ from the electrolyte into the $Zn_5(OH)_8Cl_2 \cdot H_2O$ [11]. Thus the charge storage mechanism of simonkolleite-based composite electrodes is ascribed to the rapid intercalation of alkali metal cations K^+ in the electrode during reduction and oxidation processes [11,23].

The galvanostatic charge–discharge curves for simonkolleite and simonkolleite-graphene foam composite were measured at different current densities of 1.0–10.0 A g^{-1} as shown in Figs. 4d and 4e respectively. The shape of the discharge curves shows a characteristic pseudocapacitance [24,25]; and this is in agreement with the CVcurves which show redox peaksresulting from the oxidation-reduction reaction at the interface between the electrode and theelectrolyte.The specific capacitance was calculated from the galvanostatic discharge curves using the formula [5,26]:

$$C_s(\mathrm{F/g}) = I \times T_d/(m \times \Delta\Omega) \quad (6)$$

where I is a current (A), T_d s the discharge time (s), m s the mass of active material (g), and ΔV s the voltage range (V).

An enhancement in the discharge time for the simonK/GF composite electrode at 1 A g^{-1} current density is observed in Fig. 4e as compared with that of simonK alone (Fig. 4d). A specific capacitance of 1094 F g^{-1} is obtained for simonK/GF composite compared with a much lower specific capacitance value of 741 F g^{-1} for pristine simonK at a current density of 1 A g^{-1}. This is a considerable enhancement and is a great improvement over our earlier studies on simonkolleite microplatelets prepared by an aqueous chemical growth method technique [11]. We therefore propose that the improvement in supercapacitance value is as a result of the addition of a porous and conducting graphene foam to the simonK matrix which provides an improved electron transfer rate and better structural support in form of exfoliation of thinner simonK microplatelets interacting with graphene sheets [11]. Fig. 4f shows the variation of the specific capacitance (C_s) with current densities for both simonK and simonK/GF composite electrodes. From the figure, it can be observed that there is a decrease in specific capacitance with increasing current density. This is due to the limited movement of ions and protons by diffusion at higher current densities, which accesses only the outer active surface of the material for charge storage [5,27]

Fig. 5a shows the Nyquist plots obtained from the electrochemical impedance spectroscopy (EIS) measurements done at

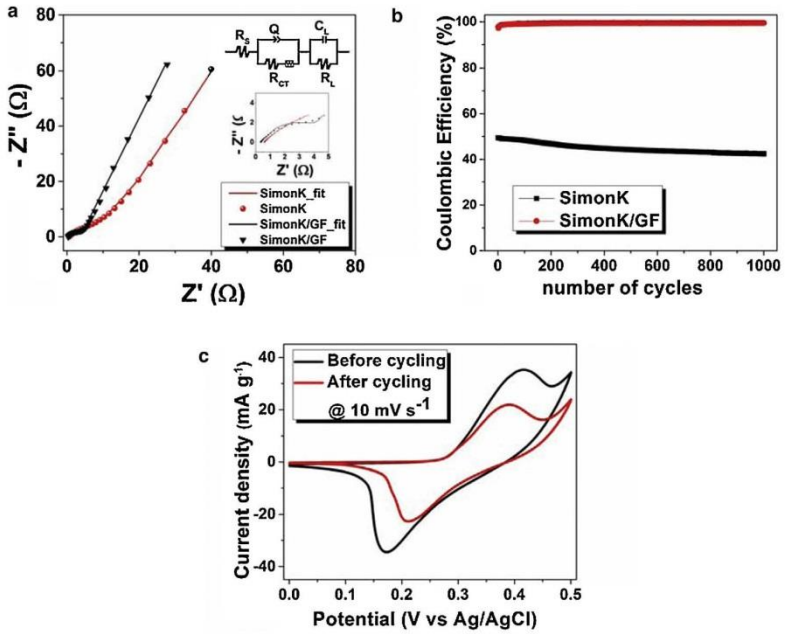

Fig. 5. (a) EIS plot of simonkolleite and simonkolleite-graphene foam composite (insets to the fig. shows the high frequency region zoomed in and a fitted RC circuit related to the sample electrodes respectively) (b) Dependence of the coulombic efficiency on the charge-discharge cycle number for simonkolleite and simonkolleite-graphene foam on NF-G at a current density of 10 A g^{-1}; (c) CV comparison before and after 1000 cycles at a scan rate of 10 mV s^{-1} of simonkolleite-graphene foam composite.

open circuit (E_{oc}) potential to further evaluate the electrochemical behavior for the simonkolleite and simonkolleite-graphene foam composite at a frequency range of 10 mHz to 100 kHz. The scan begins from the high frequency (100 kHz) to the low frequency end (10 mHz). At the former frequency, a partial semi-circular arc is observed which is attributed to the dispersion effect [28]. At low frequency, the impedance plot should, theoretically, be a vertical line parallel to the vertical -Im (Z") axis. However a slightly tilted vertical line is seen which indicates a pure capacitive behavior of the simonK material and low diffusion resistance of ions within the structure of the material [5]. The intersection of the curve on the real part of Z' axis in the high frequencies range corresponds to the equivalent series resistance (ESR) value (also called the solution resistance, R_S) and is described as the resistance of both the electrolyte, contact resistance at the active material/current collector interface and the internal resistance of the electrode [8,29]. The Nyquist spectrum of both electrodes can be represented by a modified Randles circuit [30] also referred to as an equivalent circuit (EQC) with a set of resistors and capacitors as shown in the inset to Fig. 5a. From the figure, the EIS data fitting software (ZFIT) that applies the complex nonlinear least-squares (CNLS) method [31] is used for fitting experimental data with a model which best describes the circuit elements. The equivalent series resistance, R_S is in series with the constant phase element, Q. The small semi-circular arc in the high-frequency region to mid-frequency is modelled by a charge transfer resistance R_{CT} and Q which is responsible for the ideal capacitance of the samples both connected in parallel to each other.

The high-frequency semicircle to the mid-frequency tail can be represented by the Warburg element W which is expressed as:

$$W = A/j\omega^{0.5} \quad (7)$$

where A is the Warburg coefficient, ω is the angular frequency and n is an exponent [32,33]. The impedance of the constant phase element Q, can be expressed as:

$$Q = 1/T(j\omega)^n \quad (8)$$

where T is the frequency independent constant with dimensions of $(F cm^{-2})^n$ related to the roughness and pseudocapacitive kinetics of the electrode, n value varies from -1 to 1 and can be calculated from the slope of the log Z versus log f. For values of n = 0, Q acts as a pure resistor while for n = 1, Q acts as a pure capacitor and acts as an inductor when n = -1 [34].

For very low frequency values, an ideal electrode produces a vertical line parallel to the imaginary axis with a mass capacitance represented as Q. The deviation from this ideal behaviour is linked with a leakage resistance R_L and is placed parallel to the C_L in the equivalent circuit. C_L denotes the pseudocapacitance which arises as a result of the Faradaic charge transfer process [33].

The charge transfer resistance (R_{CT}) describes the rate of redox reactions at the electrolyte-electrode interface [35] and this corresponds to the semi-circular arc radius [28]. A lower R_{CT} value implies a faster ion transport during operation. Therefore, a higher ion transport rate will lead to an enhanced device electrochemical performance. From the experimental data obtained, the arc radius formed in Fig. 5a is smaller for the simonK/GF composite which confirms the faster ion transport. The ESR value from the Nyquist plots improves from 0.55 Ω for simonK alone to 0.35 Ω for the simonK/GF composite respectively as read from the intercept of Z' and this is clearly shown by the inset to Fig. 5a for zoomed-in high to mid frequency part. This is possibly due to the presence of graphene foam in the composite electrode material.The ESR value obtained from the fitting for simonK and simonK/GF composite is calculated as 0.595 Ω and 0.368 Ω respectively. This is seen to be close to the values obtained experimentally and signifies an excellent fit with the experimental data. Thus, it is reasonable to state that the enhancements observed, could be attributed to the better conductivity and favorable electron transfer rate within the composite electrode material. The n-values obtained from the fitting of the Nyquist plots for the simonK and simonK/GF composite were calculated as 0.647 and 0.769 respectively. Thus the results for n indicate a capacitive behavior from the above discussions. This further confirms a successful fitting process on the experimental data obtained from EIS analysis. A summary of the CNLS fitting parameters from the experimental impedance spectra is presented in Table 1.

Table 1
Calculated Values of fitted parameters through CNLS Fitting of the Experimental Impedance Spectra Based on the equivalent circuit shown in the inset to Fig. 5a

Electrode	R_s (Ω)	R_{CT} (Ω)	C_L (F)	n	Q
SimonK	0.595	9.638	0.350	0.647	0.126
SimonK/GF	0.368	3.942	0.674	0.769	0.014

The stability of the electrode material of supercapacitors is also a very important characteristic for their application as energy storage devices. Fig. 5b shows the continuous galvanostatic charge–discharge cycling of simonK and simonK/GF composite respectively, at 10 A g^{-1} current density for 1000 cycles. The stability plot was characterized by little change in the coulombic efficiency obtained from repeated charging and discharging in both materials, which initially increased after a few number of cycles before stabilizing at a higher number of cycles. It is suggested that this increase is as a result of the full exposure of electrolyte ions to some inner sites of the electrode material which were not exposed during the initial cycling stage, and due to the activation of simonK/GF sites which contribute to an increase in capacitance after some initial cycling of the active electrode material [5,14]. The coulombic efficiency of the simonK electrode material after 1000 cycles is recorded at a value of 43.1%. However, for simonK/GF composite, a much more improved and stable coulombic efficiency of 99.7% is recorded after 1000 cycles. This is also an improvement over our earlier report for application of simonK as supercapacitor electrodes [11]. This is an indication that the addition of graphene foam to the simonK matrix has a long-term electrochemical stability and a high degree of charge–discharge reversibility. The excellent pseudocapacitive behavior and high cycling stability can be attributed to the high electrical conductivity and improved specific surface area, allowing rapid and effective ion charge transfer and electron transport.

Since redox reactions also take place during the continuous cycling charge–discharge process, a comparison was made for the CV curves before and after cycling as represented in Fig. 5c to further analyze the cyclic stability of the composite electrode material. Similar CV curves were obtained before and after the 1000th cycle with a little shift in the cathodic peak. In other words, both CV curves appear with their usual redox peaks which confirm the electrode stability. However, a slight reduction in the intensity and observed shift of the peak position is possibly caused by consumption of some of the active sites in the material which leads to some subsequent capacitance loss [28]. Thus, these results show the suitable use of the composite electrode for energy storage applications due to the promising and improving trend of electrochemical properties.

4. Conclusion

In this paper, we reported an excellent and improved pseudo-capacitance behavior of simonK/GF microplatelets synthesized by an

in situ hydrothermal technique on nickel foam-graphene (NF-G) current collector as compared to simonK alone. The choice of the NF-G substrate was used based on earlier studies which showed better response when used as a current collector [36]. The simonK/GF composite electrode exhibits an enhanced electrochemical performance due to the presence of the graphene in the simonK matrix and gives a specific capacitance of 1094 F g^{-1} at a current density of 1 A g^{-1} and a capacitive retention of about 99.7% after 1000 charge–discharge cycles. This shows that these composites are promising electrode materials for energy storage devices.

Acknowledgments

This work is based upon research supported by the South African Research Chairs Initiative (SARChi) of the Department of Science and Technology (DST) and the National Research Foundation (NRF). Any opinion, findings and conclusions or recommendations expressed in this work are those of the authors and the NRF and DST do not accept any liability with regard thereto. D.Y acknowledges the financial support from University of Pretoria and the NRF Doctorate Innovation Fund for his study.

References

[1] P. Simon, Y. Gogotsi, Materials for electrochemical capacitors, Nat. Mater. 7 (2008) 845–854.
[2] L. Wang, D. Wang, X.Y. Dong, Z.J. Zhang, X.F. Pei, X.J. Chen, et al., Layered assembly of graphene oxide and Co-Al layered double hydroxide nanosheets as electrode materials for supercapacitors, Chem. Commun. (Camb). 47 (2011) 3556–3558.
[3] Z. Gao, J. Wang, Z. Li, W. Yang, B. Wang, Graphene nanosheet/Ni2+/Al3+ layered double-hydroxide composite as a novel electrode for a supercapacitor, Chem. Mater. 23 (2011) 3509–3516.
[4] J. Memon, J. Sun, D. Meng, W. Ouyang, M.A. Memon, Y. Huang, et al., Synthesis of graphene/Ni–Al layered double hydroxide nanowires and their application as an electrode material for supercapacitors, J. Mater. Chem. A. 2 (2014) 5060.
[5] W. Yang, Z. Gao, J. Wang, J. Ma, M. Zhang, L. Liu, Solvothermal one-step synthesis of Ni-Al layered double hydroxide/carbon nanotube/reduced graphene oxide sheet ternary nanocomposite with ultrahigh capacitance for supercapacitors, ACS Appl. Mater. Interfaces. 5 (2013) 5443–5454.
[6] B. Wang, G.R. Williams, Z. Chang, M. Jiang, J. Liu, X. Lei, et al., Hierarchical NiAl Layered Double Hydroxide/Multiwalled Carbon Nanotube/Nickel Foam Electrodes with Excellent Pseudocapacitive Properties, ACS Appl. Mater. Interfaces. 6 (18) (2014) 16304–16311.
[7] P. Chen, G. Shen, Y. Shi, H. Chen, C. Zhou, Preparation and characterization of flexible asymmetric supercapacitors based on transition-metal-oxide nanowire/single-walled carbon nanotube hybrid thin-film, ACS Nano. 4 (2010) 4403–4411.
[8] Z. Fan, J. Yan, T. Wei, L. Zhi, G. Ning, T. Li, et al., Asymmetric Supercapacitors Based on Graphene/MnO2 and Activated Carbon Nanofiber Electrodes with High Power and Energy Density, Adv. Funct. Mater. 21 (2011) 2366–2375.
[9] M.-Q. Zhao, Q. Zhang, J.-Q. Huang, F. Wei, Hierarchical Nanocomposites Derived from Nanocarbons and Layered Double Hydroxides - Properties, Synthesis, and Applications, Adv. Funct. Mater. 22 (2012) 675–694.
[10] J. Sithole, B.D. Ngom, S. Khamlich, E. Manikanadan, N. Manyala, M.L. Saboungi, et al., Simonkolleite nano-platelets: Synthesis and temperature effect on hydrogen gas sensing properties, Appl. Surf. Sci. 258 (2012) 7839–7843.
[11] S. Khamlich, A. Bello, M. Fabiane, B.D. Ngom, N. Manyala, Hydrothermal synthesis of simonkolleite microplatelets on nickel foam-graphene for electrochemical supercapacitors, J.Solid State Electrochem. 17 (2013) 2879–2886.
[12] F. Hawthorne, E. Sokolova, Simonkolleite, Zn5 (OH) 8Cl2 (H2O), a decorated interrupted-sheet structure of the form [MO2]4, Can. Mineral. 40 (2002) 939–946.
[13] K.J. Huang, L. Yan, C.S. Xie, Effect of Surfactants on the Morphologies of ZnO Nanostructures Synthesized by Hydrothermal Method and its Gas Sensitivity to Formaldehyde, in, Adv. Mater. Res. (2011) 628–633.
[14] L. Zhang, J. Wang, J. Zhu, X. Zhang, K. San Hui, K.N. Hui, 3D porous layered double hydroxides grown on graphene as advanced electrochemical pseudocapacitor materials, J. Mater. Chem. A. 1 (2013) 9046.
[15] T. Long, S. Yin, K. Takabatake, P. Zhnag, T. Sato, Synthesis and Characterization of ZnO Nanorods and Nanodisks from Zinc Chloride Aqueous Solution, Nanoscale Res. Lett. 4 (2008) 247–253.
[16] C. Liu, F. Li, L.-P. Ma, H.-M. Cheng, Advanced materials for energy storage, Adv. Mater. 22 (2010) E28–62.
[17] M. Zhi, C. Xiang, J. Li, M. Li, N. Wu, Nanostructured carbon-metal oxide composite electrodes for supercapacitors: a review, Nanoscale. 5 (2013) 72–88.
[18] W.L. Bragg, The diffraction of short electromagnetic waves by a crystal, Proc. Camb. Philol. Soc. (1913) 43–57.
[19] N.V. Bhat, M.M. Nate, M.B. Kurup, V.A. Bambole, Structural changes in chlorine implanted poly(vinyl alcohol) films, Nucl. Instruments Methods Phys. Res. Sect. B Beam Interact. with Mater Atoms. 262 (2007) 39–45.
[20] T. Ishikawa, K. Matsumoto, K. Kandori, T. Nakayama, Anion-exchange and thermal change of layered zinc hydroxides formed in the presence of Al(III): Colloids Surfaces A Physicochem, Eng. Asp. 293 (2007) 135–145.
[21] Y. Tao, L. Ruiyi, L. Zaijun, L. Junkang, W. Guangli, G. Zhiquo, A free template strategy for the fabrication of nickel/cobalt double hydroxide microspheres with tunable nanostructure and morphology for high performance supercapacitors, RSC Adv. 3 (2013) 19416.
[22] H. KuanXin, Z. Xiaogang, L. Juan, Preparation and electrochemical capacitance of Me double hydroxides (Me=Co and Ni)/TiO2 nanotube composites electrode, Electrochim. Acta. 51 (2006) 1289–1292.
[23] J. Yan, Z. Fan, T. Wei, W. Qian, M. Zhang, F. Wei, Fast and reversible surface redox reaction of graphene–MnO2 composites as supercapacitor electrodes, Carbon N. Y. 48 (2010) 3825–3833.
[24] P. Simon, Y. Gogotsi, B. Dunn, Materials science. Where do batteries end and supercapacitors begin? Science. 343 (2014) 1210–1211.
[25] J.-W. Lang, L.-B. Kong, W.-J. Wu, M. Liu, Y.-C. Luo, L. Kang, A facile approach to the preparation of loose-packed Ni(OH) 2 nanoflake materials for electrochemical capacitors, J.Solid State Electrochem. 13 (2008) 333–340.
[26] J. Wang, Y. Song, Z. Li, Q. Liu, J. Zhou, X. Jing, et al., In Situ Ni/Al Layered Double Hydroxide and Its Electrochemical Capacitance Performance, Energy & Fuels. 24 (2010) 6463–6467.
[27] Z.J. Lao, K. Konstantinov, Y. Tournaire, S.H. Ng, G.X. Wang, H.K. Liu, Synthesis of vanadium pentoxide powders with enhanced surface-area for electrochemical capacitors, J.Power Sources. 162 (2006) 1451–1454.
[28] B. Wang, Q. Liu, Z. Qian, X. Zhang, J. Wang, Z. Li, et al., Two steps in situ structure fabrication of Ni–Al layered double hydroxide on Ni foam and its electrochemical performance for supercapacitors, J.Power Sources. 246 (2014) 747–753.
[29] B.E. Conway, V. Birss, J. Wojtowicz, The role and utilization of pseudocapacitance for energy storage by supercapacitors, J.Power Sources. 66 (1997) 1–14.
[30] J.E.B. Randles, Kinetics of rapid electrode reactions, Discuss. Faraday Soc. 1 (1947) 11–19.
[31] B. Conway, Electrochemical supercapacitors: Scientific fundamentals and technological applications, Kluwer Academic Publishers, Plenum Press, New York, 1999.
[32] Y. Zhou, H. Xu, N. Lachman, M. Ghaffari, S. Wu, Y. Liu, et al., Advanced asymmetric supercapacitor based on conducting polymer and aligned carbon nanotubes with controlled nanomorphology, Nano Energy. 9 (2014) 176–185.
[33] C. Masarapu, H.F., Zeng, K.H., Hung, B. Wei Effect of Temperature on the Capacitance of Carbon Nanotube Supercapacitors, 3 (2009) 2199–2206.
[34] H. Guan, L.-Z. Fan, H. Zhang, X. Qu, Polyaniline nanofibers obtained by interfacial polymerization for high-rate supercapacitors, Electrochim. Acta. 56 (2010) 964–968.
[35] M. Sluyters-Rehbach, Impedances of electrochemical systems: Terminology, Nomenclature and Representation PART I: Cells with metal electrodes and liquid solutions, Pure Appl. Chem. 66 (1994) 1831–1891.
[36] D. Momodu, A. Bello, J. Dangbegnon, F. Barzeger, F. Taghizadeh, A.T.C. Johnson, et al., Solvothermal synthesis of NiAl double hydroxide microspheres on a nickel foam- graphene as an electrode material for pseudo-capacitors, AIP Adv. 4 (2014) 097122.

4.3.4 Concluding Remarks

Simonkolleite-graphene foam composite electrodes with outstanding stability were fabricated via a facile in situ solvothermal technique. The morphological studies revealed that the simonK sheets actually interlaced with the graphene sheets to form a hybrid interconnected network with improved surface area and electrochemical performance. The graphene sheets also aided in exfoliating thinner simonK sheets in the composite material as compared to the simonK sample alone. Results from this study demonstrate the successful combination of the properties from both materials and makes the composite electrode a potential material for supercapacitor applications.

4.3.5 References

[1] F. Hawthorne, E. Sokolova, Can. Mineral. 40 (2002) 939.

[2] H. Tanaka, A. Fujioka, A. Futoyu, K. Kandori, T. Ishikawa, J. Solid State Chem. 180 (2007) 2061.

[3] J. Sithole, B.D. Ngom, S. Khamlich, E. Manikanadan, N. Manyala, M.L. Saboungi, D. Knoessen, R. Nemutudi, M. Maaza, Appl. Surf. Sci. 258 (2012) 7839.

[4] S. Khamlich, A. Bello, M. Fabiane, B.D. Ngom, N. Manyala, J. Solid State Electrochem. 17 (2013) 2879.

[5] K.J. Huang, L. Yan, C.S. Xie, in:, Adv. Mater. Res., 2011, pp. 628–633.

[6] Z. Gao, J. Wang, Z. Li, W. Yang, B. Wang, Chem. Mater. 23 (2011) 3509.

CHAPTER 5

5.0 GENERAL CONCLUSIONS

In this section, the main results reported and discussed in chapter 4 are summarized below.

Three-dimensional (3D) graphene foam (GF) has initially been synthesized via an atmospheric pressure chemical vapor deposition (AP-CVD) technique using a nickel foam (NF) template. The graphene foam sample assumed a 3D framework due to the characteristic morphology of the NF template used as starting platform for the dissolution/diffusion of carbon atoms. At higher magnifications, the scanning electron microscopy (SEM) micrographs showed wrinkles of the GF surface which is attributed to difference in thermal expansion coefficients between the few-layer thick graphene and the nickel. A high quality, defect free structure is revealed from the Raman spectroscopy results displayed for different regions on the NF-G surface. The different regions consist of a combination of both single layer and few-layered graphene. However, the desirable structure still offers an ideal surface when integrated in different forms with appropriate Faradaic-active materials like NiAl layered double hydroxides through various routes in order to make graphene-based metal hydroxide composite materials.

The NiAl layered double hydroxides (NiAl LDHs) have been synthesized via a solvothermal method using different solvents such as ethanol, tert-butanol and

deionized water to tune their morphological and electrochemical properties. Using equal ratios of ethanol and deionized water, interlaced mesoporous NiAl LDH sheets were obtained while in a reaction medium containing a tert-butanol-deionized water (TBA-H_2O) mixture, spherical NiAl layered double hydroxides also referred to as NiAl double hydroxide microspheres (NiAl DHMs) were obtained. The NiAl DHMs are also composed of relatively thin sheets grown on microspheres as revealed from the scanning and tunneling electron microscopy results. The results from the XRD characterization spectra gave an idea of the structural characteristics of both materials of different morphologies. Although these materials were synthesized using different reaction solvents, the spectra clearly showed similar diffraction peaks for both NiAl LDH and NiAl DHM materials.

Zinc chloride hydroxide monohydrate (simonkolleite) platelets have been synthesized using the solvothermal method in a deionized water reaction medium. The microscopy results reveal hexagonal sheets interlaced with each other. Typical sharp and strong diffraction peaks which correspond to the simonkolleite material reported in earlier studies are indexed to pure rhombohedra simonkolleite showing the relatively high crystallinity of the sample. The XRD analysis shows that simonkolleite has a strong preferential orientation along the c-direction.

The addition of graphene foam to the metal hydroxides materials to obtain a graphene-metal hydroxide composite was done via different means in order to fully optimize both the electric double layer properties from graphene with the Faradaic properties from

the metal hydroxide component. For example, adding graphene foam to the NiAl LDH facilitates the growth of the LDH sheets in between the graphene foam sheets and reduced the restacking problem associated with LDH sheets. In the case of the simonkolleite reaction medium, the graphene foam aided the exfoliation of thinner simonK sheets interlaced with GF sheets on the NF-G growth template.

In section 4.1, graphene foam was integrated into the NiAl LDH and NiAl DHM matrices by two distinct methods. The initial route involved the direct incorporation of in different weighted amount of graphene foam into the NiAl LDH precursor reaction medium to enable the NiAl LDH sheets grow amongst the pre-sonicated graphene sheets thereby obtaining the final NiAl LDH-GF composite. The BET surface area of the NiAl LDH-GF was increased to 68.09 $m^2 g^{-1}$ from an initial value of 57.83 $m^2 g^{-1}$ for the pristine NiAl LDH.

The electrochemical performance results obtained by calculating the specific capacitance from the cyclic voltammogram showed an increasing trend up to a certain limit after which further addition of GF resulted in a decrease in specific capacitance value due to a proposed restacking of the excess graphene sheets.

The second route involved the growth of a thin film of few-layer graphene on the NF current collector to form a modified porous nickel foam-graphene (NF-G) current collector. The resulting composite electrode comprising of the NiAl DHM material coated onto the NF-G current collector exhibits an enhanced electrochemical performance. This is ascribed to the contribution from more electronegative species

present within the interlayer region of the DHM structure combined with the improved electron transfer rate from the high surface area and conductive graphene layer deposited on the NF surface.

In section 4.2, the NiAl LDH-GF composite obtained from the direct incorporation of graphene foam into the NiAl LDH precursor reaction medium was added to a P3HT:PCBM polymer blend to obtain the P3HT:PCBM/NiAl LDH-GF composite electrode by dip coating. An improvement in the electrochemical properties of the overall composite was depicted from the cyclic voltammetry tests. For example, the value of the specific capacitance increased to 1.22 F cm^{-2} for the P3HT:PCBM/NiAl LDH-GF composite electrode from an initial value of 0.29 F cm^{-2} for the pristine P3HT:PCBM nanostructure which is an order of magnitude enhancement. This tremendous improvement is one of the highest values reported for P3HT:PCBM based supercapacitors in aqueous electrolyte and is attributed to the high surface area of the 3D-graphene foam coupled with the redox active NiAl LDH in the NiAl LDH-GF composite material. The stability of the electrode was depicted by the similar cyclic voltammogram obtained before and after cycling through 500 charge-discharge cycles. This makes them potential materials for polymer-based supercapacitor electrodes.

Section 4.3 demonstrated the superior electrochemical capacitance of simonkolleite-graphene foam (SimonK/GF) composite electrode prepared via an in situ one step solvothermal synthesis route. Thinner simonK sheets are obtained when graphene foam

was directly added with improved surface area of the composite. This increased surface area provides the necessary active sites for the desired transport and storage of charges. Electrochemical tests carried out on the simonK/GF composite electrode revealed an increased specific capacitance of 1094 F g^{-1} as compared to 741 F g^{-1} for the pristine simonK electrode at 1 A g^{-1} current density. The composite electrode also exhibited a 99.7% coulombic efficiency after 1000 charge-discharge cycles. The stability of the electrode was further depicted by the similar cyclic voltammogram obtained before and after cycling. The excellent Faradaic-type behavior and high cycling stability can be attributed to the high electrical conductivity and improved specific surface area that allows rapid and effective ion charge transfer along with electron transport.

In summary, the results displayed clearly show the great potential of incorporating graphene foam into the main matrix of metal hydroxides to obtain graphene-based composites for energy storage device electrodes. The improvement of the electrochemical properties of polymer-based electrodes could also be achieved by the addition of these graphene-based composite materials to the pristine polymer blends. This study therefore provides an initial path towards developing prospective hybrid electrodes which combines the properties from both the graphene foam component and the Faradaic NiAl layered double hydroxide for energy storage applications.

CHAPTER 6

6.0 FUTURE WORK

The electrode material of a supercapacitor plays a major role in determining its electrochemical performance. An in depth understanding of the individual intrinsic material properties at the nanoscale level is the medium through which the device charge storage capability can be improved. The process of charge storage involves diffusion of ions which is linked to the specific surface area and porosity of the active material. Thus, in order to obtain an outstanding electrochemical performance, the method of material synthesis needs to be optimized in order to tune the properties of the final products to fit the specific application requirements.

Graphene-based composite materials have so far demonstrated a great potential as electrode material for supercapacitors as seen from the results discussed in Chapter 4 and reports mentioned in the literature studies in Chapter 2 of this thesis. The combination of graphene (carbonaceous EDLC type material) with faradaic type materials such as layered double hydroxides and polymer blends has the merit of synergizing their individual material properties to form composite nanostructured electrodes. Such merits include; providing a facile one-step procedure of fabricating composite electrodes, the prevention of restacking of LDH and graphene sheets,

improvement of the specific surface area and conductivity of the overall composite etc. However, the results discussed have only been done for composite electrode materials tested in a three (3) electrode configuration. The combination of these composite electrodes with other active electrodes stable in other voltage regions to form a hybrid asymmetric supercapacitor device that will be tested in a two (2) electrode configuration is necessary. Materials such as activated carbons and other faradaic-type metal oxides and hydroxides are possible electrodes for use. These need to be carefully studied in order to maximize the operating voltage window of the full device.

In addition, the graphene foam synthesized through chemical vapor deposition technique can be incorporated with other highly pseudocapacitive metal oxides pairs with large work function difference in order to obtain a hybrid nanostructured electrode for supercapacitors. The large work function difference will increase the operating voltage window which will also improve the energy density and specific capacitance of the asymmetric device without necessarily affecting its power density.